PROPAGATION OF FLUCTUATIONS AND DETECTION OF HIDDEN UNITS IN NETWORK DYNAMICAL SYSTEMS

Von der Fakultät für Mathematik und Naturwissenschaften der Carl von Ossietzky Universität Oldenburg zur Erlangung des Grades und Titels eines

DOKTORS DER NATURWISSENSCHAFTEN (DR. RER. NAT.)

angenommene Dissertation von Herrn

HAUKE HÄHNE

geboren am 9. Februar 1990 in Hamburg.

Erstgutachter:
Prof. Dr. Joachim Peinke,
Carl von Ossietzky Universität Oldenburg
Zweitgutachter:
Prof. Dr. Pedro Lind,
Oslo Metropolitan University
Weiteres Mitglied der Prüfungskommision:
Prof. Dr. Alexander Hartmann,
Carl von Ossietzky Universität Oldenburg

Tag der Disputation: 15. August 2019

CONTENTS

ABSTRACT

Networks of dynamical systems model a broad range of complex phenomena in natural and technological systems. The analysis of the interplay of dynamics and topology is divided into two major classes of problems: While forward approaches deduce properties of the dynamical evolution from the topology and the system parameters, inverse methods infer system properties from observations of the dynamics. With this thesis, we contribute to both fields: First, we analyze the spreading of fluctuations in power grids. In recent years, more and more conventional generators have been replaced with renewable sources among which wind power plays a key role. In contrast to the steady production of conventional power plants, wind power generation shows correlated and non-Gaussian fluctuations that are related to the intermittent fluctuations of turbulent flows. With power grid frequency measurements from two different places in Germany, we demonstrate that the short-term grid frequency fluctuations locally increase with increasing share of volatile wind power feed-in. We consider frequency increment statistics and provide analytical results for the propagation of their variance as a function of the distance to the feed-in and the system parameters. For the specific case of chains of synchronous machines, we show how reducing grid inertia impacts the type of the decay of the variance of frequency increment statistics. Second, we consider the case in which a network dynamical system, not necessarily a power grid, is only partially accessible for observations and derive a novel method to detect nodes that are hidden from measurement. We test our approach on systems with various, possibly noisy, dynamics, including periodic and chaotic collective motion, and demonstrate successful detection and quantification of hidden nodes even in the case where only very few nodes are measured. Our method is model-free and relies on fundamental relations of linear algebra.

ZUSAMMENFASSUNG

Netzwerke dynamischer Systeme modellieren eine Vielzahl komplexer Phänomene in natürlichen und technischen Systemen. Die Analyse der Interaktion von Topologie und Dynamik lässt sich in zwei dominierende Klassen einteilen: Während forwärtsgerichtete Ansätze die dynamische Entwicklung aus Eigenschaften der Topologie und der Systemparameter ableiten, schlussfolgern inverse Methoden die Systemparameter aus Beobachtungen der Dynamik. Mit dieser Arbeit tragen wir zu beiden Klassen bei: Erstens untersuchen wir die Ausbreitung von Fluktuationen in Stromnetzen. In den letzten Jahren wurden mehr und mehr konventionelle Stromerzeuger durch erneuerbare Quellen ersetzt, bei denen die Windenergie eine Schlüsselrolle einnimmt. Im Gegensatz zur kontinuierlichen Produktion konventioneller Kraftwerke zeigt die Windenergieproduktion korrelierte und nicht gaußförmige Fluktuationen, die in Zusammenhang zu den intermittenten Fluktuationen turbulenter Strömungen stehen. Mit Frequenzmessungen im Stromnetz an zwei verschiedenen Standorten in Deutschland demonstrieren wir, dass die Kurzzeitfluktuationen lokal zunehmen, wenn der Anteil volatiler Windenergieeinspeisung zunimmt. Wir betrachten Inkrementstatistiken der Frequenz und zeigen analytische Ergebnisse für die Ausbreitung ihrer Varianz als Funktion des Abstands zur Einspeisung und den Systemparametern. Für den spezifischen Fall von Ketten aus Synchronmaschinen zeigen wir, wie die Reduktion der Trägheit im Netz die Art des Abfalls der Varianz der Inkrementstatistik der Frequenz beeinflusst. Zweitens betrachten wir den Fall, in dem ein Netzwerk dynamischer Systeme, nicht notwendigerweise ein Stromnetz, nur teilweise zugänglich für Beobachtungen ist und leiten eine neuartige Methode her, mit der Knoten, die nicht messbar sind, detektiert werden können. Wir testen unseren Ansatz mit Systemen mit verschiedenartiger, möglicherweise verrauschter, Dynamik, einschließlich periodischer und chaotischer kollektiver Bewegung, und demonstrieren die erfolgreiche Detektion und Quantifizierung versteckter Knoten selbst wenn nur sehr wenige Knoten messbar sind. Unsere Methode ist modellfrei und beruht auf fundamentalen Zusammenhängen linearer Algebra.

LIST OF PUBLICATIONS

Haehne, H., Casadiego, J., Peinke, J., & Timme, M. (2019). Detecting Hidden Units and Network Size from Perceptible Dynamics. *Physical Review Letters*, 122(15), 158301.

H.H., J.C., and MT. conceived and designed the research, worked out the theory and derived the analytical results. H.H., advised by J.C. and M.T., carried out the numerical experiments and prepared the figures. All authors contributed methods and analysis tools. H.H., J.C. and M.T. analyzed the data. All authors interpreted the results and contributed to the writing of the manuscript.

***

Haehne, H., Schmietendorf, K., Tamrakar, S.R., Peinke, J., & Kettemann, S. (2019) Propagation of Wind-Power-Induced Fluctuations in Power Grids. *Physical Review E*, 99, 050301(R).

Rapid Communication.

H.H. performed the experimental measurements. H.H., advised by J.P., analyzed and evaluated the data. S.K. and H.H. worked out the theoretical results. H.H., with preparatory work from S.T., performed the numerical simulations. K.S. and S.T. generated the artificial production data with the stochastic model. S.T. prepared the data set for the SciGrid topology. H.H. wrote the manuscript and prepared the figures. S.K. and H.H. wrote the supplemental material. All authors contributed to interpreting the results and editing the manuscript.

***

Haehne, H., Schottler, J., Waechter, M., Peinke, J., & Kamps, O. (2018). The footprint of atmospheric turbulence in power grid frequency measurements. *Europhysics Letters*, 121(3), 30001.

Editor's Choice.

J.S. and H.H. performed the experimental measurements. H.H., advised by O.K., J.P., and M.W., analyzed and evaluated the data. H.H. wrote the manuscript and prepared the figures. All authors contributed to interpreting the results and editing the manuscript.

1 INTRODUCTION

Networks model a broad range of systems of interconnected units [1]. Applications include the spreading of diseases through contact networks [2, 3], the complex interaction of spiking neurons [4], networks of gene regulation [5, 6], and technological networks such as electric power grids [7].

The structure of a network critically affects its function [8]. In most cases, one cannot conclude on the functioning of the overall system only from properties of the isolated units. The collective, often complex, behavior of a networked system arises from the interplay of individual dynamics at each unit and the network structure. Often, desired collective states, such as the synchronization of the dynamics at all nodes, is robust against perturbations on some networks and very fragile on others [9]. So, how does network structure interact with the dynamic evolution of each node? How does that affect the collective behavior of the units? The concept of network dynamical systems allows for a systematic analysis of the collective dynamics as a function of local dynamics and the network [10].

We differentiate between two major directions of research in network dynamical systems [11]: First, *forward problems* enquire properties of the system from the structure of the network and the individual dynamics [10, 12, 13]. Questions like how fast a disease spreads on a given aviation network or how a gene regulatory network reacts to silencing a specific component fall under this category. The second important field constitute the *inverse problems* which deal with the case in which information on the network is retrieved from measured or desired dynamics [11, 14–16]. To stick to our examples, one may want to trace back how a disease spreads from one population to another from a data set of infections at different places. One possible outcome would be that the aviation network is responsible for the spreading. In gene regulation, one may want to infer which gene activates or represses the expression levels of other genes in the cell.

In this thesis, we want to contribute to both fields. First, we analyze how fluctuations of renewable power generators spread in power grids (which is a forward problem) and, second, we show how unknown units, hidden to measurements, can be inferred from th dynamics of the accessible units (which is an inverse problem).

The dynamics of high-voltage alternating current (AC) power grids is governed by the dynamics of large, conventional generators that can be modeled as inert phase-coupled oscillators [7]. Reliable energy supply is only possible if all nodes in the network show synchronous frequencies. Hence, the stability of the collective synchronous state is of particular importance for power systems. In 2008, Filatrella *et al*. [7] drew the analogy between synchronization in power grids and the Kuramoto model [17], a celebrated model for the study of synchronization of phase-coupled oscillators [13]. Since then, the collective dynamics of power grids is a rapidly evolving field in theoretical physics [7, 18–22].

The ongoing replacement of conventional with renewable generators imposes new challenges and risks upon reliable operation of power grids. The fact that wind (and also solar) power fluctuates on various timescales, from hours down to seconds [23], makes us wonder how such fluctuations impact on and spread in power grids. The problem of signal propagation in network dynamical systems is not only relevant to power grids, but of interest for various systems, from viral spreading to neuronal or biochemical signal propagation [24]. In this thesis, we focus on the propagation of fluctuations from wind power generators in power grids.

Time series of wind power production show heavily correlated and non-Gaussian fluctuations that are related to statistical properties of turbulent flows [25–27]. It is convenient to analyze fluctuations of a signal $x(t)$ in terms of increments $\Delta_\tau x(t) := x(t+\tau) - x(t)$ on timescale τ. This viewpoint on fluctuations is popular in turbulence research [28, 29] and allows for a separation of effects on timescales τ in the signal $x(t)$. While several recent studies analyze the impact of fluctuating feed-in on the synchronization of inert oscillators in power grids with numerical and analytic methods [30–37], it still lacks (i) a direct relation to measured data from real-world power grids and (ii) a theory to describe the propagation of fluctuations in power grids in terms of increment statistics.

An important inverse problem in network dynamics deals with the task of revealing the underlying network from measured data of the dynamics at each unit. This view on network dynamical systems not only helps to reveal physical structures from data but also contributes to designing optimal networks for desired dynamics or redesigning natural processes, such as gene and protein networks, in lab experiments [11, 38]. Established methods to reconstruct a network involve repeated measurements of the dynamics at each node in the network [11, 15, 38–50]. For a review, we refer to Ref. [11]. However, complete measurements of the entire network are rare and often, only a subset of units are accessible for measurement. The other, inaccessible, units are referred to as "hidden" in this thesis. In a realistic setup, an immediate question is how many hidden units exist: In a network of interconnected neurons, for example, we may ask how many other neurons are affecting those that are measured. Analogously, it might not be clear at all how many other genes impact the expression levels of those genes that are monitored in a gene regulatory network. Yet, there is no theory that reliably quantifies the number of hidden units in network dynamical systems.

This thesis is structured as follows. In Chapter 2, we introduce the basic notion of network dynamical systems. We give a brief historical introduction to the concept of networks (Sec. 2.1) and formalize our view on them (Sec. 2.2). We then introduce the concept of dynamical systems which is widely used among physicists and mathematicians in the field of complex systems (Sec. 2.3). We show how linear stability analysis allows to gain an insight into the stability of fixed points and other, possibly desired, dynamical states of complex systems in Sec. 2.4. We introduce this concept not only for the purpose of stability assessment: As we will show in the following chapters of this thesis, linearization of dynamical systems in a small vicinity of some reference point in state space helps us to explore both, fluctuation spreading in power grids and the detection of hidden units. In Sec. 2.5, we show how coupling dynamical systems on networks leads to the powerful concept of network dynamical systems. As an example, we demonstrate how the interaction of dynamics and structure promotes or hinders the emergence of collective dynamical states such as symmetric fixed points or full synchronization. To conclude this section, we introduce the Kuramoto model to explore the effect of phase locking, that is the synchronization process that takes place in power grids.

In Chapter 3, we present our view of wind power fluctuations in power grids. We begin with a discussion on statistical properties of turbulent flows in Sec. 3.1. Further, we demonstrate how the fluctuations of atmospheric turbulence impact wind power generation (Sec. 3.2). Finally, we introduce the synchronous motor model of power grids which captures the short-term response of high-voltage AC grids to perturbations and constitutes the basis of our further analysis of fluctuation spreading in power grids (Sec. 3.3) and provide technical details on our frequency measurement setup (Sec. 3.4).

The following Chapters 4–6 comprise the original manuscripts of the papers published prior to the publication of this thesis. To maintain the original character of the articles, we keep their structure. However, we adjusted the formatting and added some additional references to other chapters in this thesis. In Chapter 4, we show how the short-term fluctuations of locally measured grid frequency time series increase with increasing share of wind power fed to the grid and provide a model for their increment distributions. Motivated by this finding, we performed a second measurement of the grid frequency in another region with less wind power injection than in the first region (Chapter 5). We find that the effect of wind power on the frequency fluctuations cannot be seen in the second measurement. Further, we analytically derive a theory for the propagation of fluctuations in power grids in terms of frequency increment statistics. We evaluate our results as a function of the system parameters of the power grid. In Chapter 6, we provide a novel theory for the detection and quantification of hidden units in network dynamical systems. We demonstrate the successful inference of hidden units in various systems, in particular in coupled Kuramoto oscillators. We discuss our results and give an outlook on further research in Chapter 7.

2 NETWORK DYNAMICAL SYSTEMS

If we think of a network simply as a system of interconnected entities, many examples instantly come to our minds: Transportation networks such as a railway system, communication networks such as the telephone system, or even biological networks such as interconnect neurons in human brains [10, 51]. However, apart from systematically grouping these systems under the term "network", what are key methods and results from network science that lead to substantial scientific progress in a such broad range of disciplines? To understand the interdisciplinary power of networks, we give a brief historic introduction to the field and then provide the formal definitions. Further, we introduce the concept of dynamical systems and demonstrate how coupling dynamical systems on networks gives insights to the interplay of dynamics and structure of complex networked systems.

2.1 A BRIEF HISTORY

In 1741, Leonhard Euler published his famous solution to the problem of the seven bridges in Königsberg[1] [52, 53]. The sketch in his original manuscript, Fig. 1, shows the branches of river Pregel, dividing the city into four domains (A-D) connected by seven bridges. The problem he picked up from discussions with the inhabitants was the following: Is it possible to take a walk through all domains in the city using each bridge *exactly* once? In Ref. [53], E. Estrada gives an interesting interpretation which we would like to follow here: Euler was not so much interested in the solution itself (which probably had only limited relevance) but more in the fact that by then no mathematical concept existed to solve the problem except for explicit listing of all possible paths. He solved the problem (which he referred to as the "geometry of position") with a conceptually new answer which lies in the number of bridges connected to each domain: An aforementioned walk crossing all bridges once is always possible if an even (nonzero) number of bridges ends in each domain. If there are domains with odd numbers of ending bridges, the walk is only possible if there are exactly two such domains which form starting and ending point of the walk. Otherwise, the walker would pass by domains with odd number of bridges during his walk that he would have to enter *and* leave– which is impossible if bridges must be used exactly once.

1 The today's Kaliningrad in Russia. Due to destruction in World War II, the modern city has a different number of bridges than in 1741.

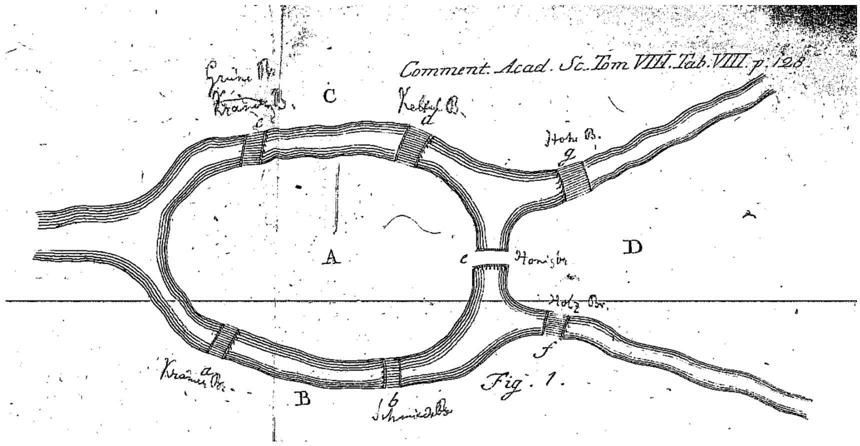

Figure 1: Original sketch of the seven Königsberg bridges from Lenhard Euler [52] in 1741. The Pregel river divides the city into four domains (A-D). Can you find a path through all domains in the city taking each bridge exactly once?

Euler reduced the complex problem to a new conceptual thinking which we refer to as network, or graph, theory today. Another example, also taken from Ref. [53], are the early works of Gustav Kirchhoff [54], who derived his famous laws for electricity networks from the finding that the current flowing into some point needs to flow out of the same point again. Other applications of network theory where found in molecule structures in the 19th century [53]. Instead of discussing further examples in detail, we now provide the formal definitions and notations of networks that we need for our further analyses.

2.2 FORMAL DEFINITIONS

So far, we have considered a network simply as a system of interconnected entities. We now want to formally elaborate the concept of networks and provide basic definitions and notations of networks [10, 53, 55]. We define the entities as *nodes* or *units* and the connections as *links*. Sometimes the entities are also referred to as *vertices* connected by *edges*. In the mathematical literature, a network is called *graph* and the corresponding field is referred to as *graph theory*.

The *adjacency matrix* $A \in \mathbb{R}^{N \times N}$ comprises the core information about the network structure of $N \in \mathbb{N}$ nodes. It is defined as

$$A_{ij} := \begin{cases} 1, \text{ if a link from node } j \text{ to } i \text{ exists, and} \\ 0, \text{ if not.} \end{cases} \tag{1}$$

A network can be either *directed* or *undirected*. In the undirected case, a link from i to j implies a link from j to i; the adjacency matrix is hence symmetric ($A = A^T$). In directed networks, a link from i to

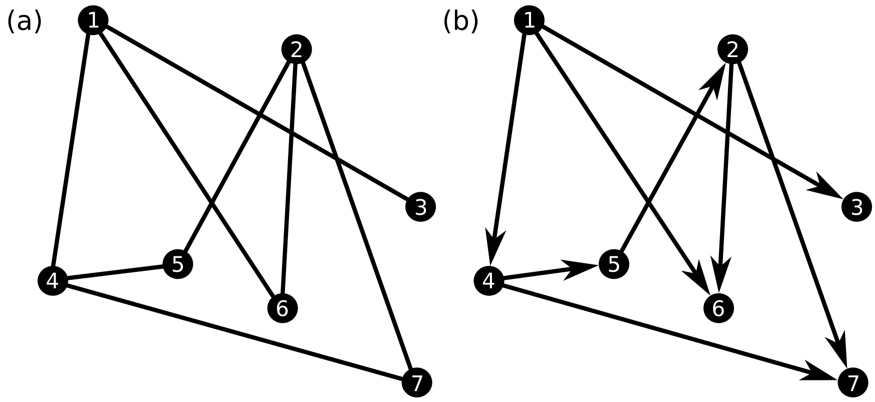

Figure 2: Sketch of an example network with $N = 7$ numbered nodes and *(a)* undirected and *(b)* directed links. In the undirected case, the network is connected, because there is a path between any pair (i, j) of nodes. Further, the adjacency matrix is symmetric ($A = A^T$). In the directed example, the network is *not* strongly connected because not all pairs (i, j) are connected by directed paths. Note, for example, that there is no directed path from node 2 to node 4 (even though a path from 4 to 2 exists). Further, the adjacency matrix is not symmetric, as can be seen from $A_{74} = 1$ and $A_{47} = 0$.

j may well exist without a link in the opposite direction and hence, in general, $A \neq A^T$. Further, the links may be not equally weighted; some can be "stronger" than others. In this case, the adjacency matrix is weighted which results in entries different from 1 for existing links (but still 0 for absent links).

The number of links that are adjacent to a node i is called the *degree* $d(i)$ of node i. In the undirected, unweighted case it simply follows from

$$d(i) = \sum_{j=1}^{N} A_{ij}. \tag{2}$$

In the directed case, we differentiate between the sum of all incoming links (*in-degree*) and of all outgoing links (*out-degree*).

A *path* is defined as a sequence of connected nodes in which each node appears only once. It can be seen as a walk through the network which passes each node only once. Consequently, the *shortest path distance* $d(i, j)$ is defined as the length of the shortest path between nodes i and j. A network in which a path exists for each pair of nodes (i, j) is called *connected*. A directed network is referred to as *strongly connected* if for each pair (i, j) a directed path from i to j *and* from j to i exists.

We visualize these important definitions in Fig. 2. Until this point, our discussion was focused on structure. We now introduce the concept of *dynamical systems* to include time-dependent behavior of complex networked systems in our description.

2.3 DYNAMICAL SYSTEMS

Dynamical systems model the evolution of a broad range of (possibly complex) systems. Indeed, the definition of the term itself can be as general as in Ref. [56]: "A dynamical system is a mathematical formalization for any *fixed rule* that describes the dependence of the position of a point in some *ambient space* on a *parameter*." With this definition, the construction of arbitrarily abstract systems is possible (as probably intended by the authors), however, in this work we will restrict ourselves to cases where the *parameter* is "time", the *ambient space* is referred to as "state space", i. e. the set of all possible states the system can be in at any parameter value, and the *fixed rule* is expressed by an ordinary differential equation (ODE) [56]. With these specifications in mind, we may define a *dynamical system* as the triple $(S, \mathbb{R}^+, \Phi)$ comprising the state space S, the time domain $\mathbb{R}^+$, and a flow

$$\Phi : \mathbb{R}^+ \times S \to S \tag{3}$$

which describes the evolution of the ODE system

$$\dot{\mathbf{x}} = \mathbf{F}(\mathbf{x}). \tag{4}$$

Here, $\mathbf{x}(t) = [x_1(t), \dots, x_n(t)] \in S$ is the state vector of the system at time t, $\mathbf{F} : S \to S$ a smooth function, and $\dot{\mathbf{x}} = d\mathbf{x}/dt$. The flow Φ is a formal notation of the solution of the initial value problem (4) with $\mathbf{x}(t = 0) = \mathbf{x}_0$:

$$\mathbf{\Phi}_t(\mathbf{x}_0) = \mathbf{x}(t). \tag{5}$$

It has the following properties [57]: *(i)* $\mathbf{\Phi}_0(\mathbf{x}_0) = \mathbf{x}_0$, *(ii)* $\mathbf{\Phi}_{t_1+t_2}(\mathbf{x}_0) = \mathbf{\Phi}_{t_1}(\mathbf{\Phi}_{t_2}(\mathbf{x}_0))$, and *(iii)* $\mathbf{\Phi}_t(\mathbf{x}_0)$ is a differentiable map for $t \in \mathbb{R}^+$.

2.4 LINEAR STABILITY ANALYSIS

Let us consider a simple example of a dynamical system described by a linear ODE with $\mathbf{F}(\mathbf{x}) = M\mathbf{x}$, where $M \in \mathbb{R}^{N \times N}$ is a constant matrix and $\mathbf{x} \in \mathbb{R}^N$. Such a system is called *linear time-invariant (LTI)* or *linear autonomous* [56]:

$$\dot{\mathbf{x}} = M\mathbf{x}. \tag{6}$$

Clearly, $\mathbf{x}^* = [0, \dots, 0]^T$ is a fixed point, that is a stationary solution $\mathbf{x}(t) = \mathbf{x}^*$ for all times if $\mathbf{x}_0 = \mathbf{x}^*$. The key question now is how we can judge if small perturbations of $\mathbf{x}(t) = \mathbf{x}^*$ will lead to a relaxation of $\mathbf{x}(t)$ back to $\mathbf{x}^*$ or rather to completely different behavior such as divergence in one or more components x_i. Such small perturbations are omnipresent in real-world problems, often induced by thermal noise [58]. In the linear case, we have the advantage that the general solution $\mathbf{x}(t)$ for initial value $\mathbf{x}_0$ is given by

$$\mathbf{x}(t) = \exp(Mt)\mathbf{x}_0, \tag{7}$$

where $\exp(\cdot)$ denotes the matrix exponential function [56]. In analogy to the scalar-valued exponential function, $\exp(Mt)$ converges to $[0, \ldots, 0]^T$ for $t \to \infty$, if all eigenvalues λ_n of M have negative real part, $\Re(\lambda_n) < 0$ for all $n = 1, \ldots, N$. Hence, we find that in this case, for linear systems, $\mathbf{x}^* = [0, \ldots, 0]^T$ is a *stable fixed point*, that is the system asymptotically approaches $\mathbf{x}^*$ irrespective of the initial conditions. If, in contrast, at least one eigenvalue λ_k has positive real part, $\Re(\lambda_k) > 0$, then $\mathbf{x}^* = [0, \ldots, 0]^T$ is an *unstable fixed point* which the system will leave for any finite perturbation. Purely imaginary eigenvalues, $\Re(\lambda_k) = 0$, can lead to more complex behavior such as periodic motion. However, their treatment is more difficult and system-dependent [56, 59].

Real-world problems are rarely linear. For a nonlinear system in the sense of Eq. (4), it can be challenging to even find a fixed point $\mathbf{x}^*$. If found, it fulfills

$$\mathbf{F}(\mathbf{x}^*) = [0, \ldots, 0]^T. \tag{8}$$

For a small perturbation $\boldsymbol{\epsilon}(t)$ such that $\mathbf{x}(t) = \mathbf{x}^* + \boldsymbol{\epsilon}(t)$, we find

$$\dot{\mathbf{x}} = \dot{\boldsymbol{\epsilon}} = \mathbf{F}(\mathbf{x}^* + \boldsymbol{\epsilon}(t)). \tag{9}$$

If we want the system to asymptotically approach $\mathbf{x}^*$ with $t \to \infty$, we need $\boldsymbol{\epsilon}(t)$ to decay to zero with $t \to \infty$. If the initial perturbation $\boldsymbol{\epsilon}(0)$ is small enough so that the linear term in the Taylor expansion of $\mathbf{F}(\mathbf{x})$ centered on $\mathbf{x}^*$ dominates, we find

$$\dot{\boldsymbol{\epsilon}} \approx D\mathbf{F} \cdot \boldsymbol{\epsilon}(t), \tag{10}$$

where we introduced the Jacobian matrix $D\mathbf{F}_{ij} = \partial F_i / \partial x_j |_{\mathbf{x}^*} \in \mathbb{R}^{N \times N}$ evaluated at $\mathbf{x}^*$. Eq. (10) now has the form of Eq. (6) and we can generalize the stability criteria deduced above for M to the local linearization $D\mathbf{F}$, that is the *Poincaré-Lyapunov Theorem* [56]: If all eigenvalues of $D\mathbf{F}$ have negative real part, then $\mathbf{x}^*$ is locally asymptotically stable. If at least one eigenvalue has positive real part, then $\mathbf{x}^*$ is unstable.

2.5 NETWORK DYNAMICAL SYSTEMS

We have introduced the concept of networks to capture structural properties in terms of an adjacency matrix A. We have seen how dynamical systems can be modeled in terms of ODEs and how the stability criteria of fixed points $\mathbf{x}^*$ can be deduced. The purpose of *network* *dynamical systems* is to link dynamics with structure. A convenient notation is the following:

$$\dot{x}_i = f_i(x_i) + \sum_{j=1}^{N} A_{ij} g_{ij}(x_i, x_j) \tag{11}$$

[10], where f_i is a smooth function that models the local dynamics at each node and g_{ij} is another smooth function modeling the coupling among nodes. Note that for the moment, we use heterogeneous f_i and g_{ij} for the nodes i. Mathematically speaking, Eq. (11) has the form of Eq. (4) with nonlinear function $\mathbf{F}(\mathbf{x})$. However, the notation (11) allows us to reveal the interplay between structure and dynamics; as we will see in the following.

2.5.1 *Symmetric fixed points*

The stability of fixed points $\mathbf{x}^* = [x_1^*, \dots, x_N^*]$ of heterogeneous systems like (11) can generally be assessed with the techniques discussed above. To obtain a more systematical insight, let us now consider an example systems with homogeneous dynamics $f = f_i$ and $g = g_{ij}$ for all i and j and symmetric fixed point $\mathbf{x}^* = [x^*, \dots, x^*]$ on an undirected, unweighted network ($A = A^T$) without self-links ($A_{ii} = 0$ for all i) [10]:

$$\dot{x}_i = f(x_i) + \sum_{j=1}^{N} A_{ij} g(x_j) \tag{12}$$

We have further restricted the coupling to act only on node j and not on node i itself. If we introduce a small perturbation of the system close to the fixed point, $\mathbf{x}(t) = \mathbf{x}^* + \boldsymbol{\epsilon}(t)$, we find

$$\dot{\boldsymbol{\epsilon}} = (\alpha I_N + \gamma A)\boldsymbol{\epsilon}, \tag{13}$$

where I_N is the $N \times N$-identity matrix, $\alpha = \partial f(y)/\partial y|_{x^*}$ and $\gamma = \partial g(y)/\partial y|_{x^*}$. Just as before, the asymptotic stability of the symmetric fixed point $\mathbf{x}^*$ depends on the eigenvalues of $\alpha I_N + \gamma A$. If $\mathbf{v}_k$ is an eigenvector of A with eigenvalue μ_k, it is also an eigenvector to $\alpha I_N + \gamma A$ with eigenvalue $\alpha + \gamma\mu_k$. Hence, $\mathbf{x}^*$ is stable if

$$\alpha + \gamma\mu_k < 0 \tag{14}$$

for all k [10]. Because $A = A^T$ and $A \in \mathbb{R}^{N \times N}$, all eigenvalues μ_k of A are real. Further, there are positive as well as negative eigenvalues[2]. To fulfill (14), $\alpha < 0$. This is an intuitive result, because it states that the local dynamics is stable in $\mathbf{x}^*$. We then find $-\alpha/\gamma < \mu_k$ if $\gamma < 0$

2 In networks without self-links, $A_{ii} = 0$ for all i. Hence $\mathrm{tr}(A) = 0 = \sum_{k=1}^{N} \mu_k$. If there is at least one link in the network, there must be both negative and positive eigenvalues.

and $-\alpha/\gamma > \mu_k$ if $\gamma > 0$. If we denote $\mu_1 > 0$ as the largest and $\mu_N < 0$ as the smallest eigenvalue, we find [10]

$$\frac{1}{\mu_N} < -\frac{\gamma}{\alpha} < \frac{1}{\mu_1}. \tag{15}$$

Condition (15) is referred to as *master stability condition*. It can take much more complicated forms if not all the aforementioned conditions apply, but we deduced this explicit example to demonstrate the interplay between structure and dynamics in network dynamical systems: While $\alpha = \partial f(y)/\partial y|_{x^*}$ and $\gamma = \partial g(y)/\partial y|_{x^*}$ depend only on the local and coupling dynamics, respectively, the eigenvalues μ_k depend only on the adjacency matrix, i.e. the network structure. Whenever (15) is fulfilled, $\mathbf{x}^*$ is linearly stable.

Example 1: Nonlinear coupling function. Let us consider the network dynamical system

$$\dot{x}_i = -x_i + \sum_{j=1}^{N} A_{ij} \cdot K \frac{x_j}{1 + x_j}. \tag{16}$$

In fact, Eq. (16) is a simple model for biochemical reaction networks, the Michaelis-Menten Kinetics [5], in which $x_i(t)$ specifies the chemical abundance or expression level of molecular species i. It shows an asymmetric fixed point and we will later in this thesis use deviations from such an asymmetric fixed point to infer hidden nodes in networks (Chapter 6). However, let us for the moment consider the symmetric fixed point $\mathbf{x}^* = [0, \ldots, 0]^T$ which has only subordinate relevance in biochemical reactions, but nicely illustrates our previously derived condition (15) from a mathematical perspective. We choose a homogeneous coupling constant K on the unweighted adjacency matrix A. For the symmetric fixed point $\mathbf{x}^* = [0, \ldots, 0]^T$, we have $\alpha = -1$ and $\gamma = K$. We integrate Eq. (16) on a small network of five nodes, Fig. 3 a, and show the eigenvalues μ_k of A in Fig. 3 b. The master stability condition, Eq. (15), reads

$$-\frac{1}{1.7491} \approx -0.57 < K < \frac{1}{2.6855} \approx 0.3724. \tag{17}$$

In this example, the structural properties of the network, expressed by the eigenvalues μ_k of the adjacency matrix A, lead to the fact that $\mathbf{x}^*$ becomes instable once the coupling K exceeds $K = 0.3724$. For illustration, we show the evolution of $x_i(t)$ for the unstable ($K = 0.4$, Fig. 3 c) and stable regime ($K = 0.3$, Fig. 3 d).

2.5.2 *Synchronous trajectories*

Network dynamical systems can show much more complex collective phenomena than simple symmetric fixed points $\mathbf{x}^*$. One important example is *full synchronization*, where the trajectories $x_i(t)$ of all nodes

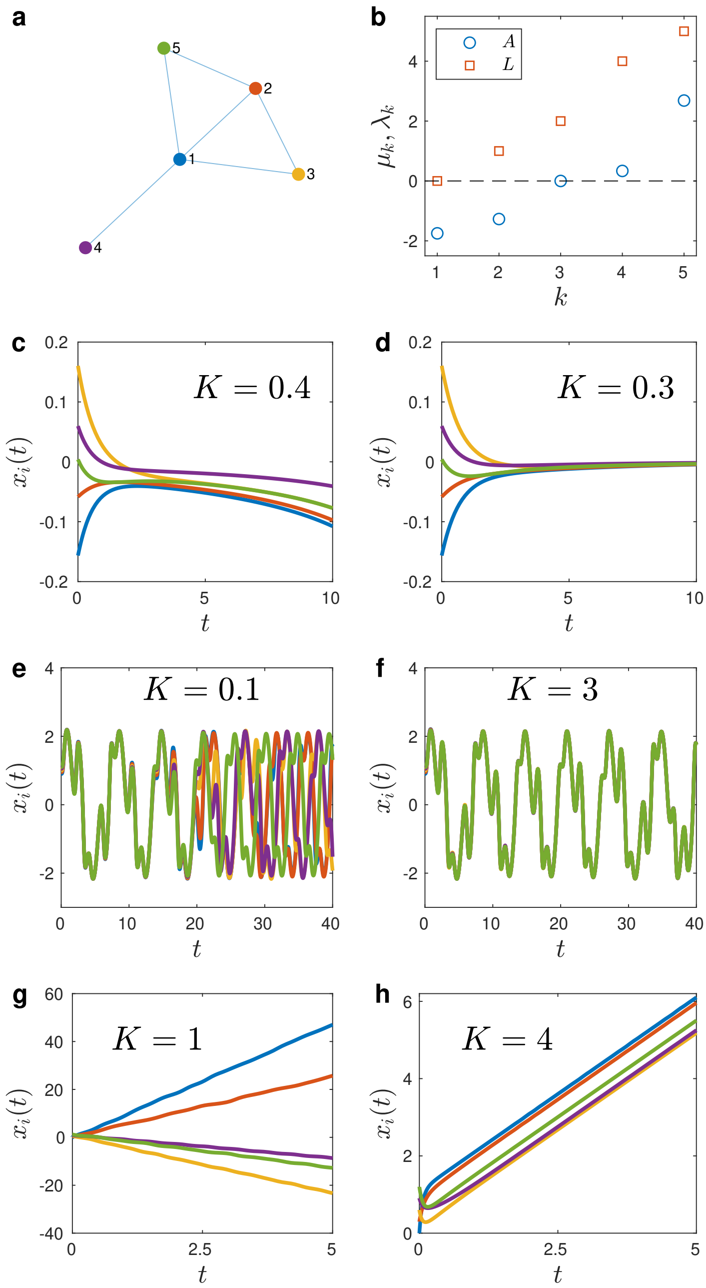

Figure 3: **Examples of collective dynamics in network dynamical systems** *(a)* Example network of five nodes. *(b)* Eigenvalues of the corresponding adjacency matrix A and graph Laplacian L. *(c,d)* In network with nonlinear coupling function, Eq. (16), the symmetric fixed point $\mathbf{x}^* = [0, \ldots, 0]^\top$ becomes instable, once the coupling K exceeds $K_c = 0.3724$. Line colors correspond to node colors in (a). *(e,f)* Diffusively coupled van der Pol systems, Eq. (26), fully synchronize for couplings stronger than $K_c = 1.232$. *(g,h)* Kuramoto oscillators coupled on the network, Eq. (37), phase-lock if $K > K_c = 3.25$; according to the condition derived in [60].

are exactly equal, $x_i(t) = s(t)$ for all i [12]. Note that $s(t)$ is still a time-dependent, possibly chaotic, trajectory and no stationary fixed point. A common notation to analyze synchronization in network dynamical systems is the following [12]:

$$\dot{x}_i = f(x_i) + K \cdot \sum_{j=1}^{N} A_{ij}(g(x_j) - g(x_i)). \tag{18}$$

Here, we have introduced a coupling strength $K \in \mathbb{R}$ (which could technically be absorbed in g) and a slightly different coupling $g(x_j) - g(x_i)$ than before. However, we can re-write Eq. (18) as

$$\begin{aligned}
\dot{x}_i &= f(x_i) + K \cdot \sum_{j=1}^{N} A_{ij} g(x_j) - K \cdot \sum_{j=1}^{N} A_{ij} g(x_i) \\
&= f(x_i) + K \cdot \sum_{j=1}^{N} A_{ij} g(x_j) - K \cdot g(x_i) \sum_{j=1}^{N} A_{ij} \\
&= f(x_i) + K \cdot \sum_{j=1}^{N} A_{ij} g(x_j) - K \cdot g(x_i) d(i) \\
&= f(x_i) - K \cdot \sum_{j=1}^{N} (d(i)\delta_{ij} - A_{ij}) g(x_j) \\
&=: f(x_i) - K \cdot \sum_{j=1}^{N} L_{ij} g(x_j),
\end{aligned} \tag{19}$$

which has the form of Eq. (12) except that here, in Eq. (19), the newly defined matrix

$$L_{ij} := d(i)\delta_{ij} - A_{ij}, \tag{20}$$

with Kronecker-δ_{ij} and degree $d(i)$ of node i, takes over the role of the adjacency matrix A_{ij}. L is called the *graph Laplacian matrix* of the network [10, 12].

In fact, L is closely related to the Laplacian operator $\Delta := \sum_i \partial_i^2$ in continuous systems: Let us consider for a moment the diffusive spreading of a scalar quantity $\phi(u, v, t)$ on a two-dimensional space $(u, v) \in \mathbb{R}^2$ described by the heat equation

$$\partial_t \phi = \Delta \phi = \partial_u^2 \phi + \partial_v^2 \phi. \tag{21}$$

If we discretize the partial derivation in space, we find

$$\begin{aligned}
\partial_t \phi(u, v, t) = \lim_{h \to 0} \Bigg[&\frac{\phi(u-h, v, t) + \phi(u+h, v, t)}{h^2} \\
&+ \frac{\phi(u, v-h, t) + \phi(u, v+h, t)}{h^2} \\
&- \frac{4\phi(u, v, t)}{h^2} \Bigg].
\end{aligned} \tag{22}$$

The Laplace operator Δ sums up the values of ϕ at neighboring positions in space in all 4 directions with infinitesimal distance h and subtracts 4 times the value of ϕ at the position itself. If we now look at the simplest version of Eq. (19) without local dynamics ($f(x) = 0$) and linear coupling ($g(x) = x$), we find that $(-L)$ is doing the exact same thing– except that the summation runs over all adjacent nodes. Eq. (19) hence describes a reaction-diffusion process on a network [10].

The Laplacian L of an undirected network has some important properties of which we only list a few: First, it always has one eigenvalue $\lambda_1 = 0$ with corresponding eigenvector $\mathbf{1} = [1, \dots, 1]^T$. This can be deduced straight-forwardly from the definition of L and the nodal degree $d(i)$ (Eq. (2)). Second, all other eigenvalues are real ($L = L^T$) and positive. A convenient notation is hence $\lambda_1 = 0 \leqslant \lambda_2 \leqslant \dots \leqslant \lambda_N$. And, third, λ_2 is referred to as *algebraic connectivity*: If $\lambda_2 \neq 0$, the network is connected, otherwise it has at least two disconnected components [10].

But now back to our system (19). How can we find a condition under which the trajectories $x_i(t)$ converge to the same synchronous trajectory $s(t)$? We begin with an ansatz which generalizes from the analysis of symmetric fixed points. We consider a time-dependent perturbation $\epsilon_i(t)$ of the synchronous trajectory, $x_i(t) = s(t) + \epsilon_i(t)$, and write [12]

$$\begin{aligned}\dot{\boldsymbol{\epsilon}}(t) &= f(\mathbf{s}(t) + \boldsymbol{\epsilon}(t)) - K \cdot Lg(\mathbf{s}(t) + \boldsymbol{\epsilon}(t)) \\ &\approx \left.\frac{\partial f(y)}{\partial y}\right|_{\mathbf{s}(t)} \boldsymbol{\epsilon}(t) - K \cdot L \left.\frac{\partial g(y)}{\partial y}\right|_{\mathbf{s}(t)} \boldsymbol{\epsilon}(t).\end{aligned} \tag{23}$$

Eq. (23) is a variational equation in $\boldsymbol{\epsilon}(t)$ and much more difficult to treat than Eq. (13); note that the derivatives have to be evaluated along the trajectory $\mathbf{s}(t)$. Projecting Eq. (23) into the eigenspace of L, $Q\mathbf{w}(t) = \boldsymbol{\epsilon}(t)$ with $Q \in \mathbb{R}^{N \times N}$ the matrix of eigenvectors of L, yields [12]

$$\dot{\mathbf{w}}(t) = \left.\frac{\partial f(y)}{\partial y}\right|_{\mathbf{s}(t)} \mathbf{w}(t) - K \cdot \operatorname{diag}(\lambda_1, \dots, \lambda_N) \left.\frac{\partial g(y)}{\partial y}\right|_{\mathbf{s}(t)} \mathbf{w}(t) \tag{24}$$

or, element-wise,

$$\dot{w}_i(t) = \left[\left.\frac{\partial f(y)}{\partial y}\right|_{\mathbf{s}(t)} - K\lambda_i \left.\frac{\partial g(y)}{\partial y}\right|_{\mathbf{s}(t)} \right] w_i(t). \tag{25}$$

If all trajectories $x_i(t)$ converge to $s(t)$, all eigenmodes $w_i(t)$ for $i > 1$ must converge to zero for $t \to \infty$. For convenience, we define $\sigma_i := K\lambda_i$. Note that the mode w_1 corresponds to the eigenvector $\mathbf{1} = [1, \dots, 1]^T$ which represents a global shift of all nodes and does therefore not affect the synchronized state. For all other modes, one has to numerically compute the largest Lyapunov exponent $\Lambda_{max}(\sigma)$ of the variational equation (25) as a function of σ. All modes $w_i(t)$ damp out if $\Lambda_{max}(\sigma_i) < 0$ for all $\sigma_i = K\lambda_i$, $i = 2, \ldots, N$. $\Lambda_{max}(\sigma)$ is referred to as the *master stability function* [9, 12].

Example 2: Forced van der Pol system. Consider the system

$$\ddot{x}_i = -x_i + d(1 - x_i^2)\dot{x}_i + F\sin(\eta t) + K \cdot \sum_{j=1}^{N} A_{ij}(x_j - x_i) \tag{26}$$

of diffusively coupled van der Pol systems with $d = 3$, $F = 15$, and $\eta = 4.065$ [61]. In fact, this is a second order differential equation. However, if we define two-dimensional nodal dynamics $\mathbf{x}_i = [\dot{x}_i, x_i]^T$, it can be brought to the form of Eq. (18) and the derivation of the Master Stability Function $\Lambda_{max}(\sigma)$ generalizes straight-forwardly for multidimensional nodal dynamics [12]. The numerical calculations to obtain $\Lambda_{max}(\sigma)$ were performed in Ref. [61] with the result that $\Lambda_{max} < 0$ for $\sigma > 1.232$. Hence, for a stable full synchronization, we need to fulfill

$$K\lambda_i > 1.232 \tag{27}$$

for all nonzero Laplacian eigenvalues λ_i, $i \geqslant 2$. Given that in our example system, Figs. 3 a&b, $\min_{i \geqslant 2} \lambda_i = 1$, full synchronization occurs for $K > 1.232$. As in the previous example, we show the evolution of the nodal dynamics in the unstable ($K = 0.1$, Fig. 3 e) and stable case ($K = 3$, Fig. 3 f).

2.5.3 *Phase locking of coupled oscillators*

Master stability functions, as discussed in the previous chapter, are powerful tools due to their broad applicability. However, non-trivial and possibly expensive numerical calculations are necessary to obtain Lyapunov exponents of systems like Eq. (25). Hence, the insight to the systematic dependence of synchronization on structure and dynamics is limited. A deeper theoretical insight is obtained from a model proposed by Kuramoto [13, 17]. The dynamics read [13]

$$\dot{\theta}_i = \omega_i + \frac{K}{N}\sum_{j=1}^{N} \sin(\theta_j - \theta_i) \tag{28}$$

and model a set of N oscillators with phase $\theta_i(t)$ and natural frequency ω_i which are globally, i.e. all-to-all, coupled with coupling strength K/N. The natural frequencies ω_i are distributed according to a given probability density function, $\omega \sim g(\omega)$.

Kuramoto oscillators synchronize under certain circumstances. Let us first consider frequency synchronization, i.e. $\dot{\theta}_i(t) = \Omega$ for all i and t. Then, summing up Eq. (28) for all i yields

$$\sum_{i=1}^{N} \dot{\theta}_i = N\Omega = \sum_{i=1}^{N} \omega_i + \frac{K}{N} \sum_{i=1}^{N} \sum_{j=1}^{N} \sin(\theta_j - \theta_i) \tag{29}$$

Since $\sin(\theta_j - \theta_i) + \sin(\theta_i - \theta_j) = 0$, we find

$$\Omega = \frac{1}{N} \sum_{i=1}^{N} \omega_i. \tag{30}$$

The common frequency Ω is hence the average of the natural frequencies ω_i. However, the phases $\theta_i(t)$ are not necessarily the same everywhere. Let us go back to Eq. (28) for some fixed i in the case where all frequencies are synchronous ($\dot{\theta}_i(t) = \Omega$):

$$\Omega = \omega_i + \frac{K}{N} \sum_{j=1}^{N} \sin(\theta_j - \theta_i) \tag{31}$$

Synchronized phases θ_i would imply $\theta_j - \theta_i = 0$ and hence $\Omega = \omega_i$ for all i. Thus, we find that phase synchronization in the Kuramoto model is only possible for systems with identical oscillators, $\omega_i = \Omega$.

The case where all frequencies are the same, $\dot{\theta}_i = \Omega$ for all i, but the phases θ_i show a constant phase difference $\theta_j - \theta_i =: \Delta_{ij} = \text{const.}$ is referred to as the *phase-locked* or *frequency-synchronized* state [62]; in contrast to the previously discussed full synchronization.

In the case of global coupling, Eq. (28), the transition from asynchronous to phase-locked dynamics can be derived analytically [13]: Let us consider the order parameter

$$Z(t) := \frac{1}{N} \sum_{j=1}^{N} \exp(i\theta_j(t)). \tag{32}$$

By definition, $|Z| \leqslant 1$. Z measures the coherence of the phases $\theta_i(t)$: If all phases evolve asynchronously with independent frequencies, they will cancel out each other and $|Z| \to 0$. If coupling K is increased, more and more oscillators will, eventually, join the phase-locked cluster and sum up coherently; resulting in $|Z| \to 1$. Defining $R := |Z|$ and $\Psi := \arg(Z)$ allows us to formulate a mean field theory for the system (28):

$$\dot{\theta}_i = \omega_i + KR\sin(\Psi - \theta_i). \tag{33}$$

We omit the detailed calculations here and present only the result [13] manifested in a self-consistent equation for R:

$$R = KR \int_{-\pi/2}^{\pi/2} d\varphi \cos^2(\varphi) g\left[KR\sin(\varphi)\right]. \tag{34}$$

$R \searrow 0$ yields

$$K_c = \frac{2}{\pi g(0)}, \tag{35}$$

which is the critical coupling above which R starts to grow because more and more oscillators phase-lock and sum up coherently. Close to K_c, R grows, in leading order, as

$$R \sim \sqrt{\frac{-16(K-K_c)}{\pi K_c^4 g''(0)}}, \tag{36}$$

that is $R \propto (K-K_c)^{1/2}$ – in analogy to a second-order phase transition [13].

The original model (28), as proposed by Kuramoto, can be generalized to complex networks by replacing the global coupling in Eq. (28) with an adjacency matrix A [13]:

$$\dot{\theta}_i = \omega_i + K \sum_{j=1}^{N} A_{ij} \sin(\theta_j - \theta_i) \tag{37}$$

In this case, analytical synchronization conditions for arbitrary topologies are rare and usually depend on the algebraic connectivity λ_2, or nodal degrees $d(i)$. For a summary of the state-of-the-art, we refer to Refs. [62] or [13]. Here, we present only one recent result which applies to a broad range of network types and was derived by Dörfler *et al.* in Ref. [60]. The authors define solutions $\{\theta_i(t)\}$ as *phase cohesive* if each pair of connected oscillators (i, j) has a bounded phase difference $|\theta_i - \theta_j| \leqslant \gamma < \pi/2$. Then, there exists a stable phase-locked and phase cohesive solution if

$$||L^\dagger \boldsymbol{\omega}||_{A,\infty} \leqslant \sin(\gamma), \tag{38}$$

where $L^\dagger$ denotes the Moore-Penrose pseudo inverse of the graph Laplacian L and $\boldsymbol{\omega} = [\omega_1, \dots, \omega_N]^T$. Further, for some state vector $\mathbf{x} \in \mathbb{R}^N$, $||\mathbf{x}||_{A,\infty} := \max_{(i,j)} |x_i - x_j|$ where (i, j) is a link in the network represented by A. $||\mathbf{x}||_{A,\infty}$ is hence the "worst-case dissimilarity" [60] for $\mathbf{x}$ over the links.

Example 3: Kuramoto oscillators on a network. We now couple Kuramoto oscillators, Eq. (37), on our example network, Figs. 3 a&b, with $\boldsymbol{\omega} = [10, 5, -5, -2, -3]^T$. We obtain

$$(KL)^\dagger \boldsymbol{\omega} = \frac{1}{K} L^\dagger \boldsymbol{\omega} = \frac{1}{K}[1.8, 1.3, -1.45, -1.2, -0.45]^T. \tag{39}$$

The largest difference of this result along an existing edge is hence $1/K(1.8 - (-1.45)) = 1/K \cdot 3.25$. If we formulate condition (38) in its least strict fashion, $\gamma = \pi/2$, we obtain that phase-locked behavior occurs for $K > 3.25$. In Figs. 3 g&f, we show asynchronous phase evolution for $K = 1$ and phase-locked evolution for $K = 4$, respectively.

3 FLUCTUATIONS OF WIND POWER IN POWER GRIDS

We begin this chapter with a discussion of basic properties of fluctuations in turbulent flows. Further, we show how wind turbines react to turbulent inflow conditions by comparing specific statistical properties of the power output of wind turbines to those of ideal turbulence. We will then introduce a simple power grid model which captures the dynamics of high-voltage AC grids and constitutes the basis for our further analysis of fluctuation spreading in power grids.

3.1 A STATISTICAL APPROACH TO TURBULENCE

Throughout this section, we follow the reasoning of Ref. [29]. The evolution of a velocity field $\mathbf{u}(\mathbf{x}, t)$ of an incompressible Newtonian fluid is governed by *Navier Stokes equation*:

$$\begin{aligned} \partial_t \mathbf{u}(\mathbf{x}, t) + (\mathbf{u}(\mathbf{x}, t) \cdot \nabla)\mathbf{u}(\mathbf{x}, t) \\ = -\nabla p(\mathbf{x}, t) + \nu\Delta\mathbf{u}(\mathbf{x}, t) + \mathbf{f}(\mathbf{x}, t), \end{aligned} \tag{40}$$

where ν denotes kinematic viscosity and $p(\mathbf{x}, t) = P(\mathbf{x}, t)/\rho$ the pressure field $P(\mathbf{x}, t)$ divided by the constant density ρ. $\mathbf{f}(\mathbf{x}, t)$ is a body acceleration term (such as gravity) [29].

Eq. (40) models the spatial and temporal evolution of a velocity field $\mathbf{u}(\mathbf{x}, t)$. Yet, in most cases, there is no general analytical solution known. Hence, the analysis of statistical properties of the velocity field $\mathbf{u}(\mathbf{x}, t)$ cannot be derived from an explicit solution of Eq. (40). However, why is it so difficult to derive, for example, the probability density function $p(|\mathbf{u}|, t)$ or at least moments thereof?

Let us consider the two-point correlator

$$C_{ij}(\mathbf{x}, \mathbf{x}', t) = \langle (u_i(\mathbf{x}, t) u_j(\mathbf{x}', t) \rangle \tag{41}$$

which comprises important statistical information on the flow: For $\mathbf{x} = \mathbf{x}'$, it gives the second-order moments of $p(|\mathbf{u}|, t)$ and for $\mathbf{r} = \mathbf{x} - \mathbf{x}'$, we obtain information on the correlation of the velocity field on scale $\mathbf{r}$. Directly from Eq. (40), one obtains

$$\begin{aligned}
&\frac{\partial}{\partial t}\langle(u_i(\mathbf{x},t)u_j(\mathbf{x}',t)\rangle + \sum_{k=1}^{3}\frac{\partial}{\partial x_k}\langle(u_k(\mathbf{x},t)u_i(\mathbf{x},t)u_j(\mathbf{x}',t)\rangle \\
&+ \sum_{k=1}^{3}\frac{\partial}{\partial x'_k}\langle(u_k(\mathbf{x}',t)u_i(\mathbf{x},t)u_j(\mathbf{x}',t)\rangle \\
&= -\frac{\partial}{\partial x_i}\langle(p(\mathbf{x},t)u_j(\mathbf{x}',t)\rangle - \frac{\partial}{\partial x'_j}\langle(p(\mathbf{x}',t)u_i(\mathbf{x},t)\rangle \\
&+ \nu[\Delta_x + \Delta_{x'}]\langle u_i(\mathbf{x},t)u_j(\mathbf{x}',t)\rangle + Q_{ij}(\mathbf{x},\mathbf{x}',t) \qquad (42)
\end{aligned}$$

[29]. Here, Q_{ij} denotes a source term which stems from the acceleration $\mathbf{f}$. The main difficulty arises from the fact that Eq. (42), whose solution would principally reveal C_{ij}, includes both second and third moments. In fact, one can show that each equation for the Nth moment depends on the $(N+1)$th moment as well– thus hindering a direct analytical solution for C_{ij}. This problem is referred to as the *closure problem of turbulence* [29].

In 1922, L.F. Richardson developed a phenomenological description of turbulent fluids [29, 63]: Stimulated by the observation that turbulent velocity fields consist of a multitude of eddies of different sizes which dynamically appear and decay, he presented his view of the *energy cascade*. In this model, energy is injected to the fluid at large spatial scales evoking large eddies of size L. Those rapidly become instable and decay into smaller eddies to which the energy of the original, large eddy is transferred. Thus, the energy is transferred down the cascade of ever smaller eddies until the structures become so small that the energy dissipates.

We will consider turbulent flows that are stationary, homogeneous, and isotropic. Stationarity is obtained if energy is injected with constant rate on large scales to maintain a stable energy cascade. Homogeneity, that is spatial invariance, states that the flow is large enough to minimize the impact of boundary conditions on scales $l \ll L$. Isotropy means rotational invariance. The two-point correlator $C_{ij}(\mathbf{x}, \mathbf{x}', t)$, Eq. (41), then only depends on distance $r = |\mathbf{r}| = |\mathbf{x} - \mathbf{x}'|$ and is stationary as well. Further, it is sufficient to consider only a single velocity component $u(\mathbf{x}, t)$:

$$C(r) = \langle u(\mathbf{x}+\mathbf{r}, t)u(\mathbf{x}, t)\rangle. \qquad (43)$$

We may then define the *integral length scale* L which was phenomenologically discussed above as

$$L := \int_0^\infty \frac{C(r)}{C(0)} dr \qquad (44)$$

[29]. Further, the length scale λ below which dissipation dominates is defined by the curvature of the parabolic decay of $C(r)$ close to $r = 0$ through

$$\frac{C(r)}{C(0)} = 1 - \frac{1}{2}\frac{r^2}{\lambda^2} \tag{45}$$

[29]. The length scale λ is referred to as the *Taylor length*. The scales $\lambda \ll l \ll L$ constitute the *inertial range*. In 1941, Kolmogorov postulated that within the inertial range, turbulent structures are homogeneous, isotropic and independent of dissipation effects [29, 64].

In the spectral domain, two-point correlations manifest in the spectral energy density $E(k)$, where k is a wave number. $E(k)$ quantifies the energy contained in structures of wave number k. One important result, independently obtained[1] by Obukhov [65], Kolmogorov [66], Heisenberg [67], and Weizäcker [68] is that $E(k)$ of the turbulent velocity field scales as

$$E(k) \propto k^{-\frac{5}{3}}. \tag{46}$$

Despite the various aforementioned discoverers, Eq. (46) is often referred to as the *Kolmogorov spectrum* of turbulence.

Of particular interest for our analysis of turbulent fluctuations is the statistics of increments. Let us define the longitudinal increment

$$\Delta_r u(\mathbf{x}, t) := \mathbf{e_r} \cdot (\mathbf{u}(\mathbf{x} + \mathbf{r}, t) - \mathbf{u}(\mathbf{x}, t)), \tag{47}$$

where $\mathbf{r}$ with $r = |\mathbf{r}|$ is the distance vector and $\mathbf{e_r}$ the unit vector in $\mathbf{r}$-direction. Due to the assumed isotropy, $\Delta_r u(\mathbf{x}, t)$ depends only on the distance r and not the spatial orientation. The moments of the longitudinal increments are called *structure functions*

$$S^n(r) := \langle \Delta_r u^n \rangle \tag{48}$$

of order n. Here, $\langle \cdot \rangle$ refers to statistical averaging. For $S^3(r)$, Kolmogorov derived one of the very few results directly from Navier Stokes:

$$S^3(r) = -\frac{4}{5}\langle \epsilon \rangle r \tag{49}$$

[29], where $\langle \epsilon \rangle$ is the mean energy dissipation rate. This is the famous *4/5 law* for turbulent flows which is valid for scales within the inertial range in which dissipation can be neglected. Further, Kolmogorov postulated self-similarity of the increment distributions. A probability density $p(\Delta_r u)$ is considered as self similar if it scales as

1 See Ref. [28], from where the original references were taken, for a historical discussion.

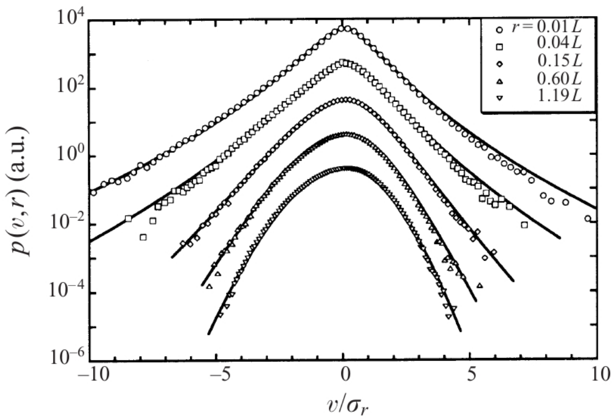

Figure 4: **Breaking of self-similarity of increment statistics.** Increment PDFs ($p(\Delta_r u) \equiv p(v, r)$) of velocity measurements in the turbulent region of a round free jet. Each PDF is shown in units of its respective standard deviation σ_r and vertically shifted to enhance differentiability. Spatial scales r are given in units of the integral length scale L. Figure reprinted from Ref. [69] with permission from Cambridge University Press.

$p(u, r) = \lambda^{\zeta} p(\lambda^{\zeta} u, \lambda r)$ with appropriate scaling parameter ζ. Figuratively speaking, this is the case when the increment distributions have the same shape for different scales r. For the structure functions, self similarity – together with Eq. (49) – results in

$$S^n(r) = C_n \langle \epsilon \rangle^{\frac{n}{3}} r^{\zeta_n} \tag{50}$$

with $\zeta_n^{K41} = n/3$. This is the main result from Kolmogorov in 1941 [29, 64].

Experimental results refute the hypothesis of self similarity of structure functions in the inertial range. Probability density functions $p(\Delta_r u/\sigma_r)$ of increments (in units of their respective standard deviations $\sigma_r = \langle \Delta_r u^2 \rangle$) follow an almost Gaussian distribution on large scales r and deform towards more heavy-tailed shapes on small scales r, Fig. 4. This effect is termed *intermittency* in turbulence research[2] [29].

The scaling of structure functions $S^n(r)$ with r has been a field of intensive research since Kolmogorv's results from 1941. In 1962, Kolmogorov replaced the mean dissipation rate $\langle \epsilon \rangle$ in his original theory by a log-normally distributed random variable. Therewith he obtained for the scaling exponent

$$\zeta_n^{K62} = \frac{n}{3} - \frac{\mu}{18} n(n-3), \tag{51}$$

2 We emphasize that the term "intermittency" has a different meaning in other disciplines and may, for example, also refer to intermittent availability of renewable energies or a specific behavior of dynamical systems [29].

[29, 70] where the constant μ was experimentally estimated as $\mu \approx 0.26$. While this nonlinear exponent ζ_n^{K62} fits experimental data better than $\zeta^{K41} = 1/3$, She and Leveque derived an even better fitting expression [29, 71]

$$\zeta_n^{SL} = \frac{n}{9} + 2\left(1 - \left(\frac{2}{3}\right)^{\frac{n}{3}}\right). \tag{52}$$

In summary, we have seen that statistical properties of turbulent velocity fields are difficult to obtain directly from Navier Stokes equation. Experiments show that such properties highly depend on the spatial scale r and are not self-similar. Increments $\Delta_r u$ characterize fluctuations in terms of velocity differences on a fixed scale r and underlie the effect of intermittency, that is the deformation of a Gaussian $p(\Delta_r u)$ on large scales towards heavy-tailed shapes of $p(\Delta_r u)$ with decreasing r. Several theoretical frameworks model the effect of intermittency decently, but not perfectly.

3.2 FLUCTUATIONS IN WIND POWER MEASUREMENTS

In the previous Sec. 3.1, we discussed non-Gaussian increment statistics of homogeneous and isotropic turbulence. While such theoretical analyses usually focus on spatial increments at fixed times, experimental setups often only allow to measure time-wise increments at a fixed spot of an Eulerian observer. However, if the measured velocity fluctuations are small compared to the mean velocity, Taylor's hypothesis [29] applies and properties of spatial increments translate into properties of time-wise increments. Even though the idealized conditions of homogeneous isotropic turbulence apply mainly to lab experiments, also wind speed measurements show non-Gaussian increment statistics on short timescales which deform towards less heavy-tailed shapes on larger scales, Fig. 5 a [23, 25, 26].

How do intermittent wind speed fluctuations affect the power production of wind turbines? Interestingly, time series of wind power generation show even more pronounced tails, Fig. 5 b [23, 25, 26]. In units of their respective standard deviations σ_τ, the $\tau = 1$ s increments of wind power last up to approximately $20\sigma_\tau$, while those of wind speed are smaller than $10\sigma_\tau$. However, the deformation towards a Gaussian distribution with increasing time lag τ is less obvious in the power time series.

Wind turbines convert kinetic energy of the wind into electric power. Modern turbines allow for variable rotational speed and decouple the rotating mechanical parts from the frequency of the alternating current fed to the grid through AC-DC-AC converters (see [25] with references therein). Such power converters apply complex control strategies to maximize the power output in a fluctuating wind field. In many cases, controllers freely follow wind speed variations and may

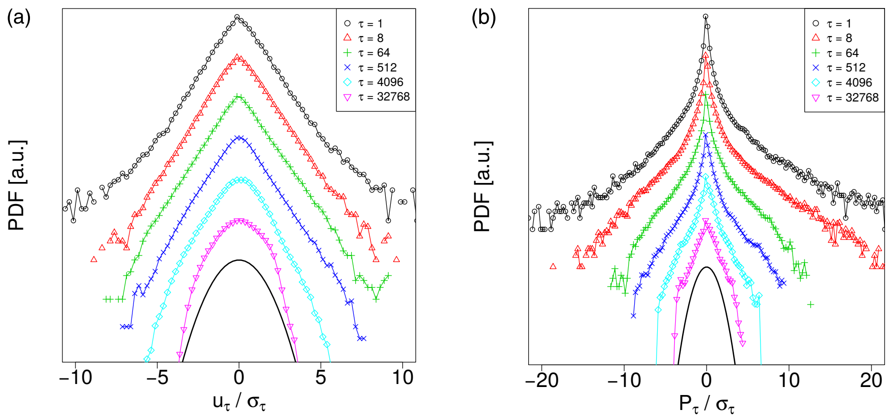

Figure 5: **Non-Gaussian increment statistics of wind speed and wind power measurements.** Increment PDFs of *(a)* wind speed measurements $\Delta_\tau u \equiv u_\tau$ and *(b)* the power output of a wind turbine $\Delta_\tau P \equiv P_\tau$ for different timescales (symbols, timescales τ in seconds). The Gaussian distribution is given as the solid reference curve. Each PDF is vertically shifted to enhance differentiability. Figures reprinted from Ref. [23] with permission from Springer Nature.

therewith transfer statistical properties of the incoming wind field to the power output [25].

Regardless of how exactly the controller is programmed, there is one principal argument why short-term fluctuations appear stronger in wind power than in wind speed measurements. In a laminar and incompressible flow with constant speed u and density ρ, the kinetic power $\tilde{P}_{\text{wind}}(u)$ which passes through a rotor plane A, perpendicular to the wind direction, is

$$\tilde{P}_{\text{wind}}(u) = \frac{d}{dt} E_{kin} = \frac{1}{2}\dot{m}u^2, \tag{53}$$

where $\dot{m} = \rho u A$ is the mass flow rate [23]. Inserting $\dot{m}$ yields

$$\tilde{P}_{\text{wind}}(u) = \frac{1}{2}\rho A u^3 \tag{54}$$

[23]. Eq. (54) relates wind speed u to theoretically available power $\tilde{P}_{\text{wind}}(u)$ through a power law with exponent 3. This nonlinear transformation can principally explain the different shapes between $p(\Delta_\tau u)$ and $p(\Delta_\tau P)$, see Fig. 5, by itself.

Non-Gaussian short-term fluctuations persist in the aggregated output of 12 turbines, Fig. 6 a. This is an experimental hint that the effect of geographic smoothing, that is the decrease of fluctuations due to aggregation of spatially distributed turbines, does not critically affect the shape of the short-term increment distributions. Further, we find the turbulent energy spectrum $E(k) \propto k^{-5/3}$, Eq. (46), in both, the power spectral density of wind speed and power output time series, Fig. 6 b. This indicates that the long-ranging spatial correlations

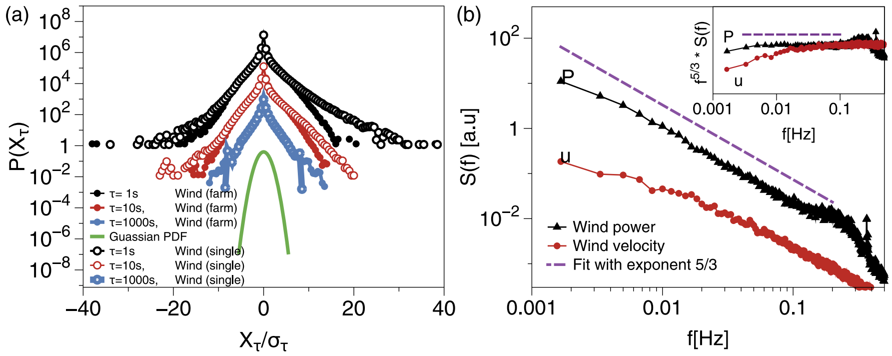

Figure 6: **Increment statistics of aggregated power output and power spectral densities.** *(a)* Increment PDFs $p(\Delta_\tau P \equiv X_\tau)$ of power production of a single turbine ($\circ$) and the aggregation of 12 turbines ($\bullet$) for different time lags τ in seconds. The Gaussian distribution is given as the solid reference curve. Each PDF is vertically shifted to enhance differentiability. *(b)* Power spectral densities of wind speed and power production time series in comparison to the turbulent energy spectrum, Eq. (46). Figures reprinted from Ref. [26] (published under CC BY 3.0 license).

of turbulent flows manifest in time-wise fluctuations of wind power generation. In a recent Letter [27], M.M. Bandi suggests that due to the long-ranging correlations in atmospheric turbulence, there exists a natural bound for geographic smoothing beyond which fluctuations do not further decrease among aggregation.

3.3 Power grids as network dynamical systems

We have seen that wind power shows specific non-Gaussian and correlated fluctuations on time scales as short as seconds. In this section, we want to derive the simplistic model for high-voltage alternating current (AC) grids that was introduced to the community of theoretical physics by Filatrella *et al.* [7] and captures the phase and frequency dynamics on such timescales. We remark that our main purpose is to derive a theoretical framework which allows us to understand the physical interaction of fluctuations with the power grid. We do not intend to perform an analysis or even make predictions for existing power grids. In the following, we briefly sketch the derivation of our network dynamical model [72–74]. For a more detailed discussion, we refer to the power system literature [72, 75, 76].

3.3.1 *Power flow equations*

Let us consider a power grid with $i = 1, \ldots, N$ nodes connected by lines with admittance y_{ij}. Given that in high-voltage grids, the three phases of the alternating current are usually symmetrically loaded, we only consider a single phase in our calculations [34]. To each node, we may assign a complex voltage

$$U_i = E_i e^{i\varphi_i} \tag{55}$$

with amplitude E_i and phase φ_i. Following Ohm's law, the current I_{ij} from node j to node i along line ij is

$$I_{ij} = y_{ij}(U_i - U_j). \tag{56}$$

We remark that the admittances y_{ij} can be interpreted as a weighted adjacency matrix in the sense of Eq. (1): y_{ij} takes some, generally complex, nonzero value if a line between nodes i and j exists. Otherwise, $y_{ij} = 0$. For the apparent power S_i^{inj} injected into node i, we find

$$S_i^{\text{inj}} = \sum_{j=1}^{N} U_i I_{ij}^* = U_i \sum_{j=1}^{N} y_{ij}^*(U_i^* - U_j^*) \tag{57}$$

Here, "$*$" refers to complex conjugation. In Eq. (57), we observe that the voltages U_i couple diffusively to the power injection at node i; in analogy to Eq. (18). We can therefore express the coupling in Eq. (57) in terms of the graph Laplacian matrix, Eq. (20), of the admittances y_{ij}. In analogy to Eq. (20), we define

$$Y_{ij} := \begin{cases} -y_{ij} & \text{if } i \neq j \\ \sum\limits_{k=1}^{N} y_{ik} & \text{if } i = j \end{cases} \tag{58}$$

which is referred to as the *nodal admittance matrix* [72, 74] and is by construction a graph Laplacian. Therewith we find

$$S_i^{\text{inj}} = U_i \left(U_i^* \sum_{j=1}^{N} y_{ij}^* - \sum_{j=1}^{N} y_{ij}^* U_j^* \right) \tag{59}$$

$$= U_i \sum_{j=1}^{N} Y_{ij}^* U_j^*. \tag{60}$$

We further define the conductance G_{ij} as the real and the susceptance B_{ij} as the imaginary part of the admittance matrix,

$$Y_{ij} = G_{ij} + iB_{ij}, \tag{61}$$

and write

$$S_i^{\mathrm{inj}} = U_i \sum_{j=1}^{N} \left(G_{ij} - iB_{ij}\right) U_j^* \tag{62}$$

$$= E_i e^{i\varphi_i} \sum_{j=1}^{N} \left(G_{ij} - iB_{ij}\right) E_j e^{-i\varphi_j} \tag{63}$$

$$= \sum_{j=1}^{N} E_i E_j \left(G_{ij} - iB_{ij}\right) e^{i(\varphi_i - \varphi_j)} \tag{64}$$

$$= \sum_{j=1}^{N} E_i E_j \left(G_{ij} - iB_{ij}\right) \left(\cos(\varphi_i - \varphi_j) + i\sin(\varphi_i - \varphi_j)\right). \tag{65}$$

Finally, we obtain for the active power P_i^{inj} injected to node i

$$P_i^{\mathrm{inj}} = \Re(S_i^{\mathrm{inj}})$$
$$= \sum_{j=1}^{N} E_i E_j \left(G_{ij}\cos(\varphi_i - \varphi_j) + B_{ij}\sin(\varphi_i - \varphi_j)\right). \tag{66}$$

Eq. (66) and the analogue expression for the reactive power, $Q_i^{\mathrm{inj}} = \Im(S_i^{\mathrm{inj}})$, are referred to as the *load flow equations* [72].

3.3.2 *Swing equation*

The dynamics of today's high-voltage AC power grids are governed by the rotating masses of synchronous generators in large conventional power plants. Synchronous generators consist of a rotor and a stator. The rotor is driven by a turbine and establishes a rotating magnetic field which induces alternating voltages and currents in the (usually three) stator windings. Mechanical rotor angle and electric phase angle are synchronous [74–76]. From a simplistic standpoint, such generators convert mechanical power P_i^{source} into electrical power P_i^{inj} injected into the grid and rotational energy of the rotating mass. Due to mechanical friction, some fraction of the power is lost in dissipation. An adequate power balance is hence given by

$$P_i^{\mathrm{source}} = \frac{d}{dt}\left(\frac{1}{2} J_i \dot{\varphi}_i^2\right) + \gamma_i \dot{\varphi}_i^2 + P_i^{\mathrm{inj}}, \tag{67}$$

where we introduced the moment of inertia J_i of the rotating mass and the damping constant γ_i [7, 30]. We approximate high-voltage AC transmission lines as purely inductive, that is

$$G_{ij} = 0. \tag{68}$$

In normal, unperturbed operation, the synchronous generator rotates at fixed frequency ω_0 and locked phase differences $\varphi_i^0 - \varphi_j^0 = \vartheta_i^0 - \vartheta_j^0$

to adjacent nodes j. Let us define the phase variation with respect to the phase-locked state as $\alpha_i(t) = \varphi_i(t) - \omega_0 t + \vartheta_i^0$. If the variations of $\alpha_i(t)$ are only small compared to the reference frequency, $\dot{\alpha}_i \ll \omega_0$, their dynamics are governed by

$$\ddot{\alpha}_i + 2\frac{\gamma_i}{J_i}\dot{\alpha}_i = \frac{P_i}{J_i\omega_0} - \sum_{j=1}^{N} \frac{E_i E_j B_{ij}}{J_i\omega_0} \sin(\varphi_i - \varphi_j), \tag{69}$$

that is the *swing equation* for synchronous generators, combined with the load flow Eq. (66) [7, 30]. P_i now stands for the effectively produced power at generator i. Throughout this thesis, we neglect voltage fluctuations of the synchronous machines and refer to [74] for a dynamical model which includes voltage fluctuations.

3.3.3 *The synchronous motor model*

In the previous section, we have derived a differential equation for the phase variations $\alpha_i(t)$ of synchronous generators. The *synchronous motor model*, which we use for our analyses, represents the loads in the grid as synchronous motors which function similar to synchronous generators only that electrical energy is converted to mechanical energy, that is $P_i < 0$. This load representation is not the only possible one. Other options are the *effective network* or the *structure-preserving* model [77]. In the former, loads are represented as constant impedances rather than oscillators. The latter models loads as first-order oscillators without inertia, that is $J_i = 0$ for all loads [77].

The synchronous motor model has the advantage that both, generators and motors/loads, follow Eq. (69). It is widely used among the literature (e.g. [7, 18, 30, 31]). We emphasize the close relation of the frequency synchronization and phase locking in this model with our earlier discussion on Kuramoto's model, Sec. 2.5.3.

For simplicity, we assume homogeneous machine parameters, $J_i \equiv J$ and $\gamma_i \equiv \gamma$. Further, we define the coupling matrix $K_{ij} := E_i E_j B_{ij}$. We can then model the dynamics at each node i as

$$\ddot{\alpha}_i + 2\frac{\gamma}{J}\dot{\alpha}_i = \frac{P_i}{J\omega_0} - \sum_{j=1}^{N} \frac{K_{ij}}{J\omega_0} \sin(\varphi_i - \varphi_j), \tag{70}$$

or, introducing the timescale $\tau = J/\gamma$,

$$\tau^2\ddot{\alpha}_i + 2\tau\dot{\alpha}_i = \frac{J}{\gamma^2\omega_0}P_i - \sum_{j=1}^{N} \frac{J}{\gamma^2\omega_0} K_{ij} \sin(\varphi_i - \varphi_j). \tag{71}$$

3.4 EXPERIMENTAL SETUP FOR GRID FREQUENCY MEASUREMENTS

In this thesis, we analyze the impact of fluctuating wind power injection on the grid frequency also in experimentally measured data. We measure time series of the voltage $U(t)$ after a toroidal transformer (Talema Ta60, 115V/115V to 7V/7V, 5VA each) which the electronic workshop of the University of Oldenburg constructed for us explicitly for that purpose (order numbers 176/16 and 131/17). The transformer allows us to sample the voltage with an NI cRIO-9014 real-time controller with an NI 9215 analogue input module.

We explain our data analysis techniques in the published papers which constitute the following chapters.

4 THE FOOTPRINT OF ATMOSPHERIC TURBULENCE IN POWER GRID FREQUENCY MEASUREMENTS

This chapter is, with minor editorial changes, identical to our publication

Haehne, H., Schottler, J., Waechter, M., Peinke, J., & Kamps, O. (2018). The footprint of atmospheric turbulence in power grid frequency measurements. *Europhysics Letters*, 121(3), 30001.

Reprint with permission from EPLA.

ABSTRACT

Fluctuating wind energy makes a stable grid operation challenging. Due to the direct contact with atmospheric turbulence, intermittent short-term variations in the wind speed are converted to power fluctuations that cause transient imbalances in the grid. We investigate the impact of wind energy feed-in on short-term fluctuations in the frequency of the public power grid, which we have measured in our local distribution grid. By conditioning on wind power production data, provided by the ENTSO-E transparency platform, we demonstrate that wind energy feed-in has a measurable effect on frequency increment statistics for short time scales (< 1 sec) that are below the activation time of frequency control. Our results are in accordance with previous numerical studies of self-organized synchronization in power grids under intermittent perturbation and give rise to new challenges for a stable operation of future power grids fed by a high share of renewable generation.

4.1 INTRODUCTION

Wind energy is one of the core elements of renewable power production with increasing feed-in to the central European power grid: In 2016, an installed capacity of 153.7 GW in the EU generated almost 300 TWh and covered 10.4% of the EU electricity demand [78]. In the first days of 2018, even more than 20% (60%) of the EU (German) daily electricity demand was covered [79].

A stable and reliable supply with electrical power is essential for both, society and economy. The power grid frequency reflects the transient ratio of production to demand in the grid and thus serves as an instantaneous and locally inferable stability parameter. Mismatch of production and consumption causes frequency deviations from the nominal frequency [75]. Load frequency control of the grid operator restores the frequency after perturbations: The fastest control ("primary control") sets in seconds after a deviation from the nominal frequency to stabilize, but not yet restore, the frequency. Restoration is achieved by secondary control which operates on time scales of 30 seconds and beyond [80].

Wind energy feed-in is known to be highly volatile. Fluctuations of a process $x(t)$ on a time scale τ are often characterized by means of increments $\Delta_\tau x := x(t) - x(t+\tau)$[1]. Traditional analysis and prediction of wind speed considers variations in 15 minutes and longer [26, 81]. However, recent findings in the analysis of short-term increments of renewable power generation reveal strongly non-Gaussian fluctuations even on scales of one second [25, 26]. But, where does this short-term behavior result from?

The atmospheric boundary layer is known to be non-stationary and turbulent [82–84]. Turbulent flows show scale-dependent increment statistics: In an hierarchical cascade process, kinetic energy is transferred from large- to small-scale structures [69]. Specifically, this implies pronounced tails in short-term increment statistics; an effect termed *intermittency* in turbulence research [28]. Due to the intermittent increment statistics, severe wind-speed fluctuations are much more likely than expected from a normal distribution.

A wind turbine transforms the kinetic energy of the wind to electric power. Even though *ac-dc-ac* converters decouple wind speed from power output dynamics, turbine controllers maximize the power output and follow wind speed variations [25]. Hence, atmospheric fluctuations even within a second propagate into the power output of wind farms and are fed to the grid. In fact, intermittency is found in production time series of wind (and also photovoltaic) power plants [25, 26]. Consequently, power quality is a major challenge for the grid integration of renewable generators [85].

The transient short-term reaction of power grids to perturbations has attracted great attention in theoretical physics: Simple models of high-voltage ac-grids correspond to complex networks of Kuramoto-like, phase-coupled oscillators [7, 74]. Such models have been used to analyze aspects of synchronization [18] and the interplay of stability and topology [21], as well as relaxation after singular [30] and stochastic [31, 32] perturbations. The impact of intermittent feed-in on power grids has been addressed in [32, 33]: Numerical results indicate that intermittency propagates in a power grid and affects the frequency increment distributions of nodes distant to the feed-in. Stochastic models for non-Gaussian frequency fluctuations are pre-

1 We remark that, unfortunately, we used a definition of the increment in this paper which deviates from the convention $\Delta_\tau x := x(t+\tau) - x(t)$ we use throughout the rest of this thesis. This does not impact the results. (Additional comment not from the paper).

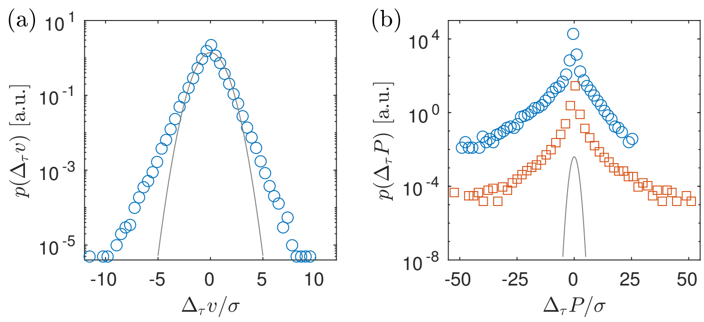

Figure 7: **Atmospheric intermittency is preserved in power time series of a single wind turbine and also in the average output of a farm of twelve turbines.** *(a)* Distribution of wind speed increments $\Delta_\tau v = v(t) - v(t+\tau)$ for $\tau = 1$ sec. Due to the turbulent conditions in the atmosphere, the increment distribution shows large deviations from the normal distribution (gray). *(b)* Distribution of power increments $\Delta_\tau P$ for $\tau = 1$ sec of a single turbine (blue) and of the average power of twelve turbines (orange). The deviations from the normal distribution are even more pronounced than for the wind speed increments and do not average out. The increment PDF for the single turbine is not symmetric which, to our interpretation, results from operations close to the rated power $P_r \approx 2$ MW. All increments are given in units of their respective standard deviations; these are $\sigma(\Delta_\tau v) = 0.29$ m/s, $\sigma(\Delta_\tau P) = 0.0067$ MW for the single turbine, and $\sigma(\Delta_\tau P) = 0.0292$ MW for the average of twelve turbines. PDFs are vertically shifted for convenience of presentation. Figures are similar to those in [26] and were produced from a freely available [89] data set of 1 Hz-recordings of twelve onshore turbines during one month; kindly provided by WPD Windmanager GmbH, Bremen, Germany. A detailed stochastic analysis can be found in [25] and [26].

sented in [86]. However, none of the prior results relates the intermittent feed-in to transient stochastic properties of the grid frequency.

It is often believed that intermittency vanishes when power time series of many turbines are averaged. To support this hypothesis, usually the central limit theorem is referred to. Velocity time series $v(t)$ are, however, highly correlated [87] and so are the resulting power time series [26]. The lacking statistical independence makes this theorem inapplicable. Intermittency is, in fact, observed in power outputs of entire wind farms [26] and withstands even country-wide averaging [88]. We show, as an example, the increment distribution for the mean power output of twelve turbines in comparison to the one of a single turbine in Fig. 7. But, what exactly is the impact of wind power feed-in on the grid frequency?

In this Letter, we complement the previous numeric and analytic work and show that the feed-in of intermittent wind power has a measurable effect on the increment statistics of the frequency measured in the distribution grid. Instead of focusing on the frequency response to singular, large-deviation events, as for example in [90], we use the full statistical information encoded in the increment statistics of the grid frequency and focus on time scales that lie below the activation of primary control.

This paper continues as follows: We first introduce our measurement and data processing techniques. Subsequently, we show our stochastic analysis and its interpretation. Finally, we conclude and give an outlook on further research.

4.2 METHODS

Publicly available measurements of the frequency of the public power grid have, to our knowledge, only a time resolution of 1 second or above. We, however, want to observe the self-organized, transient behavior of the grid and thus need a higher time resolution.

We took 10 kHz voltage samplings $u(t)$ of a single phase of the distribution grid in our lab in Oldenburg, northern Germany, from November 8, 2016, till March 23, 2017 (see also Sec. 3.4). Subsequently, we applied the method of *Instantaneous Frequency* (IF) [91] to estimate the frequency time series $f(t)$ from the sinusoidal voltage signal $u(t)$.

The IF reveals the dominant frequency component at each time instant t and is thus suited for signals composed of one major frequency component. The method makes use of the fact that real-valued signals, such as the voltage signal $u(t)$, have conjugate symmetric Fourier representations, $\mathcal{F}[u](-\omega) = \mathcal{F}[u](\omega)^*$. Here, $\mathcal{F}$ denotes Fourier transform. The complex-valued analytic signal $z(t)$ is the inverse Fourier transform of the positive frequencies $\omega > 0$. Discarding the redundant negative frequency components makes the IF accessible. It is defined as the time derivative of the phase $\Phi(t)$ of the analytic signal $z(t)$:

$$f(t) = \frac{1}{2\pi}\frac{d}{dt}\Phi(t) = \frac{1}{2\pi}\frac{d}{dt}\arg(z(t)). \tag{72}$$

In practice, $z(t)$ is obtained from the Hilbert transform $\mathcal{H}[u](t)$ of the original signal: $z(t) := u(t) + i\mathcal{H}[u](t)$. The Hilbert transform can be obtained from $\mathcal{H}[u](t) = (u * 1/\pi t')(t)$, where "$*$" denotes convolution.

To estimate the derivative in Eq. (72) numerically, the phase $\Phi(t)$ was calculated for every time step in the voltage signal. Subsequently, the time derivative was estimated by linear fits of $\Phi(t)$ in disjoint blocks of 2000 samples. This procedure gives a frequency time series $f(t)$ with a time resolution of 200 ms. The 2σ-confidence bounds of the linear fits are, in average, of size $\pm$ 1 mHz. We show one example hour from our measurements in Fig. 8.

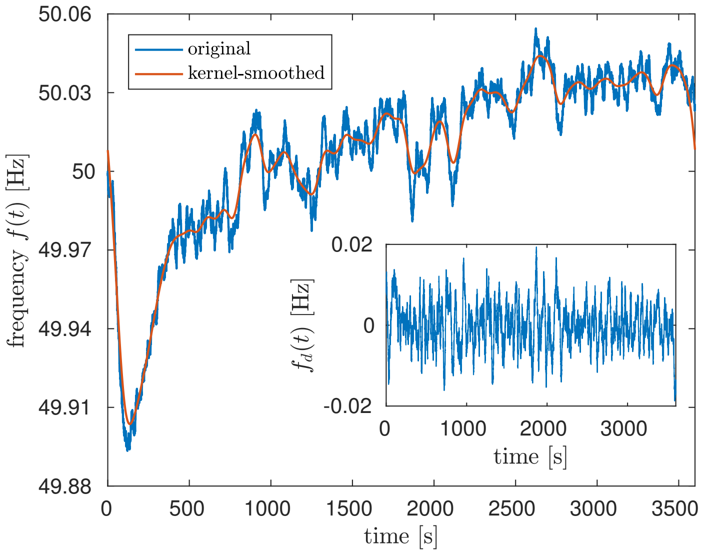

Figure 8: **Detrending isolates the short-term behavior of the signal.** Original frequency signal $f(t)$ (blue) and kernel-smoothed signal $f_{ks}(t)$ (orange) in one example hour. The kernel standard deviation is $\sigma = 30$ s. *Inset*: Detrended signal $f_d(t)$.

Frequency measurements of the public power grid are influenced by many factors that overlay the influence of renewable generation. The signal shows severe deviations from the nominal frequency each full and half hour caused by power trading. Further, it is influenced by long-term correlations in demand and production. Thus, we applied *kernel detrending* to isolate the short-term behavior of the frequency signal $f(t)$: A kernel-smoothed signal $f_{ks}(t)$ was subtracted from the original signal to obtain the detrended signal $f_d(t) = f(t) - f_{ks}(t)$. We used a 30-seconds Gaussian kernel. The kernel-smoothed signal is obtained from convolving the original signal with a Gaussian curve $g_\sigma(t)$ with standard deviation $\sigma = 30$ s and zero mean:

$$f_d(t) = f(t) - f_{ks}(t) = f(t) - (f * g_\sigma)(t). \tag{73}$$

Again, "$*$" denotes convolution. We illustrate the detrending in Fig. 8. In the following, we use the detrended data and drop the index d.

4.3 RESULTS

To evaluate the fluctuations of the grid frequency we focus on probability density functions (PDFs) of increments, $p(\Delta_\tau f)$. As shown in Fig. 9 a, the increment distribution $p(\Delta_\tau f)$ is, for a time scale of $\tau = 200$ ms, not Gaussian. Its tails cause strong deviations from the normal distribution. This means that large increments occur much more frequently than expected from a normal distribution.

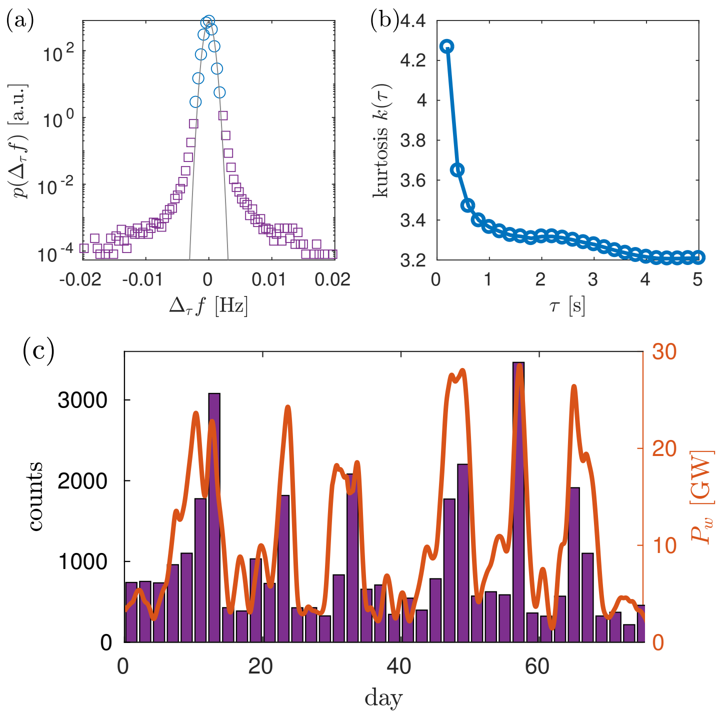

Figure 9: **Large short-term increments accumulate on days with a high share of wind power fed to the grid.** *(a)* Frequency increment distribution $p(\Delta_\tau f)$ for $\tau = 200$ ms. Tails (violet squares) deviate from the normal distribution (gray). *(b)* Kurtosis $k(\tau)$ of $p(\Delta_\tau f)$ as a function of the time lag τ. While for a Gaussian distribution $k = 3$, larger kurtosis values correspond to heavier tails. $p(\Delta_\tau f)$ has the highest kurtosis on time scales below one second. *(c)* Left axis and violet boxes: Histogram of occurrences of large increments $|\Delta_\tau f| > 2$ mHz ($\tau = 200$ ms) binned for two days for the first 70 days of our measurement. Right axis and orange curve: Amount of onshore wind power fed to the grid in Germany. Production data are taken from [92] and smoothed with moving average of two days.

The kurtosis $k(\tau) = \langle(\Delta_\tau f - \langle\Delta_\tau f\rangle)^4\rangle/\sigma^4$ measures how heavy-tailed a distribution is. Here, σ denotes the standard deviation of $p(\Delta_\tau f)$. The kurtosis takes the value $k = 3$ for a Gaussian distribution and increases for more heavy-tailed shapes. We observe that the increment PDFs $p(\Delta_\tau f)$ deform to less heavy-tailed shapes for increasing time lags τ (Fig. 9 b). On time scales below one second, we find the most extreme tails. Even though this effect is similar to turbulent intermittency, can we – at all – relate such short-term fluctuations to wind power injection?

The grid frequency measurements are, obviously, influenced by many possibly non-Gaussian and/or correlated processes. To investigate a possible dependence of grid fluctuations on wind energy injection, we extract statistical properties of the detrended frequency signal $f(t)$ which we condition on the amount of onshore wind energy $P_w(t)$ that is fed to the European grid in Germany. We use time series provided by the ENTSO-E Transparency Platform [92], specifically the dataset "actual generation per production type" for Germany and production type "onshore wind". This data set has a time resolution of 15 minutes. Hence, it does not allow for an analysis of the short-term behavior of the feed-in but still enables us to condition our high-frequency measurements on the amount of wind power fed to the grid. We focus on the generation in Germany because, first, it had, in 2016, by far the highest installed capacity of wind power [78] and, second, the provided data of other countries have an even lower time resolution.

We begin with a visual comparison of the increments $\Delta_\tau f$ and P_w: In Fig. 9 c, we show the time instants at which large increments occur as well as the amount of wind power P_w fed to the grid in Germany. We consider, for the moment, data aggregated for two days. Large increments $\Delta_\tau f$ coincide with high values of P_w. This is a first indication that wind power feed-in affects grid frequency fluctuations. In the following, we will provide a detailed analysis of the impact of wind power feed-in on frequency increment distributions on different time scales.

Instationary stochastic processes are known to potentially produce heavy tails in their probability distributions (e.g. [93]). Wind turbulence, in particular, shows characteristic turbulent behavior only when wind speed increments are conditioned on the absolute wind speed [94]. Motivated by such findings, we pinpoint the impact of wind power injection on the grid frequency by the analysis of conditioned increment PDFs $p(\Delta_\tau f|P_w)$. Thus, we learn how likely an increment $\Delta_\tau f$ is if an amount P_w of wind energy is fed to the grid. We show this PDF for a short ($\tau = 200$ ms) and a long ($\tau = 10$ s) time scale for different ranges of P_w in Figs. 10 a & b. First, we observe that on the short scale, the tails deviate from the normal distribution (gray reference curve), whereas the increment PDF is very close to normal on the long scale. Second, for the long time scale, the PDFs are almost identical, irrespectively of P_w. On the short time scale, however, we observe a broadening of the distribution with increasing P_w.

We quantify the time scale dependent impact of the feed-in P_w on the increment PDF by means of width and shape of the conditioned PDFs. In Fig. 10 c, we show that the variance

$$\sigma^2(\tau, P_w) := \int (\Delta_\tau f - \langle \Delta_\tau f \rangle_{P_w})^2 p(\Delta_\tau f|P_w) d\Delta_\tau f \tag{74}$$

of the conditioned increment PDF increases with P_w for $\tau = 200$ ms. For increasing time lags τ, this effect quickly diminishes. On time scales of $\tau = 800$ ms and above, the variances show no clear trend with P_w.

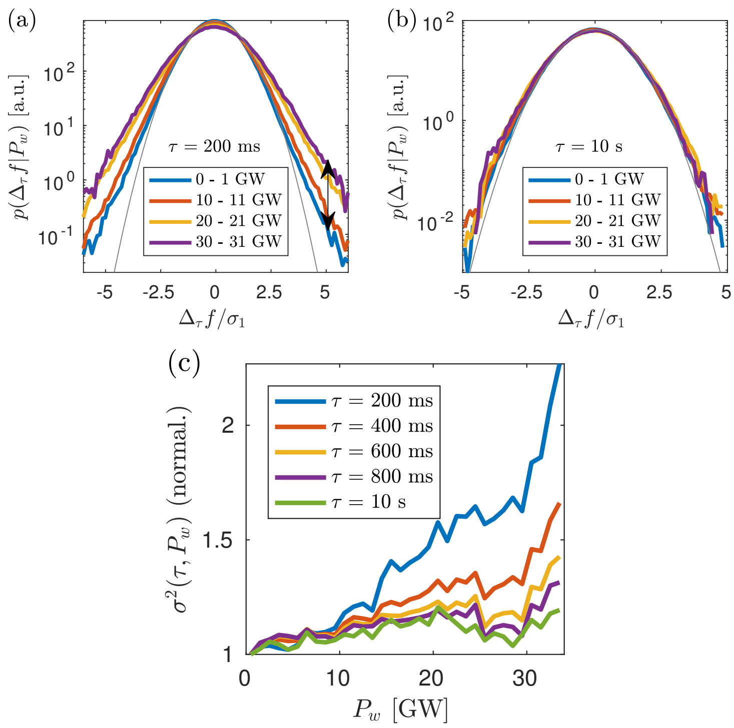

Figure 10: **Wind energy feed-in affects the short-term statistics of the power grid frequency.** *(a)* PDF of increments $\Delta_\tau f$ on the time scale $\tau = 200$ ms for different intervals of P_w (color-coded) normalized by the standard deviation σ_1 of the smallest P_w interval. Increasing feed-in P_w broadens the increment distribution resulting in a tenfold higher probability for a $5\sigma_1$-event (black arrow). *(b)* Increment PDF for a larger time scale, $\tau = 10$ s. The increments follow the same, almost Gaussian, distribution; independent of the amount of wind energy P_w fed to the grid. *(c)* Variances of increment distributions plotted against P_w for different time scales (color-coded). On the shortest time scale, $\tau = 200$ ms, the distribution becomes broader with increasing P_w. This effect diminishes with increasing time lags τ. On the longest scale, $\tau = 10$ s, the variance shows no clear trend with P_w. For all time scales, the variances were normalized with the respective smallest P_w bin.

An increased probability of large fluctuations may result not only from an increased variance but also from non-Gaussian, heavy-tailed shapes of the PDFs. To quantify the shape development of $p(\Delta_\tau f|P_w)$ with P_w, we use a model which was proposed by Castaing for the characterization of intermittency in turbulence [95].

Castaing uses superimposed Gaussian PDFs with log-normally distributed variances to grasp the tails in intermittent increment PDFs. The standard deviation λ^2 of the log-normal distribution,

$$\lambda^2 = \frac{1}{4}\ln\left(\frac{\langle(\Delta_\tau f - \langle\Delta_\tau f\rangle)^4\rangle}{3\cdot\langle(\Delta_\tau f - \langle\Delta_\tau f\rangle)^2\rangle^2}\right) = \frac{1}{4}\ln\left(\frac{k(\tau)}{3}\right), \tag{75}$$

governs the shape of the thus obtained PDF $p_c(\Delta_\tau f|P_w)$ and is called *shape parameter* [96]. Due to its close relation to the kurtosis $k(\tau)$, it serves as a measure for the heavy-taildness of the Castaing PDF: For a Gaussian PDF, λ^2 is zero. It increases the larger the deviations of the tails from the Gaussian PDF become. In wind speed measurements, we find λ^2 in the range of 0.2 – 0.3 for increment PDFs on short time scales [94].

We calculate λ^2 from our measurements with Eq. (75) and follow the steps in [94] to obtain the explicit expression of $p_c(\Delta_\tau f|P_w)$. The results match the data very well as shown in Fig. 11 a, where we compare the conditioned increment PDFs for a small and a large P_w on the short scale ($\tau = 200$ ms). With this result we are now able to analyze the change in shape as a function of the wind power P_w, see Fig. 11 b. In accordance with Figs. 10 a and b, we observe lower λ^2-values for $\tau = 10$ s than for $\tau = 200$ ms; i.e. the PDFs are closer to the Gaussian distribution on the longer time scale. In contrast to the variance (Fig. 10 c), we do not observe a clear trend of λ^2 with P_w. This means that wind energy feed-in mainly broadens the conditioned increment PDF on short scales without much affecting its shape.

The Castaing parametrizations $p_c(\Delta_\tau f|P_w)$ can be used to estimate the impact of P_w on extreme fluctuations of the frequency: In Fig. 11 a, we compare the probability of a 5σ-event during high wind energy feed-in P_w to a Gaussian model. We observe a factor 900 between the Castaing model and the Gaussian (black arrow in Fig. 11 a). Note that this probability factor increases further by many orders of magnitude for larger σ-events which for the Gaussian statistics are expected to almost never occur – even though we observe them already in our relatively short data set. This stresses the importance of a correct non-Gaussian modeling of frequency fluctuations in power grids with intermittent feed-in.

4.4 CONCLUSIONS AND DISCUSSION

We have shown that wind power feed-in impacts the power grid frequency on time scales that lie below one second. The time range up

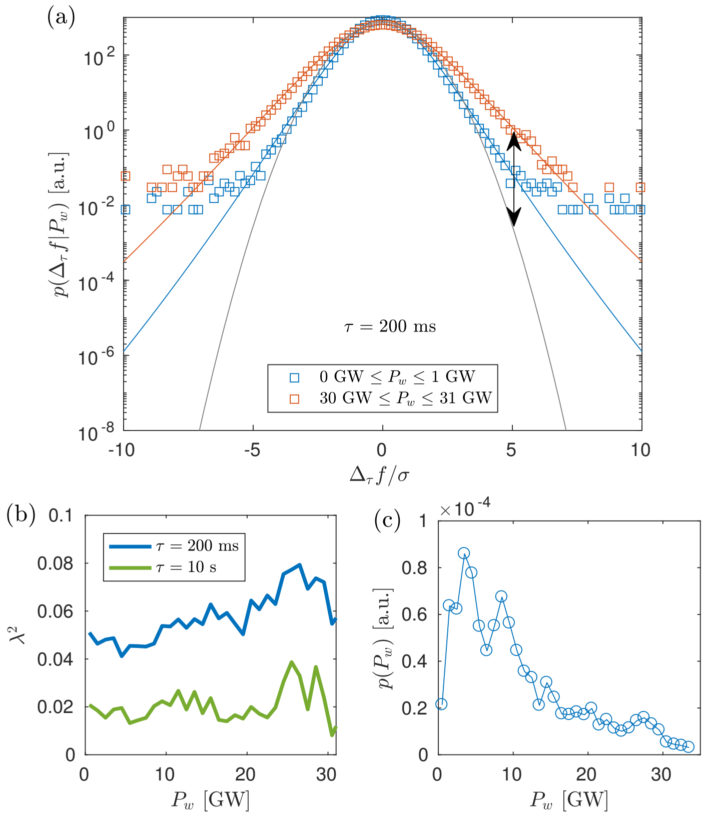

Figure 11: **Castaing curves grasp the tails of conditioned increment PDFs.** *(a)* Conditioned PDFs $p(\Delta_\tau f|P_w)$ for $\tau = 200$ ms estimated from measurements (squares) and Castaing curves $p_c(\Delta_\tau f|P_w)$ (straight lines) using the shape parameter λ^2 (Eq. (75)) for a low (blue) and a high (orange) amount of wind energy feed-in P_w. Both PDFs are normalized with the standard deviation $\sigma = 0.53$ mHz of the (unconditioned) PDF $p(\Delta_\tau f)$. The Castaing curves emphasize the importance of a correct modeling of the increment PDFs: Within this model, the probability of a 5σ event is increased by a factor 900 as compared to a Gaussian model (black arrow). *(b)* Shape parameter λ^2 used to derive $p_c(\Delta_\tau f|P_w)$ for $\tau = 200$ ms plotted against P_w. For comparison, we have included the evolution of λ^2 also for $\tau = 10$ s. The shape parameter shows no clear trend with P_w. *(c)* PDF of the wind energy feed-in $p(P_w)$ during our measurements (data available in [92]).

to approximately one second is interesting in two aspects: First, it lies in the range of activation of primary frequency control [80]. This suggests that fluctuations by wind power injection on longer time scales are successfully compensated. Second, in the context of *Small Signal Stability Analysis*, one second is approximately the time scale that separates local modes, which affect only a localized subset of nodes in the grid, from so-called interarea modes [97]. This suggests that the effect we measure is local; a result which is in accordance with our analysis in so far as the used German wind power data are dominated by the northern region of Germany where our frequency measurements were made.

Power quality is a key challenge for the grid integration of renewable generators [85]. Although the absolute size of the fluctuations we consider is small ($\Delta_\tau f < 20$ mHz for $\tau = 200$ ms), a precise knowledge of the fluctuation statistics is essential to correctly estimate the probability of large, possibly critical, increments. In future power grids with a high share of renewable energy sources, the amount of rotational inertia will be much lower than today. This will lead to faster frequency dynamics with larger amplitudes [98]. If grid design and control strategies are not properly adapted, such frequency fluctuations may become highly critical for the grid stability [31]. Thus, an explicit expression for increment probabilities is desirable to correctly quantify these risks.

Our analysis offers a new tool to quantify the impact of renewable generation on the frequency increment statistics: The conditioned increment PDFs $p(\Delta_\tau f|P_w)$ are well described by Castaing's parametrization. For a given distribution of the feed-in $p(P_w)$ (Fig. 11 c), the conditioned PDFs may be assumed to follow $p_c(\Delta_\tau f|P_w)$ with, in the simplest model, constant shape parameter (Fig. 11 b) and variance increasing with P_w (Fig. 10 c). If shape parameter and variance evolution are inferred from calibration measurements, the increment PDF

$$p(\Delta_\tau f) = \int p(P_w) p_c(\Delta_\tau f|P_w) dP_w \tag{76}$$

describes the overall impact of wind energy feed-in on the fluctuation characteristics of a given grid and may be helpful for the design of new control strategies for grids with a high share of renewable sources.

We want to point out that the non-Gaussian increment statistics $p(\Delta_\tau f)$ may also be fitted with other heavy-tailed distributions, such as q-Gaussians or α-stable distributions, which have successfully been applied to single-point PDFs of grid frequency data [86] as well as to other complex systems like stock markets [99] or biological systems [100]. An important property of such distributions is, besides the stability, the fact that they have diverging moments for wide parameter ranges. We use here the turbulence-like finite-moment approach because, first, we see that power fluctuations are driven by wind turbulence and, second, we observe that frequency increment PDFs are not stable: The sum of two consecutive increments is per definition an increment of a larger scale. However, with increasing time lag, the kurtosis of the increment PDF decreases (Fig. 9 b). Hence, the hypothesis of stability is violated.

Independently of the question about the best model of the increment statistics, our main finding is that we observe a broadening of frequency increment PDFs with increasing share of wind power generation. There remains an open question, i.e., to what extend the shape of the increment PDFs is caused by the turbulent wind statistics [2] or by other collective effects of interacting grid components. We conclude that a deep understanding of the non-Gaussian fluctuations of renewable energy sources and their interaction with the grid is an important field of further research.

2 In principle, we expect also photovoltaic feed-in to cause similar frequency fluctuations. However, we leave this as a question for further research because, first, during our winter time measurements only small amounts of PV energy were generated and, second, intermittency in PV power time series depends not only on the amount of produced energy but also on cloud structures. Hence, a similar analysis for PV requires additional data sets.

5 PROPAGATION OF WIND-POWER-INDUCED FLUCTUATIONS IN POWER GRIDS

This chapter (including the Supplemental Material) is, with minor editorial changes, identical to our publication

Haehne, H., Schmietendorf, K., Tamrakar, S.R., Peinke, J., & Kettemann, S. (2019) Propagation of Wind-Power-Induced Fluctuations in Power Grids. *Physical Review E*, 99, 050301(R).

ABSTRACT

Renewable generators perturb the electric power grid with heavily non-Gaussian and time correlated fluctuations. While changes in generated power on timescales of minutes and hours are compensated by frequency control measures, we report subsecond distribution grid frequency measurements with local non-Gaussian fluctuations which depend on the magnitude of wind power generation in the grid. Motivated by such experimental findings, we simulate the sub-second grid frequency dynamics by perturbing the power grid, as modeled by a network of phase coupled nonlinear oscillators, with synthetically generated wind power feed-in time series. We derive a linear response theory and obtain analytical results for the variance of frequency increment distributions. We find that the variance of short-term fluctuations decays, for large inertia, exponentially with distance to the feed-in node, in agreement with numerical results both for a linear chain of nodes and the German transmission grid topology. In sharp contrast, the kurtosis of frequency increments is numerically found to decay only slowly, not exponentially, in both systems, indicating that the non-Gaussian shape of frequency fluctuations persists over long ranges.

5.1 INTRODUCTION

For the transition of electric energy supply towards renewable sources, wind power plays a crucial role. Alone in 2017, 15.6 GW of new wind power capacity was installed in the European Union (EU), now summing up to 168.7 GW, that is 18% of the total installed power generation capacity in the EU [101].

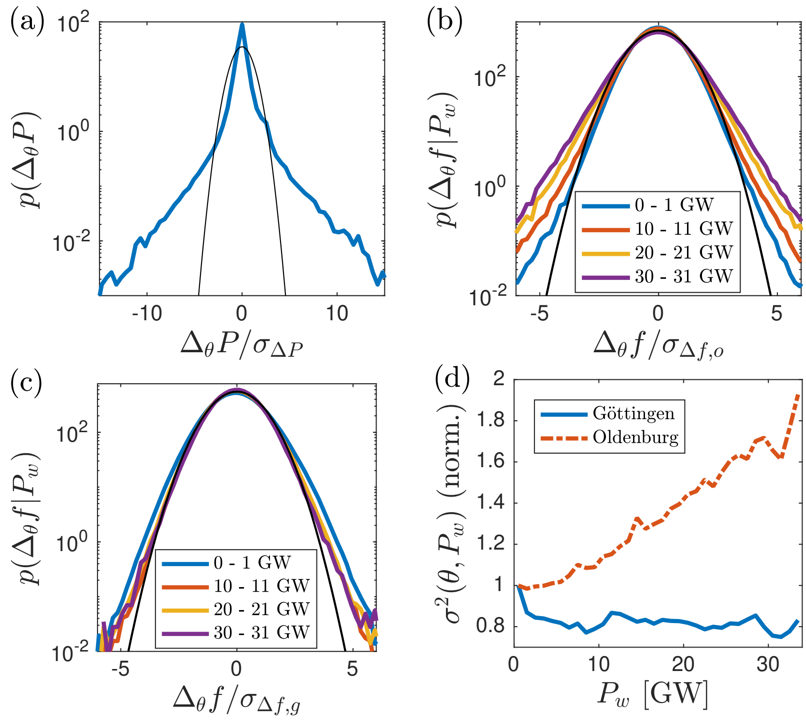

Figure 12: *(a)* Distribution of power increments $\Delta_\theta P = P(t+\theta) - P(t)$ of the aggregated output $P(t)$ of 12 wind turbines in a wind park (timescale $\theta = 1$ s) [89] and Gaussian distribution as a reference in black. Each turbine has a rated power $P_r \approx 2$ MW. Power increments are given in units of the standard deviation $\sigma_{\Delta P} = 0.023$ MW of $p(\Delta_\theta P)$. *(b)* Frequency increment distribution $p(\Delta_\theta f|P_w)$ conditioned on wind energy generation P_w in Germany, measured in Oldenburg ($\theta = 0.2$ s). $p(\Delta_\theta f|P_w)$ broadens with increasing P_w. *(c)* Simultaneously measured data in Göttingen. Standard deviations of $p(\Delta_\theta f)$ are $\sigma_{\Delta f,o} = 0.58$ mHz in Oldenburg and $\sigma_{\Delta f,g} = 0.73$ mHz in Göttingen. *(d)* Variance evolution of the distributions in (b) and (c) with P_w, normalized with the first P_w-bin.[1]

In contrast to the steady production of conventional power sources, wind power generation is highly volatile. Due to its continuing and increasing integration to the European power grid, maintaining a high power quality despite such fluctuations has become an important task [85]. For the analysis of fluctuations on a timescale θ of a stochastic process $x(t)$, we study the statistics of increments $\Delta_\theta x(t) = x(t+\theta) - x(t)$ as quantified by their moments $\langle(\Delta_\theta x - \langle\Delta_\theta x\rangle)^n\rangle$ which contain information about time correlations. Time series of wind power generation $P(t)$ show non-Gaussian increment probability density functions (PDFs) $p(\Delta_\theta P)$ on timescales of few seconds [25, 26]. The tails

1 We obtain different values for the standard deviation $\sigma_{\Delta P}$ of the increments of the aggregated power output than in our earlier publication, Fig. 7, because we applied another treatment of missing values in the data set. Earlier (Fig. 7) we treated missing values of single turbines as zeros which causes an increased volatility in the

of such PDFs deviate from the Gaussian distribution even after aggregation of several turbines in a wind farm, Fig. 12 a, and are related to the turbulent nature of wind speed fluctuations [25].

On larger timescales, frequency control measures compensate feed-in fluctuations of renewable generators– thereby maintaining stable grid operation [80]. However, how does the grid respond to the characteristic non-Gaussian short-term fluctuations when its dynamics is governed by the inertia of rotating masses? How does that affect power quality? Recent results from local distribution grid frequency measurements show that on timescales below 1 s, grid frequency fluctuations actually increase with increasing wind power production [102]. Further, the timescale separating local from interarea modes in *Small Signal Stability Analysis* lies in the order of 1 s [97]. The question arises if such wind-power-induced fluctuations are a local feature resulting from high wind power injection close to the measurement or if they rather have a long-range effect to the grid.

Dynamical systems driven by non-Gaussian, turbulence-like noise model a broad range of natural and manmade phenomena [103]. Up to a few seconds, the dynamics of high-voltage AC-grids are captured by networks of inert phase-coupled oscillators [7, 75, 76]. For such models, the spreading of singular [30, 34], harmonic [104], and stochastic [36] perturbations were analyzed and evaluated. Modified Fokker-Planck equations have shown to be useful to predict steady state frequency distributions obtained from measurements in highly meshed grids [86]. Further, the probability of outages caused by fluctuating perturbations was evaluated in Refs. [31, 32]. While these results indicate that locally induced perturbations affect the dynamics and synchronization of coupled oscillators, it is not yet understood if stochastic perturbations affect the grid only locally or if they rather propagate throughout the grid and how that depends on the parameters and intrinsic timescales of the power grid.

Our work combines experimental and theoretical analyses of short-term increments $\Delta_\theta f = f(t+\theta) - f(t)$ of the grid frequency $f(t)$ which allows us to analyze fluctuations on timescales θ. We present grid frequency measurements at two different locations in Germany: Oldenburg, in the northwestern region of Germany with a high share of wind energy injection close to the measurement, and, in 213 km straight line distance towards the center of Germany, Göttingen, with smaller proportion of wind energy injection [105]. We show that the statistics of the fluctuations depends qualitatively differently on wind power feed-in at the two measurement positions. Motivated by these observations, we study the propagation of fluctuations in power grids by performing numerical simulations of the subsecond grid frequency dynamics, as modeled by a network of phase-coupled nonlinear oscil-

aggregated output. As we use this data set only for motivation purposes, this effect has no impact on our results (Additional comment not from the paper).

lators, and derive a linear response theory to obtain analytical results for the variance of frequency increment distributions as a function of the increment timescale, the distance from the feed-in node, and the system parameters, most importantly, the inertia in the grid.

5.2 DATA ANALYSIS

We use 10 kHz voltage samplings simultaneously measured in Oldenburg and Göttingen from 25 July 2017 until 13 March 2018, to derive a grid frequency time series $f(t)$ with a time resolution of 5 Hz. We provide details on our measurement techniques in the Supplemental Material (Sec. 5.8).

We characterize the short-term frequency fluctuations in terms of width (variance) and shape (kurtosis) of their increment PDFs. We use publicly available power generation data [92] to obtain conditioned PDFs $p(\Delta_\theta f|P_w)$. In an earlier measurement period ([102], Chapter 4), we have observed that $p(\Delta_\theta f)$ with $\theta = 0.2$ s broadens with an increased amount of wind energy P_w fed to the grid in Germany. In our new data set, we were able to reproduce our earlier results in Oldenburg, Fig. 12 b, while in the parallel Göttingen measurements, we see no such effect, Fig. 12 c. For comparison, we show the evolution of the conditioned variance $\sigma^2(\theta, P_w) := \mathrm{var}(p(\Delta_\theta f|P_w))$ with P_w (Fig. 12 d) clearly confirming the different short-term response to wind power feed-in at the two measurement spots.

Both short-term increment PDFs $p(\Delta_\theta f)$, $\theta = 0.2$ s, show non-Gaussian tails, characterized by a kurtosis $k > 3$, where

$$k = \frac{\langle(\Delta_\theta f - \langle\Delta_\theta f\rangle)^4\rangle}{\langle(\Delta_\theta f - \langle\Delta_\theta f\rangle)^2\rangle^2}. \tag{77}$$

We observe a higher kurtosis of $p(\Delta_\theta f)$ in Oldenburg ($k = 4.1$) than in Göttingen ($k = 3.4$). However, k shows no clear trend with P_w (not shown here).

In summary, we find that the impact of wind power generation on the short-term frequency fluctuations which is present in Oldenburg cannot be seen in Göttingen. Further, the PDFs $p(\Delta_\theta f)$ are slightly more heavy-tailed in Oldenburg than in Göttingen. To explore how the width and shape of $p(\Delta_\theta f)$ evolve with distance to the volatile feed-in, we now consider a simple power grid model driven by a stochastic signal and derive an analytic expression for the variance of the increment statistics from linear response theory.

5.3 POWER GRID MODELING

We consider the Synchronous Motor Model [7] for high-voltage AC grids. The phase angle $\vartheta_i(t)$ is, in this model, governed by the *Swing Equation*,

$$\tau^2\ddot{\alpha}_i + 2\tau\dot{\alpha}_i = \frac{J}{\gamma^2\omega_0}P_i - \sum_{j=1}^{N}\frac{J}{\gamma^2\omega_0}K_{ij}\sin(\vartheta_i^0 - \vartheta_j^0 + \alpha_i - \alpha_j). \tag{78}$$

where $\alpha_i(t) = \vartheta_i(t) - \vartheta_i^0$ is the deviation of $\vartheta_i(t)$ from the fixed point ϑ_i^0 on a co-moving reference frame. P_i denotes the generated or consumed power at node i. Further, $K_{ij} = K \cdot A_{ij}$, where A_{ij} denotes the adjacency matrix. In the following we fix the damping $\gamma = 10^5$ kgm^2/s and line capacity $K = 0.5\,\mathrm{GW}$. The reference frequency is $\omega_0 = 2\pi \cdot 50\,\mathrm{Hz}$ and the internal timescale τ follows from $\tau = J/\gamma$. We use homogeneous parameters. For a derivation of Eq. (78), we refer to Sec. 3.3.

Let us now consider the case in which a subset of nodes $\{j\}$ is driven by a noisy signal $P_j(t)$. The production or consumption at one of the perturbed nodes j decomposes as $P_j(t) = P_j^0 + \delta P_j(t)$ into a constant value P_j^0 corresponding to the fixed point and a stochastic perturbation $\delta P_j(t)$ with $\langle \delta P_j(t)\rangle = 0$.

If the system stays close to its fixed point of operation, $|\alpha_i| \ll 1$ [2], we may calculate the response of phase $\alpha_i(t)$ to the signal $\delta\Pi_j(t) := J/(\gamma^2\omega_0)\delta P_j(t)$ in first-order approximation as

$$\alpha_i(t) = \int_{-\infty}^{t}\frac{dt'}{\tau}\sum_j \delta\Pi_j(t')G_{ij}(t'-t) \tag{79}$$

where the propagator is defined by

$$G_{ij}(t'-t) = \sum_{n=0}^{N-1}\sum_{\sigma=\pm1}\frac{\phi_{ni}\phi_{nj}^*}{2\sqrt{1-\Lambda_n}}(-\sigma)e^{(1+\sigma\sqrt{1-\Lambda_n})\frac{t'-t}{\tau}}, \tag{80}$$

see Eqs. (93)-(102) in the Supplemental Material (Sec. 5.8) for the derivation. Here, $\Lambda_n \in \mathbb{R}$ are eigenvalues and $\boldsymbol{\phi}_n \in \mathbb{R}^N$ the corresponding eigenvectors of the generalized graph Laplacian matrix Λ with $\Lambda_{ij} = -\frac{J}{\gamma^2\omega_0}K_{ij}\cos(\vartheta_i^0 - \vartheta_j^0)$ and $\Lambda_{ii} = \frac{J}{\gamma^2\omega_0}\sum_j K_{ij}\cos(\vartheta_i^0 - \vartheta_j^0)$ which is related to the stability matrix used in small signal stability analysis [72, 97], see also Sec. 2.5. In contrast to prior results [33, 34, 36], our expression applies to any stochastic signal $\delta\Pi_j(t)$ and

2 See Eq. (S2) in the Supplement of [34] for a more accurate condition for the validity of linear response.

does not rely on a pure analysis of power spectra. An expression similar to Eq. (79) has been deduced in Ref. [106] independently from our work.

For simplicity, we now focus on the case where the system (78) is driven at a single node j. With the help of Eq. (79), we derive an expression for the variance of the frequency increment PDF on timescale θ, which only depends on the auto-correlation function of the increment time series $\mathrm{acf}(|\delta|) = \langle \Delta_\theta \Pi_j(t) \Delta_\theta \Pi_j(t+\delta) \rangle$,

$$\langle \Delta_\theta \omega_i^2 \rangle = \int_{-\infty}^{0} \frac{d\tilde{t}}{\tau} \int_{\tilde{t}}^{\infty} \frac{d\delta}{\tau} \mathrm{acf}(|\delta|) \partial_t G_{ij}(\tilde{t}) \partial_t G_{ij}(\tilde{t} - \delta), \tag{81}$$

where $\partial_t G_{ij}$ denotes the partial derivative of the propagator $G_{ij}(t' - t)$ with respect to t and $\omega_i = \dot{\alpha}_i$ the frequency at node i. See Eqs. (104)-(110) in the Supplemental Material (Sec. 5.8) for the derivation.

5.4 LOCALIZATION OF INCREMENT PDF VARIANCES

We now test our approach (81) numerically and analyze the propagation and localization of frequency increment statistics in linear chains of N coupled oscillators obeying Swing Eq. (78). We emphasize that our linearization approach is principally applicable to more complex networks.

In our setup, solely node $j = 1$ is driven by a stochastic signal $\delta P_j(t)$, which we obtain by means of a stochastic differential equation and subsequent modification of the power spectrum [32] (details in the Supplemental Material, Sec. 5.8). As a result, the time series $\delta P_j(t)$ reproduces key features of wind power generation data: extreme events, temporal correlations, characteristic power spectrum with -5/3 decay, and heavy-tailed increment statistics. We have $\mathrm{var}(\delta P_j) = 2.3$ MW and choose a grid with no initial power transfer, i.e., $P_i^0 = 0$ for all i. Increment variances obtained from direct numerical simulations of a chain of $N = 20$ oscillators show good agreement with the response theory, Eq. (81), see Fig. 13. The absolute amplitude of fluctuations decreases exponentially – apart from boundary effects – with distance from the perturbation, confirming the localization of the fluctuations.

The impact of reduced grid inertia J is of considerable importance for future power grids fed by a high share of renewable sources providing no inertia per se [98]. Decreasing the inertia J in our model system leads, as expected, to higher fluctuation amplitudes, Fig. 13 inset. However, as the semilogarithmic plot reveals, decreasing J while letting the damping γ remain constant causes a *faster* decay of the increment variance. So, how exactly does the exponential decay depend on the system parameters?

Increasing the inertia J while keeping γ constant increases the Laplace eigenvalues Λ_n. For chain-like grids with a large number of nodes

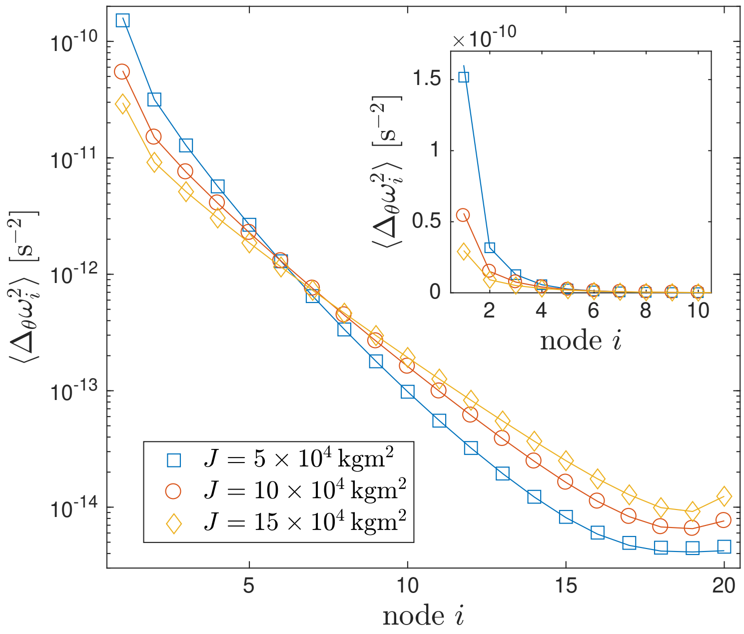

Figure 13: Evolution of the variance $\langle \Delta_\theta \omega_i^2 \rangle$ of increment PDFs $p(\Delta_\theta \omega_i)$ ($\theta = 0.01$ s) in a chain system of $N = 20$ oscillators from linear response theory Eq. (81) (solid lines) and direct Runge-Kutta simulations (symbols). Node $j = 1$ is driven by the perturbation signal $\delta P(t)$. We choose $\theta = 0.01$ s because $\delta P(t)$ shows the largest deviations from the Gaussian distribution on small timescales.

$N \gg 1$ and all nonzero $\Lambda_n > 1$, we find that the variance of short-term frequency increments, Eq. (81), can be approximated by

$$\langle \Delta_\theta \omega_i^2 \rangle \approx \frac{1}{JK\omega_0} \exp\left(-\frac{i-1}{\xi}\right) \langle \Delta_\theta \delta P_1^2 \rangle, \tag{82}$$

where $\langle \Delta_\theta \delta P_1^2 \rangle$ is the second moment of the increment PDF of the disturbance at site $j = 1$. We have used the Kolmogorov power spectrum $S(f) \propto f^{-5/3}$ of $\delta P_1(t)$. For the derivation, see Eqs. (111)-(123) in the Supplemental Material (Sec. 5.8). Thus, we confirm analytically that the second moment of the frequency increments is exponentially decaying with distance i from the position of the disturbance and find the correlation length

$$\xi = \nu\tau/2 = \sqrt{JK}/(2\sqrt{\omega_0}\gamma). \tag{83}$$

We confirm the correlation length ξ with numerical investigations of slightly longer chains ($N = 50$) to reduce finite-size effects, Fig. 14: Once J exceeds a critical value $J_c = \omega_0\gamma^2 N^2/\pi^2 K \approx 1.6 \cdot 10^6$ kgm^2, all nonzero eigenvalues Λ_n are larger than one (Fig. 14 b) and the slope m of the exponential decay is well fitted by $m = -1/\xi$ (Fig. 14 c), where ξ is given by Eq. (83). In the case of low inertia $J < J_c$, there are eigenvalues with $0 < \Lambda_n < 1$. Such Λ_n cause modes which decay more slowly with relaxation rates $\Gamma_n < 1/\tau$. If all $\Lambda_n < 1$, the

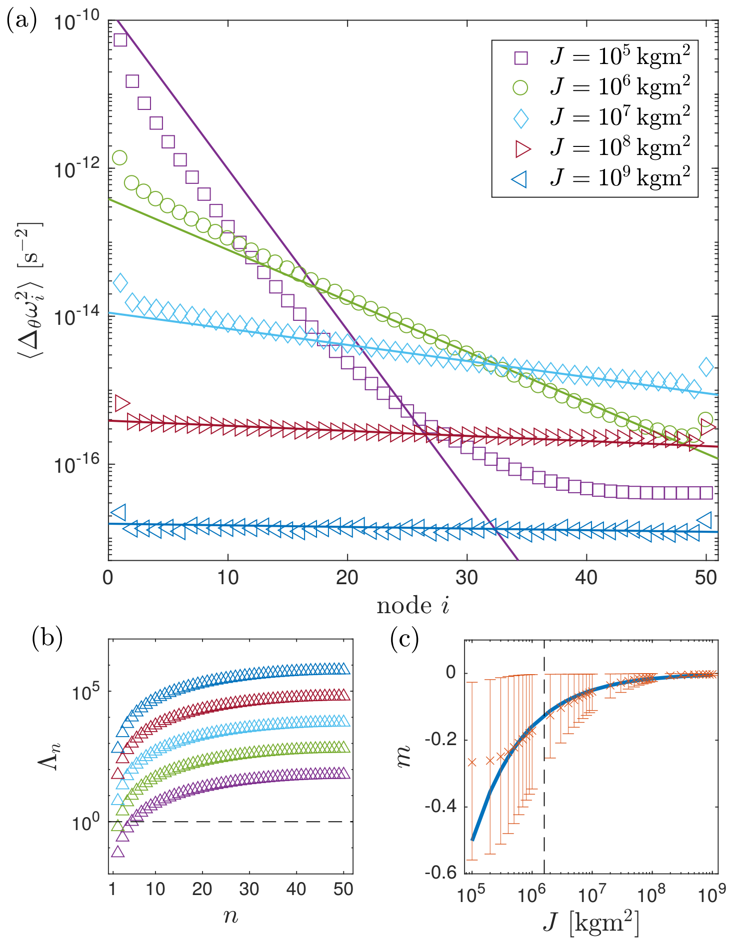

Figure 14: *(a)* Variance $\langle \Delta_\theta \omega_i^2 \rangle$ from Runge-Kutta simulations of a chain of $N = 50$ oscillators (symbols) compared to an exponential decay with slope $m = -1/\xi = -2\sqrt{\omega_0}\gamma/\sqrt{JK}$ (straight lines). *(b)* Eigenvalues Λ_n for increasing inertia J (color coded, Λ_n increase with increasing J). The dashed line marks $\Lambda_n = 1$. *(c)* Exponential fits (orange data with errorbars) of m converge to our analytical prediction $m = -1/\xi$ (Eq. (83), solid blue line) for increasing inertia J. The vertical dashed line marks J_c. Error bars correspond to the 2σ confidence bound of the exponential fit.

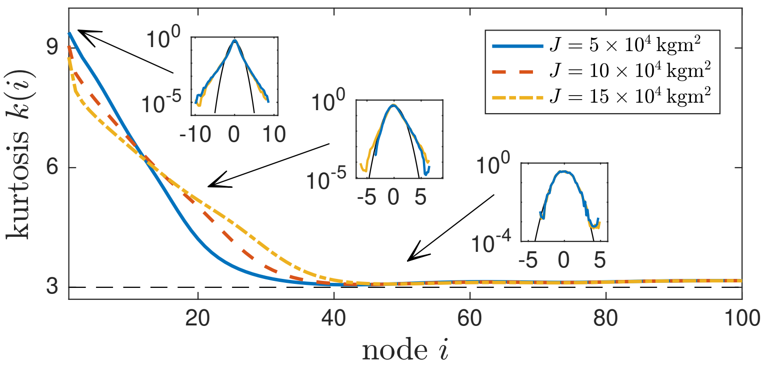

Figure 15: Kurtosis k of $p(\Delta_\theta \omega_i)$ in a longer chain of $N = 100$ oscillators. The frequency increment distribution $p(\Delta_\theta \omega_i)$ deforms only slowly towards an (almost) Gaussian distribution (insets, from left to right $i = 2, 20, 50$, $\theta = 0.01$ s). Results were obtained from direct Runge-Kutta simulations.

propagator Eq. (80) gets the form of a diffusion propagator [30] for which we expect that the variance of frequency increments decays with distance more slowly, with a power law. We observe the transition to such diffusive behavior in Fig. 14 a for $J = 10^5$ kg m^2, where the exponential decay only lasts up to node $i \approx 15$. Farther away, the slowly decaying soft modes dominate.

5.5 KURTOSIS EVOLUTION

Finally, we analyze the evolution of the shape of the increment PDFs in terms of their kurtosis k. Interestingly, the non-Gaussian shape persists much longer than the absolute fluctuation amplitudes (see Fig. 15 in comparison to the Fig. 13 inset). In numerical simulations of a chain of $N = 100$ oscillators, we observe that the short-term increment PDF deforms towards an almost Gaussian distribution only after approximately 40 nodes, see also the insets of Fig. 15. Surprisingly, we observe only a linear decay of the kurtosis k with distance until it approaches $k \approx 3$, which corresponds to a Gaussian distribution. This slow decay is in strong contrast to the exponential decay of the fluctuation amplitude observed until approximately node 15, Fig. 14, confirming that the non-Gaussian shape persists over long ranges. Again, the grid inertia seems to play a crucial role: Decreasing the inertia leads to higher kurtosis values, which means heavier tails, but also to a faster deformation towards a Gaussian distribution.

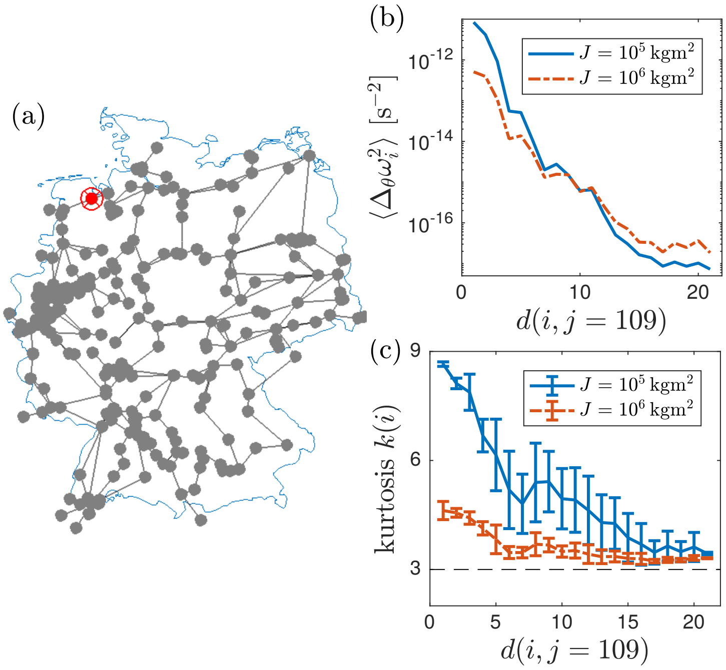

Figure 16: *(a)* SciGrid topology of the 380 kV grid in Germany [107] with homogeneous parameters as in the preceding simulations. The fluctuating perturbation $\delta P_i(t)$ is injected at node $j = 109$ (highlighted in red). *(b)* Variance of the short-term increments $\Delta_\theta \omega_i$ plotted against distance $d(i,j)$ to the perturbation. Here, we choose the shortest path distance and average the variances for all nodes with the same $d(i,j)$. The timescale is $\theta = 0.01$ s. *(c)* Evolution of the kurtosis $k(i)$ of the increments $\Delta_\theta \omega_i$. The errorbars correspond to the standard deviation of the kurtosis of nodes with the same distance $d(i,j)$. In (b), we omit errorbars due to the logarithmic y-axis.

5.6 COMPLEX NETWORK

In a numerical study, we show that the propagation of fluctuations is qualitatively similar on a complex topology, Fig. 16. We choose the SciGrid topology [107] which we perturb at a single node, Fig. 16 a. The decay of the variance of short term increments $\Delta_\theta \omega_i$ is getting steeper with decreasing inertia J and approximately follows an exponential curve, Fig. 16 b. Similar to our observation in linear chains, the non-Gaussian shape persists over long ranges: The kurtosis values are larger for low inertia and decrease slowly, not exponentially, with distance to the perturbation, Fig. 16 c.

5.7 CONCLUSIONS

In this article, we have analyzed the spreading of short-term frequency fluctuations in power grids induced by wind power feed-in.

While the influence of wind power is clearly visible in the short-term fluctuations in Oldenburg (with a large installed capacity of wind power generators [105]), the Göttingen measurements (with a rather small installed capacity [105]) do not show such an effect. Our analytical and numerical investigations show that the amplitudes of such short-term fluctuations damp out exponentially fast and form a local stochastic property of the frequency– as expected from our measurement. In contrast, the non-Gaussian shape of the frequency increment PDFs persists much wider in the grid and decays, in terms of kurtosis, only linearly with distance to the perturbation. Effects of topology and heterogeneity could further contribute to the effect we observe in the data, and that will be a subject of further research. Here, we focused on the most basic mechanism, namely, if the spatial propagation can explain our observation.

The amplitudes of the frequency fluctuations we observe are small (few mHz, Fig. 12). Hence, they do not cause risks for outages. Short-term fluctuations are expected to further decrease when the feed-in of many wind farms is aggregated. However, in future power grids mainly fed by wind and solar power, the interplay between the locality of short-term fluctuations and wide-scale averaging will be of interest for maintaining a high power quality. Further, we emphasize the subtle role of long-ranging soft modes induced by reducing the inertia in the grid.

Our analytical expressions help to estimate the timescale-dependent impact of fluctuations on power grids: For short timescales, this concerns, for example, the configuration of power converters feeding wind power to the grid. However, our analysis could be extended to longer timescales of minutes when the dynamics of primary and secondary control are included. On such timescales, the amplitudes of power increments $\Delta_\theta P$ of wind turbines are much larger and, hence, our theory may then help to develop different strategies for decentral frequency control. Further, our analysis of small-signal fluctuations in power grid frequency measurements, well situated within the linear response regime, will help to elaborate general results on networks of coupled oscillators, such as transient spreading dynamics [108] or optimal noise-canceling topologies [109].

5.8 SUPPLEMENTAL MATERIAL

5.8.1 *Grid frequency measurements in the public power grid*

We measured the grid frequency at two locations in the public distribution grid, namely our own lab in Oldenburg (Küpkersweg 70, 26129 Oldenburg, Germany) as well as a lab at Max Planck Institute for Dynamics and Self-Organization in Göttingen (Am Fassberg 17, 37077 Göttingen, Germany). We used identical setups at both sites and data evaluation techniques originating from our earlier work [102]:

We took 10 kHz voltage samplings $u(t)$ of a single phase. Subsequently, we applied the method of *Instantaneous Frequency* (IF) [91] to estimate the frequency time series $f(t)$ from the sinusoidal voltage signal $u(t)$.

The IF reveals the dominant frequency component at each time instant t and is thus suited for signals composed of one major frequency component. The method makes use of the fact that real-valued signals, such as the voltage signal $u(t)$, have conjugate symmetric Fourier representations, $\mathcal{F}[u](-\omega) = \mathcal{F}[u](\omega)^*$. Here, $\mathcal{F}$ denotes Fourier transform. The complex-valued analytic signal $z(t)$ is the inverse Fourier transform of the positive frequencies $\omega > 0$. Discarding the redundant negative frequency components makes the IF accessible. It is defined as the time derivative of the phase $\Phi(t)$ of the analytic signal $z(t)$:

$$f(t) = \frac{1}{2\pi}\frac{d}{dt}\Phi(t) = \frac{1}{2\pi}\frac{d}{dt}\arg(z(t)). \tag{84}$$

In practice, $z(t)$ is obtained from the Hilbert transform $\mathcal{H}[u](t)$ of the original signal: $z(t) := u(t) + i\mathcal{H}[u](t)$. The Hilbert transform can be obtained from $\mathcal{H}[u](t) = (u * 1/\pi t')(t)$, where "$*$" denotes convolution.

To estimate the derivative in Eq. (84) numerically, the phase $\Phi(t)$ was calculated for every time step in the voltage signal. Subsequently, the time derivative was estimated by linear fits of $\Phi(t)$ in disjoint blocks of 2000 samples. This procedure gives a frequency time series $f(t)$ with a time resolution of 200 ms. The 2σ-confidence bounds of the linear fits are, in average, of size $\pm$ 1 mHz.

5.8.2 *Stochastic process for synthetic wind power production data*

Power production time series $P(t)$ of renewable generators show certain statistic similarities to turbulence [25, 26]: We find long-range correlations and a characteristic Kolmogorov power spectrum $S(f)$ decaying with $f^{-5/3}$. Further, on small time scales θ, the PDFs of increments $\Delta_\theta P(t) = P(t+\theta) - P(t)$ show heavy tails severely deviating from the Gaussian distribution. Such tails describe the increased probability of extreme fluctuations on short scales, an effect often referred to as *intermittency* in turbulence research [110].

In our numerical studies, we perturb the power grid with synthetically generated wind power feed-in timeseries which show the above-mentioned key properties. Such properties were shown to be essential for adequate modeling of frequency fluctuations induced by stochastic feed-in [32, 33]. To isolate the effect of perturbation spreading in our simulations, we use grids with no initial power, i.e. $P_i^0 = 0$ for all

i, and perturb the system with signals $\delta P_j(t)$ at node j. We remark that all our results are as well applicable to grids with initial loads.

The dimensionless perturbation timeseries $\delta\Pi_j(t)$ is decomposed into a stochastic part $x(t)$ and an amplitude $\widehat{P}$ for which we chose $\widehat{P} = 1$ MW.

$$\delta\Pi_j(t) = \frac{J}{\gamma^2\omega_0}\widehat{P}\cdot x(t). \tag{85}$$

The stochastic part $x(t)$ is obtained by means of the procedure introduced in [32]: First, a time series $\tilde{x}(t)$ is generated integrating the Langevin-type system of equations

$$\dot{y} = -\gamma y + \Gamma(t), \tag{86}$$

$$\dot{\tilde{x}} = \tilde{x}\left(g - \frac{\tilde{x}}{x_0}\right) + \sqrt{D\tilde{x}^2}y, \tag{87}$$

with $\gamma = 1.0$, $g = 0.5$, $x_0 = 2.0$ and Γ being white Gaussian noise. The parameter D serves to tune the degree of intermittency. Here we set $D = 2.0$, which corresponds to strongly intermittent noise.

In a next step, the resulting Fourier spectrum is modified so that the final power spectrum reproduces the Kolmogorov -5/3 decay: $S(f) \propto f^{-5/3}$. Transforming back to real space and normalization eventually yields $x(t)$.

We show a short part of the time series $\delta P_i(t)$ accompanied by the short-term increment PDF and power spectrum in Fig. 17. In the numerical simulations, we use a time step $dt = 0.01$ sec and integrate the system with intermittent noise $\delta P_i(t)$ of length 19,800 sec with a Runge-Kutta scheme of order 4.

5.8.3 *Linear response theory of power grids exposed to stochastic perturbations*

We start from the Swing Equation,

$$\tau^2\ddot{\alpha}_i + 2\tau\dot{\alpha}_i = \frac{J}{\gamma^2\omega_0}P_i(t) - \sum_{j=1}^{N}\frac{J}{\gamma^2\omega_0}K_{ij}\sin(\vartheta_i^0 - \vartheta_j^0 + \alpha_i - \alpha_j), \tag{88}$$

which models the deviations $\alpha_i(t) = \vartheta_i(t) - \vartheta_i^0$ of the phase $\vartheta_i(t)$ at node i and time t from the stable fixed point ϑ_i^0. Here, J is the inertia at each node, $\gamma = J/\tau$ is the damping constant and τ is the relaxation time scale. We consider time dependent production and consumption $P_i(t) = P_i^0 + \delta P_i(t)$, where the P_i^0's correspond to the

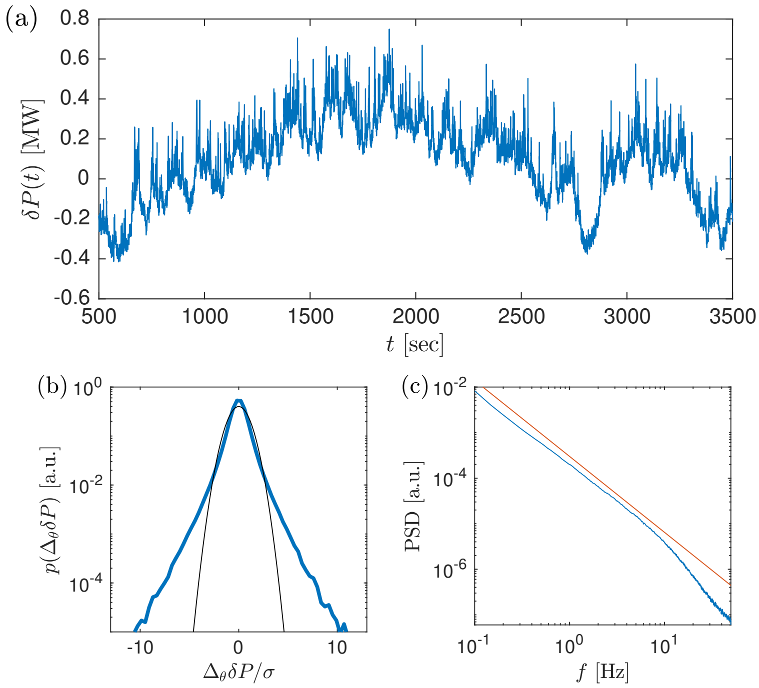

Figure 17: **Synthetic wind power time series reproduce key stochastic features of real wind power generation data.** *(a)* Short part of synthetic time series $\delta P_j(t)$ used for the numerical investigations. *(b)* The PDF of short-term ($\theta = 0.01$ sec) increments $\Delta_\theta \delta P(t) = \delta P(t+\theta) - \delta P(t)$ shows severe deviations from the Gaussian distribution (black curve) in its tails. x-axis is plotted in units of the standard deviation σ of increments $\Delta_\theta \delta P(t)$. *(c)* The power spectral density decays as $S(f) \propto f^{-5/3}$ (orange reference curve). This reproduces the characteristic Kolmogorov spectrum from turbulence.

stable fixed point. For small deviations $|\alpha_i|$, we may linearize Eq. (88) about the stable fixed point and find

$$\tau^2 \ddot{\alpha}_i + 2\tau\dot{\alpha}_i = -\sum_{j=1}^{N} \frac{J}{\gamma^2 \omega_0} K_{ij} \cos(\vartheta_i^0 - \vartheta_j^0)(\alpha_i - \alpha_j) + \frac{J}{\gamma^2 \omega_0} \delta P_i(t). \quad (89)$$

We define the generalized Laplacian Λ as

$$\Lambda_{ij} = \begin{cases} -\frac{J}{\gamma^2 \omega_0} K_{ij} \cos(\vartheta_i^0 - \vartheta_j^0) & \text{if } i \neq j \\ \frac{J}{\gamma^2 \omega_0} \sum_j K_{ij} \cos(\vartheta_i^0 - \vartheta_j^0) & \text{if } i = j \end{cases} \quad (90)$$

and write

$$\tau^2 \ddot{\alpha}_i + 2\tau\dot{\alpha}_i + \sum_{j=1}^{N} \Lambda_{ij}\alpha_j = \frac{J}{\gamma^2 \omega_0} \delta P_i(t). \quad (91)$$

Further, we introduce $\delta\Pi_i(t) = J\delta P_i(t)/(\gamma^2\omega_0)$ to obtain

$$\tau^2\ddot{\alpha}_i + 2\tau\dot{\alpha}_i + \sum_{j=1}^{N} \Lambda_{ij}\alpha_j = \delta\Pi_i(t). \tag{92}$$

We now write the phase deviation $\alpha_i(t)$ as a generalized Fourier series by writing its time dependence as a Fourier integral and expanding its spatial dependence in terms of the eigenvectors $\boldsymbol{\phi}_n$ of the generalized Laplacian Λ, defined by $\Lambda\boldsymbol{\phi}_n = \Lambda_n\boldsymbol{\phi}_n$, where Λ_n are its eigenvalues [30, 34, 77, 111]. Thereby we obtain [30, 112]

$$\alpha_i(t) = \int_{-\infty}^{\infty} d\epsilon \sum_{n=0}^{N-1} c_n(\epsilon)\phi_{ni}e^{-i\epsilon t}. \tag{93}$$

Expanding the disturbance likewise in a generalized Fourier series we get

$$\delta\Pi_i(t) = \int_{-\infty}^{\infty} d\epsilon \sum_{n=0}^{N-1} \eta_n(\epsilon)\phi_{ni}e^{-i\epsilon t}. \tag{94}$$

Here, the Fourier components of the disturbance are defined by

$$\eta_n(\epsilon) = \int_{-\infty}^{\infty} \frac{dt'}{2\pi} e^{i\epsilon t'} \sum_{i=1}^{N} \delta\Pi_i(t')\phi_{ni}^*. \tag{95}$$

We now insert the expansions for $\alpha_i(t)$ and $\delta\Pi_i(t)$ into Eq. (92) and find, requiring that the equation is fulfilled for each term of the Fourier series, [34]

$$\left(-\tau^2\epsilon^2 - i2\tau\epsilon + \Lambda_n\right) c_n(\epsilon) = \eta_n(\epsilon). \tag{96}$$

For a given disturbance, the Fourier component of the phase deviation $c_n(\epsilon)$ is thus given in response to the one of the disturbance $\eta_n(\epsilon)$. Inserting that expression for $c_n(\epsilon)$ back into the Fourier series we get [34]

$$\alpha_i(t) = \int_{-\infty}^{\infty} d\epsilon \sum_{n=0}^{N-1} \left(-\tau^2\epsilon^2 - i2\tau\epsilon + \Lambda_n\right)^{-1} \eta_n(\epsilon)\phi_{ni}e^{-i\epsilon t}. \tag{97}$$

The integral over the angular frequency ϵ can be performed by means of the residuum theorem, noting that there are two poles in the lower complex plane, $\epsilon_{n\pm} = -i(1 \pm \sqrt{1-\Lambda_n})1/\tau$. Inserting Eq. (95) into Eq. (97) yields

$$\alpha_i(t) = \int_{-\infty}^{\infty} d\epsilon \int_{-\infty}^{\infty} \frac{dt'}{2\pi} \sum_{n=0}^{N-1} (-\tau^2\epsilon^2 - 2i\tau\epsilon + \Lambda_n)^{-1} \times \sum_{j=1}^{N} \delta\Pi_j(t')\phi^*_{nj}\phi_{ni} e^{i\epsilon(t'-t)} \tag{98}$$

$$= \int_{-\infty}^{t} \frac{dt'}{2\pi}(-2\pi i) \sum_{n=0}^{N-1} \sum_{\pm} \frac{-e^{i\epsilon_\pm(t'-t)}}{\tau^2(\epsilon_\pm - \epsilon_\mp)} \sum_{j=1}^{N} \delta\Pi_j(t')\phi^*_{nj}\phi_{ni} \tag{99}$$

$$= \int_{-\infty}^{t} dt' \sum_{n=0}^{N-1} \sum_{\pm} \frac{i\, e^{i\epsilon_\pm(t'-t)}}{\tau^2(\epsilon_\pm - \epsilon_\mp)} \sum_{j=1}^{N} \delta\Pi_j(t')\phi^*_{nj}\phi_{ni}. \tag{100}$$

We have closed the integration path of ϵ clock-wise in the lower complex plane for $t' < t$. For $t' > t$, the path must be closed in the upper complex plane where no poles are present. Hence there are no contributions "from future" ($t' > t$) to the integral [34]. We remark that for $n = 0$, $\Lambda_0 = 0$ and hence $\epsilon_{0-} = 0$. Given that this pole lies on the real axis, its contribution must be multiplied with a factor 1/2. However, this contribution corresponds to a constant phase shift which does not impact the frequency $\omega_i(t)$ which we analyze in the following.

By replacing $\epsilon_\pm - \epsilon_\mp = \mp\frac{2i}{\tau}\sqrt{1-\Lambda_n}$ we obtain the expression

$$\alpha_i(t) = \int_{-\infty}^{t} \frac{dt'}{\tau} \sum_{j=1}^{N} \delta\Pi_j(t') G_{ij}(t'-t) \tag{101}$$

where the propagator $G_{ij}(t'-t)$ is defined by

$$G_{ij}(t'-t) = \sum_{n=0}^{N-1} \sum_{\sigma=\pm 1} \frac{\phi_{ni}\phi^*_{nj}}{2\sqrt{1-\Lambda_n}} (-\sigma) e^{(1+\sigma\sqrt{1-\Lambda_n})\frac{t'-t}{\tau}}. \tag{102}$$

For the frequency $\omega_i(t) = \dot{\alpha}_i(t)$ we find

$$\omega_i(t) = \frac{d}{dt}\left[\int_{-\infty}^{t} \frac{dt'}{\tau} \sum_{j=1}^{N} \delta\Pi_j(t') G_{ij}(t'-t)\right] \tag{103}$$

$$= \int_{-\infty}^{t} \frac{dt'}{\tau} \sum_{j=1}^{N} \delta\Pi_j(t') \partial_t G_{ij}(t'-t). \tag{104}$$

We remark that the boundary terms are equal to zero because $G_{ij}(0)$ vanishes due to the summation over $\sigma = \pm 1$. For the t-derivative of the propagator we find

$$\partial_t G_{ij}(t'-t) = \sum_{n=0}^{N-1} \sum_{\sigma=\pm 1} \frac{\phi_{ni}\phi_{nj}^*}{2\sqrt{1-\Lambda_n}}(-\sigma) \times \left(-\left(\frac{1+\sigma\sqrt{1-\Lambda_n}}{\tau}\right)\right) e^{(1+\sigma\sqrt{1-\Lambda_n})\frac{t'-t}{\tau}} \tag{105}$$

$$= \sum_{n=0}^{N-1} \sum_{\sigma=\pm 1} \frac{\phi_{ni}\phi_{nj}^*}{2\sqrt{1-\Lambda_n}} \left(\frac{\sigma}{\tau} + \frac{\sqrt{1-\Lambda_n}}{\tau}\right) e^{(1+\sigma\sqrt{1-\Lambda_n})\frac{t'-t}{\tau}}. \tag{106}$$

To derive an expression for the variance of the frequency increment statistics $\langle \Delta_\theta \omega_i^2 \rangle$, we first evaluate Eq. (104) at time $t+\theta$ and, subsequently, substitute $\hat{t} = t' - \theta$:

$$\omega_i(t+\theta) = \int_{-\infty}^{t} \frac{d\hat{t}}{\tau} \sum_{j=1}^{N} \delta\Pi_j(\hat{t}+\theta)\partial_t G_{ij}(\hat{t}-t). \tag{107}$$

Therewith, the increment $\Delta_\theta \omega_i(t) = \omega_i(t+\theta) - \omega_i(t)$ follows as

$$\Delta_\theta \omega_i(t) = \int_{-\infty}^{t} \frac{dt'}{\tau} \sum_{j=1}^{N} \Delta_\theta \delta\Pi_j(t')\partial_t G_{ij}(t'-t). \tag{108}$$

Finally, we focus on the case where a single node j is driven by noise. We multiply Eq. (108) with itself and apply an ensemble average $\langle \cdot \rangle$ over noise realizations to obtain

$$\langle \Delta_\theta \omega_i^2 \rangle = \int_{-\infty}^{t} \frac{dt'}{\tau} \int_{-\infty}^{t} \frac{dt''}{\tau} \left\langle \Delta_\theta \delta\Pi_j(t')\Delta_\theta \delta\Pi_j(t'') \right\rangle \times \partial_t G_{ij}(t'-t)\partial_t G_{ij}(t''-t). \tag{109}$$

We find $\mathrm{acf}(|t'-t''|) := \left\langle \Delta_\theta \delta\Pi_j(t')\Delta_\theta \delta\Pi_j(t'') \right\rangle$, define $\delta := t'-t''$ and $\tilde{t} = t'-t$ and finally obtain

$$\langle \Delta_\theta \omega_i^2 \rangle = \int_{-\infty}^{0} \frac{d\tilde{t}}{\tau} \int_{\tilde{t}}^{\infty} \frac{d\delta}{\tau} \mathrm{acf}(|\delta|)\partial_t G_{ij}(\tilde{t})\partial_t G_{ij}(\tilde{t}-\delta). \tag{110}$$

5.8.4 *Analytical derivation of frequency increment moments for a chain of nodes*

For the chain with open boundary conditions we find the eigenvalues of the generalized Laplacian to be $\Lambda_n = 2\Pi_K(1-\cos(k_n)) = 4\Pi_K \sin(k_n/2)^2$, for $n = 0, .., N-1$. Here, $\Pi_K = JK/(\omega_0\gamma^2)$ and $k_n =$

$n\pi/N$. The eigenvectors $\boldsymbol{\phi}_n$ are $\phi_{0i} = 1/\sqrt{N}$ for $n = 0$ and $\phi_{ni} = \sqrt{2}/\sqrt{N}\cos(k_n(i-1/2))$, for $n = 1, .., N-1$.

We consider the case of large inertia J when all nonzero eigenvalues are much larger than one, $\Lambda_n \gg 1$. Given that $\Lambda_1 = 4\Pi_K \sin^2(\pi/(2N)) \approx 4\Pi_K\pi^2/(4N^2)$ is the smallest nonzero eigenvalue, we find this condition fulfilled for $J \gg J_c = \omega_0\gamma^2N^2/(\pi^2K)$. In this regime, we approximate $\sqrt{1-\Lambda_n} \approx i\sqrt{\Lambda_n}$. Inserting eigenvectors $\boldsymbol{\phi}_n$ and eigenvalues Λ_n into the expression for the propagator $G_{ij}(t'-t)$, Eq. (102), yields

$$\begin{aligned} G_{ij}(\Delta t = t-t') &= \frac{1}{2N}\left(1-e^{-2\Delta t/\tau}\right) + e^{-\Delta t/\tau}\frac{1}{N\sqrt{\Pi_K}} \\ &\times \sum_{n=1}^{N-1} \frac{\cos\frac{\pi n(i-\frac{1}{2})}{N}\cos\frac{\pi n(j-\frac{1}{2})}{N}\sin\left(2\sqrt{\Pi_K}\sin(\frac{\pi}{2}\frac{n}{N})\frac{\Delta t}{\tau}\right)}{\sin(\frac{\pi}{2}\frac{n}{N})}. \end{aligned} \tag{111}$$

For large $N \gg 1$ we can turn the summation in an integral over $x = n/N$ with $dx = 1/N$. Thus, we get

$$\begin{aligned} G_{ij}(\Delta t)|_{N\gg 1} &= \frac{e^{-\Delta t/\tau}}{\sqrt{\Pi_K}}\int_0^1 dx \frac{\cos(\pi x(i-\frac{1}{2}))\cos(\pi x(j-\frac{1}{2}))}{\sin(\frac{\pi}{2}x)} \\ &\times \sin\left(2\sqrt{\Pi_K}\sin(\frac{\pi}{2}x)\frac{\Delta t}{\tau}\right). \end{aligned} \tag{112}$$

Noting that $0 < x < 1$, we further approximate $\sin(\frac{\pi}{2}x) \approx \frac{\pi}{2}x$ and perform the integrals to get

$$G_{ij}(\Delta t)|_{N\gg 1} = \frac{e^{-\Delta t/\tau}}{\sqrt{\Pi_K}} g(i,j,\Delta t), \tag{113}$$

where

$$\begin{aligned} g(i,j,\Delta t) &= \frac{1}{2\pi}\left(\mathrm{Si}[\pi(\nu\Delta t - i + j)] + \mathrm{Si}[\pi(\nu\Delta t + i - j)]\right) \\ &+ \frac{1}{2\pi}\left(\mathrm{Si}[\pi(\nu\Delta t - i - j + 1)] + \mathrm{Si}[\pi(\nu\Delta t + i + j - 1)]\right). \end{aligned} \tag{114}$$

$\mathrm{Si}(x) = \int_0^x \sin(y)/y\, dy$ is the Sine Integral. Further, we have introduced the velocity $\nu = \sqrt{\Pi_K}/\tau$.

In this article, we consider perturbations at one end of the chain, i.e., site $j = 1$. Hence, we need to know the propagator from site 1 to i. The function $g(i,1,\Delta t)$ turns out to be a step function in $i-1-\nu\Delta t$ with only weak superimposed oscillations. Thus, we can approximate $g(i,1,\Delta t) \approx 1$ for $i-1 < \nu\Delta t$ and 0 otherwise, that is, it is a unit step down function. Inserting this into Eq. (101), we find the change of phase in response to the perturbation at site $j = 1$ to be

$$\alpha_i(t) = \frac{1}{\nu\tau}\int_{-\infty}^{t-(i-1)/\nu} \frac{dt'}{\tau}\delta\Pi_1(t')e^{-(t-t')/\tau}. \tag{115}$$

Taking the time derivative we find for the frequency deviation at node i

$$\omega_i(t) = -\frac{1}{\tau}\alpha_i(t) + \frac{1}{\nu\tau^2}\delta\Pi_1(t-(i-1)/\nu)e^{-\frac{i-1}{\nu\tau}}. \tag{116}$$

In this approximation, we find for the variance of the frequency increment statistics

$$\begin{aligned}\langle\Delta_\theta\omega_i^2\rangle =& \frac{1}{\tau^2}\langle\Delta_\theta\alpha_i^2\rangle \\ &+ \frac{2}{\nu\tau^3}\langle\Delta_\theta\alpha_i(t)\Delta_\theta\delta\Pi_1(t-(i-1)/\nu)\rangle e^{-\frac{i-1}{\nu\tau}} \\ &+ \frac{1}{\nu^2\tau^4}\langle\Delta_\theta\delta\Pi_1^2\rangle e^{-\frac{2(i-1)}{\nu\tau}}.\end{aligned} \tag{117}$$

The signal $\delta\Pi_1(t)$ we are perturbing the system with has a power spectral density $S(f) \propto f^{-5/3}$. Following Wiener-Khinchin theorem, we obtain for the variance of the increment statistics

$$\langle\Delta_\theta\delta\Pi_1^2\rangle = c\theta^{2/3}. \tag{118}$$

This allows us to calculate also the increments of frequency fluctuations and their moments: Inserting Eq. (115) into Eq. (117), we obtain for the second moment of the frequency increments

$$\langle\Delta_\theta\omega_i^2\rangle = \frac{1}{\tau^2\Pi_K}c\tau^{2/3}e^{-2\frac{i-1}{\nu\tau}}L(\theta/\tau), \tag{119}$$

where the function $L(\theta/\tau)$ is given by

$$\begin{aligned}L(x=\theta/\tau) =& x^{2/3} \\ &+ 2\int_{-\infty}^{0} ds_1 \int_{-\infty}^{0} ds_2 e^{s_1+s_2}\left(|s_1-s_2|^{2/3} - |s_1-s_2-x|^{2/3}\right) \\ &+ e^{-x}\int_0^x ds e^s s^{2/3} - 2\Gamma(5/3)(1-\cosh x).\end{aligned} \tag{120}$$

The integrals can be expressed in terms of incomplete Gamma functions $\Gamma(5/3, x)$ as

$$\begin{aligned}L(x=\theta/\tau) =& x^{2/3} + \frac{2\pi}{\sqrt{3}\Gamma(-2/3)}(e^{-x}-2) \\ &- e^x\Gamma(5/3,x) - 2\Gamma(5/3)(1-\cosh x).\end{aligned} \tag{121}$$

For $\theta/\tau < 1$, the leading order is $L(x=\theta/\tau) = x^{2/3} + 3/5x^{5/3} + O(x^2)$ and hence we find for $\theta < \tau$

$$\langle\Delta_\theta\omega_i^2\rangle \approx \frac{1}{\tau^2\Pi_K}\exp\left(-\frac{i-1}{\xi}\right)\langle\Delta_\theta\delta\Pi_1^2\rangle \tag{122}$$

$$\approx \frac{1}{JK\omega_0}\exp\left(-\frac{i-1}{\xi}\right)\langle\Delta_\theta\delta P_1^2\rangle, \tag{123}$$

where $\xi = \sqrt{JK}/(2\sqrt{\omega_0}\gamma)$.

At low inertia $J < J_c = \omega_0 \gamma^2 N^2/\pi^2 K$, there appear modes which decay more slowly with relaxation rates $\Gamma_n < 1/\tau$. Then, keeping only those slowly decaying modes with $\Lambda_n < 1$, we find

$$G_{ij}(\Delta t = t - t' > \tau)|_N \approx \frac{1}{2N} + \sum_{\{n|0<\Lambda_n<1\}} \frac{\phi_{ni}\phi^*_{nj}}{2(1-\Lambda_n/2)} e^{-\frac{1}{2}\Lambda_n \frac{t-t'}{\tau}}. \tag{124}$$

Approximating $\Lambda_n \approx \Pi_K a^2 k_n^2$ and using for large $N \gg 1$ the continuum approximation $k_n \to k$, we can perform the integral over k and find

$$G_{i1}(\Delta t = t - t' > \tau)|_N \approx \frac{1}{\sqrt{2\pi \Pi_K a^2 (t-t')/\tau}} \exp\left(-\frac{(i-1)^2}{2\Pi_K (t-t')/\tau}\right), \tag{125}$$

which has the form of a diffusion propagator with diffusion constant $D = \Pi_K a^2/\tau$ [30],

$$G_{i1}(\Delta t = t - t' > \tau)|_N \approx \frac{1}{\sqrt{2\pi D(t-t')}} \exp\left(-\frac{(i-1)^2 a^2}{2D(t-t')}\right). \tag{126}$$

In the last step, we have introduced a spatial scale a, the length of a transmission line, to define the diffusion constant D in the common way. However, we note that one could principally perform these calculations in terms of node indices as distance measure as before.

6 DETECTING HIDDEN UNITS AND NETWORK SIZE FROM PERCEPTIBLE DYNAMICS

This chapter (including the Supplemental Material) is, with minor editorial changes, identical to our publication

Haehne, H., Casadiego, J., Peinke, J., & Timme, M. (2019). Detecting Hidden Units and Network Size from Perceptible Dynamics. *Physical Review Letters*, 122(15), 158301.

Reprint with permission from APS.

ABSTRACT

The number of units of a network dynamical system, its size, arguably constitutes its most fundamental property. Many units of a network, however, are typically experimentally inaccessible such that the network size is often unknown. Here we introduce a *detection matrix* that suitably arranges multiple transient time series from the subset of accessible units to detect network size via matching rank constraints. The proposed method is model-free, applicable across system types and interaction topologies and applies to nonstationary dynamics near fixed points, as well as periodic and chaotic collective motion. Even if only a small minority of units is perceptible and for systems simultaneously exhibiting nonlinearities, heterogeneities and noise, *exact* size detection is feasible. We illustrate applicability for a paradigmatic class of biochemical reaction networks.

6.1 INTRODUCTION

Networks of interacting dynamical units prevail across natural and human-made systems [1, 8, 10]. Examples range from intracellular gene-regulatory networks critical for survival [5, 6] to power grids supplying electric energy on demand [7, 18–22] and to social and transportation networks determining how ideas and diseases spread [2, 113, 114]. Key properties of the physical interaction topology in such networks fundamentally underlie their function such that revealing them from measurements of the collective network dynamics constitutes a topical field of research [11, 15, 39–41, 43–49, 115].

However, dynamical data from many networks are often only incompletely accessible, because many of their units are hidden from measurements. Thus the dynamics of a possibly small subset of units

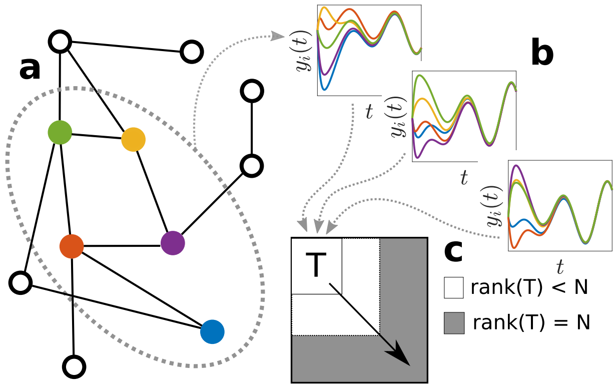

Figure 18: **Revealing network size from the dynamics of perceptible units.** *(a)* Scheme of a network of N units where only $n < N$ units (colored disks, encircled by dashed line) are accessible for measurement (perceptible). *(b)* Transient time series measured from accessible units, started from different initial conditions (trajectory colors match observable units in (a)). *(c)* Observed nonlinear, multidimensional time series are arranged into the *detection matrix* T_k, satisfying the condition $\text{rank}(T_k) = N$ if and only if $kn > N$ and $M > N$, according to (132) introduced below.

might be available only. Such hidden units typically complicate the inference of direct interactions by correlating or decorrelating the dynamics of measured units in unpredictable ways [116, 117]. Nevertheless, partial information about a networked system may provide hints about overall features of the network. For instance, approximating the network dynamics via model differential equations may help to detect the existence and location of a single hidden unit through heuristics performed on reconstructed connectivity matrices for different time windows [118–120]. Other schemes exploit dynamics to determine paths from observed, via hidden, to observed units [121–123] and typically require to know the exact number of hidden units *a priori*. Yet, how to reveal the number of many hidden units, or equivalently, the overall network size from time series recorded from the collective dynamics of accessible units remains generally unknown.

Here, we show that measuring the transient collective dynamics of a subset of perceptible network units (accessible to measurement) may robustly reveal the exact number of hidden units and thus identify the network size. We demonstrate how specifically grouping different transient time series obtained from perceptible units into a *detection matrix* yields bounds relating the rank of such matrix to the size of the full network, see Fig. 18. We propose a simple detection algorithm to exactly find the number of hidden units. The number of time series necessary to reliably identify network size only linearly scales with network size, thus making size detection scalable. The proposed method generalizes from linear and linearized dynamics near fixed points to dynamics near periodic orbits as well as to collective irregular and chaotic dynamics, without requiring knowledge of a system model. Even for systems simultaneously exhibiting nonlinearities, heterogeneities, and noise detection may be feasible and exact.

6.2 THEORY OF DETECTING NETWORK SIZE FROM OBSERVED DYNAMICS

Consider a network dynamical system

$$\dot{\boldsymbol{z}} = \mathbf{F}(\boldsymbol{z}), \tag{127}$$

of an unknown number N of coupled units $i \in \{1, \dots, N\}$, where $\boldsymbol{z}(t) := [z(t), z_2(t), \dots, z_N(t)]^\mathsf{T} \in \mathbb{R}^N$ is the system's state at time $t \in \mathbb{R}$ and $\mathbf{F} : \mathbb{R}^N \to \mathbb{R}^N$ an unknown smooth function that defines its rate of change and thereby the collective network dynamics. For simplicity, we first present the idea of identifying network size for noise-free linear dynamics close to fixed points and below discuss how it generalizes to more complex dynamics, including periodic and aperiodic, irregular dynamics, e.g., noisy and collective chaotic motion. Close to a fixed point $\boldsymbol{z}^*$ where $\mathbf{F}(\boldsymbol{z}^*) = 0$, a first order approximation of (127) in terms of $\boldsymbol{x}(t) = \boldsymbol{z}(t) - \boldsymbol{z}^*$ yields

$$\dot{\boldsymbol{x}}(t) = A\boldsymbol{x}(t) \tag{128}$$

where $A \in \mathbb{R}^{N \times N}$ with elements $A_{ij} = \partial F_i / \partial x_j\,(\boldsymbol{z}^*)$ is the Jacobian matrix of $\mathbf{F}$ evaluated at $\boldsymbol{z}^*$ and defines an unknown proxy for the connectivity of the system, i.e. $A_{ij} \neq 0$ if unit j directly acts on i and $A_{ij} = 0$ otherwise. Solving (128) yields $\boldsymbol{x}(t) = \exp(At)\boldsymbol{x}(0)$, where $\boldsymbol{x}(0) \in \mathbb{R}^N$ is a vector of initial conditions at $t = 0$ and $\exp(\cdot)$ denotes the matrix exponential function.

How can we uncover network size, i.e. find how many dynamical variables N the system has if we measure the dynamics of only $n < N$ variables? Without loss of generality, we observe the first n components of $\boldsymbol{x}(t)$ and all other $h = N - n$ state variables are hidden from measurement. The time series of measured states $\boldsymbol{y}(t) := [x_1(t), x_2(t), \dots, x_n(t)]^\mathsf{T} \in \mathbb{R}^n$ then satisfy the projection

$$\boldsymbol{y}(t) = \begin{bmatrix} I_n & 0 \end{bmatrix} \boldsymbol{x}(t) = \begin{bmatrix} I_n & 0 \end{bmatrix} \exp(At)\boldsymbol{x}(0), \tag{129}$$

where I_n is the $n \times n$ identity matrix and 0 represents the $n \times h$ matrix full of zeros. Thus we obtain the constraint

$$y_i(t) = \sum_{j=1}^{N} \theta_{ij}(t) x_j(0) \tag{130}$$

for every component $i \in \{1, 2, \dots, n\}$, where $\theta_{ij}(t) = [\exp(At)]_{ij}$ is some unknown, time-dependent function and $x_j(0)$ is the jth component of the initial state, equally unknown for $j \in \{n+1, \dots, N\}$. Our central question is now: can we find $h = N - n$ despite these many unknowns?

Rewriting the constraint (130) in matrix form yields

$$\mathbf{y}^{(m)}(t) = \Theta(t)\mathbf{x}^{(m)}(0), \tag{131}$$

where $\Theta(t) \in \mathbb{R}^{n \times N}$ and $\mathbf{y}^{(m)}(t)$ is the mth observable trajectory at time t generated from complete initial conditions $\mathbf{x}^{(m)}(0)$, different for different m. Considering M different trajectories yields a system $Y(t) = \Theta(t)X_0$, where $Y(t) := \left[\mathbf{y}^{(1)}(t), \mathbf{y}^{(2)}(t), \dots, \mathbf{y}^{(M)}(t)\right] \in \mathbb{R}^{n \times M}$ is the matrix of known dynamical states at time t and the matrix $X_0 := \left[\mathbf{x}^{(1)}(0), \mathbf{x}^{(2)}(0), \dots, \mathbf{x}^{(M)}(0)\right] \in \mathbb{R}^{N \times M}$ collects different initial conditions. If these trajectories are sampled at k different time points $t_1, \dots, t_k$, for each trajectory measured relative to its initial time, we group all values of $Y(t)$ evaluated up to time t_k into a *detection matrix*

$$T_{(k,M)} = \Theta_{(k)} X_0, \tag{132}$$

where $T_{(k,M)}(t_1, \dots, t_k) := \left[Y(t_1)^{\mathsf{T}}, \dots, Y(t_k)^{\mathsf{T}}\right]^{\mathsf{T}} \in \mathbb{R}^{kn \times M}$ and $\Theta_{(k)}(t_1, \dots, t_k) := \left[\Theta(t_1)^{\mathsf{T}}, \dots, \Theta(t_k)^{\mathsf{T}}\right]^{\mathsf{T}} \in \mathbb{R}^{kn \times N}$.[1] We note that here the lower indices k, M refer to the size ($kn \times M$) of the detection matrix, not to any element of a matrix.

Equation (132) linearly relates the detection matrix $T_{(k,M)}$ assembled from the M different time series sampled at k different times each, to unknown maps $\Theta_{(k)}$ encoding the dynamical evolution (i.e. consequences of the flow of the system) and to the initial conditions X_0 with also $(N - n)M$ unknown elements. Despite little is known about $\Theta_{(k)}$ and X_0, the time series merged into the linear system (132) already provide valuable information about the network size N. Specifically,

$$\operatorname{rank}\left(T_{(k,M)}\right) \leqslant \min\left\{\operatorname{rank}\left(\Theta_{(k)}\right), \operatorname{rank}\left(X_0\right)\right\}, \tag{133}$$

and the rank of $T_{(k,M)}$ generically increases with increasing the number M of time series ($\operatorname{rank}(X_0) = \min(N, M)$), as well as with increasing the number of sampling points k on each of them, because the rank of $\Theta_{(k)}$ increases ($\operatorname{rank}(\Theta_{(k)}) = \min(kn, N)$), until the rank is maximal and equals N. Merging sufficiently many time series, $M > N$, of sufficient length $k > N/n$ we obtain $\operatorname{rank}\left(\Theta_{(k)}\right) = \operatorname{rank}\left(X_0\right) = \operatorname{rank}\left(T_{(k,M)}\right) = N$. At this point, adding more time series, i.e. increasing M, or extending observations on each of them, i.e. increasing k, does not further increase $\operatorname{rank}\left(T_{(k,M)}\right)$ so computing the rank of the detection matrix $T_{(k,M)}$ assembled from time series of the subset of the n measured units yields the network size N via (132). Thus,

$$\hat{h} = \operatorname{rank}\left(T_{(k,M)}\right) - n \tag{134}$$

1 We remark that double transposition is required and that $T_{(k,M)}(t_1, \dots, t_k) \neq [Y(t_1), \dots, Y(t_k)]$

is the estimated number of hidden units. Interestingly, there is no principal lower bound on how small n must be for this relation to hold theoretically. In practice, measurement errors, noise and limits in the detection matrix condition number [124] limit feasible ratios n/N; see our analyses below.

6.3 ALGORITHM FOR DETECTING NETWORK SIZE FROM TIME SERIES DATA

One practical way of inferring network size through the rank inequality (133) is to numerically compute the ordered singular values $\sigma = (\sigma_1, \dots, \sigma_b)$ of $T_{(k,M)}$ such that $\sigma_1 \geqslant \sigma_2 \geqslant \dots \geqslant \sigma_b$, where $b = \min\{kn, M\}$ specifies the number of singular values, and to detect the largest $\Delta_{\max}$ of the gaps

$$\Delta_j = \log(\sigma_j) - \log(\sigma_{j+1}) \tag{135}$$

on the logarithmic scale. To safely detect the network size N given a known number n of measured units from iteratively increasing the number of measurements M (see Fig. 18c), we propose the following algorithm:

1. Start, given the lower bound $n \leqslant N$, with a set of $M = n + 1$ measurement trajectories $\mathbf{y}^{(m)}(t)$, $m \in \{1, \dots, M\}$.

2. Choose $k = \lceil \frac{M}{n} \rceil$ different time instants $t_\kappa \in \{t_1, \dots, t_k\}$ separated by $\Delta t = t_{\mathrm{tot}}/k$, where t_{tot} is the total duration of each time series considered and t_1 its start time.

3. Construct the detection matrix

$$T_{(k,M)} = \begin{bmatrix} \mathbf{y}^{(1)}(t_1) & \dots & \mathbf{y}^{(M)}(t_1) \\ \vdots & & \vdots \\ \mathbf{y}^{(1)}(t_k) & \dots & \mathbf{y}^{(M)}(t_k) \end{bmatrix} \tag{136}$$

   from the measurements $\mathbf{y}^{(m)}(t)$ and compute its $b = \min\{kn, M\}$ $= M$ singular values $\sigma\left(T_{(k,M)}\right)$.

4. Compute logarithmic gaps Δ_j as in (135).

5. Save the largest gap $\widetilde{N}_n^{(M)} := \max\{\Delta_j\}$, where $j \geqslant n$ and $j \notin \{n, 2n, \dots\} \cup \{n+1, 2n+1, \dots\}$, avoiding gaps at integer multiples of n.

6. To robustly identify size also in case N is such an integer multiple, repeat steps 2–5 for $n-1, \dots, n-4$ measured units (thus ignoring actually measured units) and take as the estimate $\hat{N}^{(M)} :=$ $\mathrm{median}\{\widetilde{N}_n^{(M)}\}$.

7. If $\hat{N}^{(M)}$ does not increase further, stop and define $\hat{N} := \hat{N}^{(M)}$ as an estimate of network size; otherwise, repeat steps 2–6 with one additional measurement, $M \to M+1$;

Here, step 2 ensures that finally, we will have $kn > N$ because $M > N$, see the examples below.

6.4 PERFORMANCE OF NETWORK SIZE DETECTION

To test the predictive power of our theory combined with the simple algorithm provided we inferred the network size for five different classes of network dynamics: (i) noiseless, diffusively coupled one-dimensional linear units collectively converging to stable fixed points, (ii) phase-oscillator networks close to periodic phase-locked states, systems of N three-dimensional coupled oscillatory units that exhibit (iii) regular periodic as well as (iv) irregular chaotic collective dynamics, and (v) noisy, heterogeneous systems with nonlinear dynamics. For settings (i) and (ii), we define the class of diffusively coupled systems of single-variable units via (127) with $F_i(\mathbf{z}) = \omega_i + \sum_{j=1}^{N} A_{ij} f\left(z_j - z_i\right)$, where $f : \mathbb{R} \to \mathbb{R}$ is a smooth function and $\omega_i \in \mathbb{R}$ is a constant driving signal. We provide all model and simulation details in the Supplemental Material (Sec. 6.6).

For the simplest setting of linear noiseless systems, we take $f(x) = cx$ with stable fixed point z^* (Fig. 19a-c). The estimated rank of the detection matrix (132) indicated by a pronounced gap in its singular value spectrum accurately predicts network size (Fig. 19a) and is reliable already if only about 10% of the units are measured (Fig. 19b). Measuring larger fractions n/N of units rapidly further improves distinguishing the largest gap Δ_N from other gaps Δ_j. For nonlinearly coupled systems of phase-oscillators ($f(x) = c\sin(x)$, $\omega_i \in [-0.1, 0.1]$, see Sec. 6.6), performance is similarly high despite locally linear approximations (Fig. 19d-f). We expected this similarity in performance, because phase-locked states map to fixed points in a corotating frame of reference and linearization of the sine function constitutes a well-conditioned approximation for $|x| \ll \pi/2$.

Complex transient dynamics and biological networks. The idea introduced above is readily generalized to systems of higher-dimensional units and more complex forms of collective dynamics, including, in principle, arbitrary periodic or chaotic motion. Now consider that z^* is not a fixed point of the dynamics (127) but *any point in state space.* We locally approximate near z^* the nonlinear flow $\mathbf{\Phi}_t(\cdot)$ [57] defined for all solutions $z(t)$ of the original nonlinear differential equation (127) via $z(t) = \mathbf{\Phi}_t(z(0))$ from some initial conditions $z(0)$, see also Sec. 2.3. The difference vector $\delta z(t) = z^{(1)}(t) - z^{(2)}(t)$ of two close-by

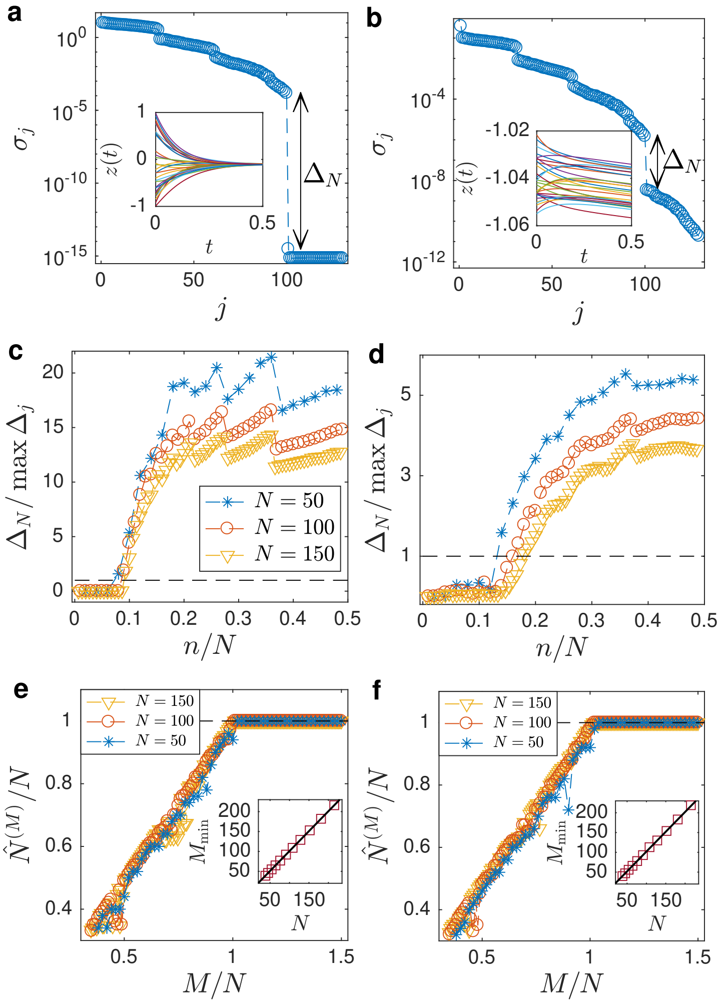

Figure 19: **Singular values of detection matrix yield network size.** *(a),(b)* Singular values σ_j of detection matrix $T_{(k,M)}$ displayed for networks of (a,c,e) linear, diffusively coupled units and (b,d,f) nonlinearly coupled Kuramoto oscillators near a phase-locked state (directed random graphs of $N = 100$ units with in-degree $g = N/10$, $n = 30$ measured, see Supplemental Material, Sec. 6.6, for more details). The largest gap Δ_N reveals network size. *Insets:* Example trajectories. *(c),(d)* Size of Δ_N relative to largest Δ_j for $j < N$ rises above detection threshold at unity (horizontal dashed line). Every data point averaged over 20 independent random networks ($M = 1.5N$). *(e),(f)* For increasing number of experiments M, the inferred number $\hat{N}^{(M)}$ of units proportionally increases until it stays constant at $\hat{N}^{(M)} = N$ once $M > N$. *Inset:* Minimum number $M_{\min}$ of experiments to achieve $\hat{N}^{(M)} = N$ for networks of different sizes N (red squares, $n = N/3$ measured units). All results well fit the prediction $M_{\min} = N + 1$ (solid line). For Kuramoto dynamics, the prediction is $M_{\min} = N + 2$ as one measurement time series is used as a reference.

trajectories indexed 1 and 2 then satisfies (see Supplemental Material, Sec. 6.6, for a step-by-step derivation)

$$\delta \mathbf{z}(t) \doteq D\mathbf{\Phi}_{t-t^*}\Big|_{\mathbf{z}^*} \delta \mathbf{z}(t^*) \tag{137}$$

where $D\mathbf{\Phi}_{t-t^*}\Big|_{\mathbf{z}^*}$ denotes the Jacobian matrix of $\mathbf{\Phi}_{t-t^*}(\cdot)$ evaluated at $\mathbf{z}^*$ and the symbol "$\doteq$" indicates first order approximation in the components of $\delta \mathbf{z}(t^*)$. Employing a projection equivalent to (129) above, we now take the time series of the measured units to be

$$\mathbf{y}(t) = \begin{bmatrix} I_n & 0 \end{bmatrix} \delta \mathbf{z}(t), \tag{138}$$

the matrix generating the dynamics to have elements

$$\theta_{ij}(t) := \left(D\mathbf{\Phi}_{t-t^*}\Big|_{\mathbf{z}^*} \right)_{ij} = \frac{\partial \Phi_{i,t-t^*}}{\partial z_j}\Big|_{\mathbf{z}^*} \tag{139}$$

and re-obtain (130) for the difference variables. We emphasize that the resulting equations are mathematically identical to (130) such that combining time series data as before into a detection matrix yields the network size exploiting the same principles and steps as above. In simulations, we consider $\mathbf{z}^{(2)}(0) = \mathbf{z}^*$ for simplicity and thus consider $t^* = 0$ and positive times $t > 0$. Figure 20 illustrates successful network size identification for high-dimensional periodic motion and for collective chaotic dynamics.

To illustrate applicability to biological circuits, we tested networks displaying Michaelis Menten kinetics, a paradigmatic model of biochemical reaction dynamics (see Figure 21 and Supplemental Material, Sec. 6.6). Intriguingly, exact size detection is feasible even in such systems simultaneously exhibiting nonlinearities, heterogeneities and noise. Most interestingly, detection may be exact despite noise. An increasing number of time series taken into account still enables exact size identification, $\hat{N} = N$. See also Supplemental Fig. 22 for a systematic evaluation of the influence of noise [2].

6.5 DISCUSSION AND CONCLUSIONS

In summary, we proposed a theory for determining the network size from time series data sampled from a potentially small subset of perceptible units. The novel perspective offers a generic tool for detecting the network size from a fundamental theorem of linear algebra applied to linear constraints on a suitably constructed detection matrix. The main conditions for applicability are that (i) $M > N$ trials are experimentally feasible and that (ii) the sampling is such that data points on a given trajectory are sufficiently close in state space for the dynamics obtained from local linearization to well approximate

2 We use a modified Euler scheme [125] for simulating systems with noise.

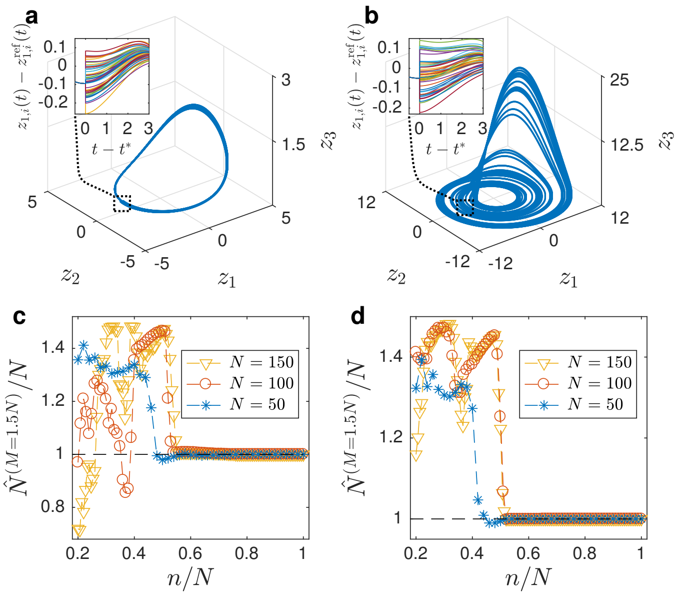

Figure 20: **Network size from complex transient dynamics.** Projection of sample trajectories of one unit i for *(a)* periodic and *(b)* chaotic dynamical regimes. Each time, the system passes a certain region on the attractor (highlighted by a dashed square), a random perturbation is applied to the components $z_{1,i}$ (insets). *(c,d)* Using deviations $\delta z^{(m)}_{1,i}(t) = z^{(m)}_{1,i}(t - t^*_m) - z^{(1)}_{1,i}(t - t^*_1)$ for each perturbation experiment m to construct $T_{(k,M)}$ reveals the correct system size $\hat{N}^{(M)} = N$, if a sufficient fraction n/N of units is measured. All data points averaged over 20 random network realizations of $N = 100$ units with degree ten, exhibiting Rössler oscillatory dynamics, with state $\mathbf{z}_i(t) = (z_{1,i}(t), z_{2,i}(t), z_{3,i}(t))$, and diffusive coupling between z_2 components. In the examples shown, the z_1 components of units i are perturbed and measured. Despite the coupling being in the z_2 components, network size identification is accurate at $\hat{N}/N = 1$.

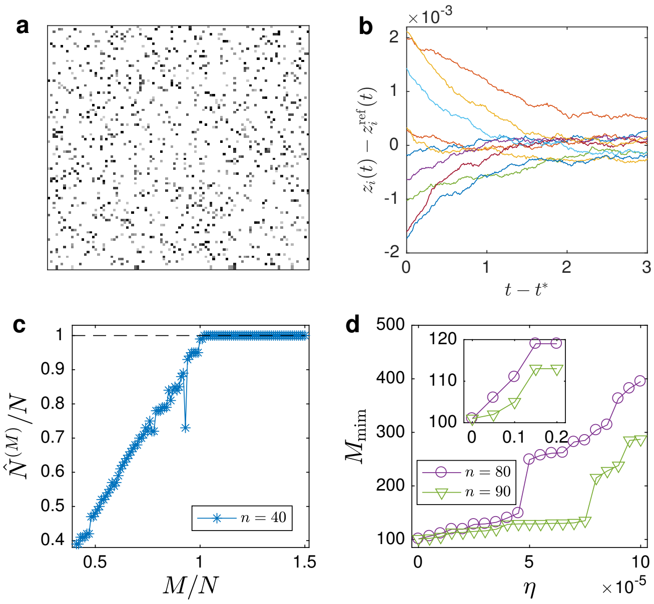

Figure 21: **Exact size detection in biological circuits simultaneously exhibiting nonlinearities, heterogeneities, and noise.** *(a)* Adjacency matrix of a coupled Michaelis Menten kinetic network ($N = 100$, link weights in gray scale) and *(b)* its collective noisy dynamics (units of ten randomly selected units displayed, $\eta = 10^{-4}$). As for coupled periodic and chaotic systems, deviations $\delta z_i^{(m)}(t) = z_i^{(m)}(t - t_m^*) - z_i^{(1)}(t - t_1^*)$ are used for the reconstruction. *(c)* Increasing the number M of measurements taken into account in the detection matrix reveals the network size once $M > N$ in the absence of noise. *(d)* The minimum number M_{min} of experiments required to obtain an *exact* size prediction $\hat{N}^{(M)} = N$ for $M \geqslant M_{\mathrm{min}}$, in dependence of the noise level $\eta > 0$.

the real dynamics. While the time steps $t_2 - t_1, \dots, t_k - t_{k-1}$ need to be the same in each measurement, we emphasize that only very few, down to $k = 2$, are needed in principle. Moreover, even in modular networks where most perceptible units are located in one module, network size detection may work reliably (see also Supplemental Fig. 24).

Compared to the state of the art, the conditions underlying network size identification can be considered mild, for at least two reasons. First, because so far only one or potentially a few individual hidden nodes are identifiable at all [118–120] whereas our approach enables the identification of an extensive number of simultaneously hidden nodes. These may even be the majority of all nodes in the network. Second, because time series analysis methods of finding the attractor dimension (that constitutes a lower bound of and sometimes could equal the dimensionality of state space, and thus the number N of active variables) require $M' \gg N$ data points and in addition are typically limited to moderate or even small N of the order of 10 or lower [126]. For example, to obtain faithful attractor dimensions that constitute lower bounds on N, as many as $M' > 10^4$ data points may be required for systems with $N = 3$ active variables [127], whereas our method requires $M' = kM$ data points with moderate or small $k \geqslant 2$ and M just slightly larger than N.

A related challenge is network observability [128–131], that is to identify a sufficient set of units such that measuring these units' states reveals the collective state of the entire network. In contrast, our work aims at identifying the number of units in a network, not their states. It is thus conceptually different and exhibits much weaker requirements.

Previous approaches to detect hidden nodes are capable of detecting a single hidden node in an otherwise completely perceptible network: Some [132] employ nonlinear Kalman filters to fit the parameters of a given model and use the covariance matrix of the fitting error; others first approximate the dynamics via differential equations and then determine the existence and location of the hidden unit through heuristic methods [118–120]. Our theory instead reliably captures many hidden units, is data driven, relies on sampled time series and thereby requires no model *a priori*. Furthermore, it provides a mechanistic perspective that not only determines the existence but also reveals the exact number of hidden units. It may thus also complement embedding methods for determining attractor dimensions [126] that identify the number of active variables from stationary time series, thereby opening up a way to broaden insights about the collective dynamics of multidimensional complex systems. [131].

6.6 SUPPLEMENTAL MATERIAL

6.6.1 *Simulating network dynamical systems*

To evaluate our identification method, we consider five different classes of network dynamical systems, *(i-v)*. To study the exact linear dynamics near fixed points and linearized dynamics near periodic orbits in systems with one variable per unit, we consider two model classes *(i)* and *(ii)* of type

$$\dot{z}_i = \omega_i + \sum_{j=1}^{N} A_{ij} f\left(z_j - z_i\right), \tag{140}$$

where $f : \mathbb{R} \to \mathbb{R}$ is a smooth function and $\omega_i \in \mathbb{R}$ is a constant driving signal. The units interact via directed random graphs with in-degree g and adjacency matrix $A \in \{0, 1\}^{N\times N}$. Here, we take $g = N/10$. As measured units which are not reachable via paths containing hidden units cannot provide information about those hidden units, we consider strongly connected networks such that each unit is reachable from every other in the network. To study the dynamics of networks with higher-dimensional units, we consider Rössler oscillators interacting via diffusive coupling on undirected random graphs with degree $g = N/10$, exhibiting *(iii)* periodic and *(iv)* chaotic collective dynamics. *(v)* As an example for biological systems, we analyze a network dynamical system with Michaelis-Menten kinetics.

(i) Exactly linear systems without noise, $f(z_j - z_i) = c \times (z_j - z_i)$, $\omega_i \equiv 0$ for all i, and $c = 10/g$. Initial conditions $\boldsymbol{z}_0$ are randomly drawn from the uniform distribution in $[-1, 1]^N$. We compute the trajectories $\boldsymbol{z}(t)$ for $t \in [0, 1]$ with the exact solution using MATLAB's `expm()` function to calculate matrix exponentials. Here, we have linear dynamics such that the time series used for reconstruction via Eq. (129) and Eq. (132) equal those directly measured, i.e. $x_i(t) = z_i(t)$ for unit i and $\dot{\mathbf{x}} = -cL\mathbf{x}$ with the Graph Laplacian matrix $L = gI_N - A$.

(ii) Networks of Kuramoto oscillators, $f(z_j - z_i) = c \times \sin(z_j - z_i)$, and $c = 10/g$. The natural frequencies ω_i were drawn from the uniform distribution in $[-0.1, 0.1]^N$. Long simulations starting from $z_i(-100) = 0$ for all i and $t \in [-100, 0]$, result in the system being in some phase-locked state, where we pick $\boldsymbol{z}^* = \boldsymbol{z}(0)$, a point on the periodic orbit. The common frequency

$$\Omega = (1/N) \sum_i [\omega_i + c \sum_j A_{ij} \sin(z_j^* - z_i^*)] \tag{141}$$

is not generally zero as the sum over j does not generally equate to zero for directed networks and thus asymmetric A_{ij} . The trajectories $x_i(t)$ for the hidden nodes detection are obtained from simulations in $t \in [0, 1]$ with $z_{0,j} = z_j^* + s_j$ and the s_j independently drawn from the uniform distribution on $[-10^{-2}, 10^{-2}]$. Given that Ω is, in general, unknown, we use the deviations $x_i^{(m)}(t) = z_i^{(m)}(t) - z_i^{(1)}(t)$ of experiment m from a reference experiment to obtain the trajectories used to construct the inference relation Eq. (132) via Eq. (129). For numerical integration, we use the MATLAB `ODE45` solver.

(iii & iv) Networks of diffusively coupled Rössler oscillators. Each node i has a state vector $\boldsymbol{z}_i(t) = (z_{1,i}(t), z_{2,i}(t), z_{3,i}(t))$ and the dynamical system reads

$$\dot{z}_{1,i} = -z_{2,i} - z_{3,i} \tag{142}$$

$$\dot{z}_{2,i} = z_{1,i} + \alpha z_{2,i} - \sum_{j=1}^{N} L_{ij} z_{2,j} \tag{143}$$

$$\dot{z}_{3,i} = \beta + (z_{1,i} - \gamma) \cdot z_{3,i}. \tag{144}$$

We test our method in two dynamical regimes: We explore *(iv)* a periodic attractor with $\alpha = 0.2, \beta = 1.7, \gamma = 4$ and *(v)* a chaotic attractor with $\alpha = \beta = 0.2, \gamma = 5.7$. We start the integration at $\boldsymbol{z}_i(0) = (1, 1, 1)$ for all i and let the system move on the respective attractor in a single, long trajectory. For the reference point $\boldsymbol{z}^*$ in phase space we choose *(iv)* $\boldsymbol{z}_i^* = (-3, 0, 0.24)$ and *(v)* $\boldsymbol{z}_i^* = (-6, 0, 0.17)$, see Fig. 20a,b. Whenever the system is sufficiently synchronous ($\max_{i,j} |z_{2,i} - z_{2,j}| < 10^{-5}$) and passes the value $z_2 = 0$ in the region *(iv)* $-3.1 \leqslant z_1 \leqslant -2.9$ or *(v)* $-6.1 \leqslant z_1 \leqslant -5.9$, respectively [3], we apply an instantaneous perturbation of the z_1-components: $z_{1,i}(t_m^*) \to z_{1,i}(t_m^*) + s_i$. Here, s_i is independently drawn from the uniform distribution in $[-0.1, 0.1]$. We use the fourth-order Runge-Kutta scheme with $dt = 5 \cdot 10^{-3}$ for the numerical integration. For a precise determination of $\boldsymbol{z}(t_m^*)$ at which $z_{2,i} \approx 0$ for all i, we choose one intermediate time step from a linear interpolation between the two regular Runge-Kutta steps that cross $z_{2,i} = 0$. For the construction of $T_{(k,M)}$, we calculate $\delta z_i^{(m)}(t) = z_{1,i}^{(m)}(t - t_m^*) - z_{1,i}^{\mathrm{ref}}(t - t_{\mathrm{ref}}^*)$ for $t_m^* \leqslant t \leqslant t_m^* + 3$, where t_m^* denotes the mth perturbation time instant and "ref" names a reference trajectory for which we choose the first observed perturbation.

(v) Noisy Michaelis-Menten kinetics. Michaelis-Menten kinetic models serve as simple standard paradigms for the dynamics of biochemical reaction networks [5] that we use to illustrate successful size detection in systems simultaneously exhibiting nonlinearities, stochasticity, and heterogeneities. For directed random networks $N = 100$ nodes with $g = 10$ incoming connections each, we consider noisy time evolution defined by the coupled equations of motion

$$\dot{z}_i = -z_i + \sum_{j=1}^{N} J_{ij} \frac{z_j}{1 + z_j} + \xi_i(t). \tag{145}$$

3 As the synchronization of the z_3-components takes place very fast, we need no restriction for $\boldsymbol{z}^*$ on the $z_{3,i}$'s.

Here, $J \in \mathbb{R}^{N \times N}$ denotes the weighted adjacency matrix with elements $J_{ij} \neq 0$ if there is a direct influence of molecular species j onto the rate of change of the abundance $z_i(t)$ of molecular species i. Link weights are heterogeneous and drawn from the uniform distribution in $[0.2, 0.5]$ such that their largest values may be up to 250% of their lowest values. ξ_i represents external i.i.d Gaussian noise acting on unit i, with correlation $\left\langle \xi_i(t)\xi_j(t')\right\rangle = \eta^2\delta(t-t')\delta_{ij}$ and average zero, $\langle \xi_i(t)\rangle = 0$. In the absence of noise, the system exhibits a stable fixed point $\boldsymbol{z}^*$; For times $t \in [-100, 0]$, we evolve the system towards $\boldsymbol{z}^*$. We record time series starting from $t = t^* = 0$, after applying random perturbations $z_j = z_j^* + s_j$, with the s_j drawn from the uniform distribution in $[-10^{-2}, 10^{-2}]$. To avoid an extensive number of rows in $T_{(k,M)}$ in the presence of noise ($\eta > 0$), we only use $k = 3$ time steps to set up $T_{(k,M)}$. As demonstrated in the main manuscript, this is already sufficient to reveal network size reliably.

6.6.2 *Noisy linear systems*

To systematically investigate the influence of noise, we extend (140) to

$$\dot{z}_i = \omega_i + \sum_{j=1}^{N} A_{ij} f\left(z_j - z_i\right) + \xi_i(t), \tag{146}$$

where ξ_i represents external i.i.d Gaussian noise acting on unit i, with correlation $\left\langle \xi_i(t)\xi_j(t')\right\rangle = \eta^2\delta(t-t')\delta_{ij}$ and average zero, $\langle \xi_i(t)\rangle = 0$. We choose pure linear dynamics, $f(z_j - z_i) = c \times (z_j - z_i)$, $\omega_i \equiv 0$ for all i and $\eta \neq 0$. With otherwise the same set-up as for *(i)*, we use a modified Euler scheme [125] with time step $dt = 10^{-3}$ to solve the stochastic differential equation. However, to avoid an extensive number of rows kn in $T_{(k,M)}$, we use only $k = 3$ time steps separated with $\Delta t = 0.08$ to set up $T_{(k,M)}$.

Although the quality of performance is generally reduced with increasing noise levels, perfect prediction of network size from noisy time series is still possible if more trajectories are recorded, Fig. 22. While for noise-free dynamics, $M > N$ observable trajectories are sufficient to correctly determine N, the minimum number M_{min} of measurements to perfectly determine N increases with greater noise strength η, Fig. 22a. Fig. 22b illustrates that prediction quality increases with larger fractions n/N of units measured, and that for each noise level (at fixed number of measured time series), prediction ultimately becomes exact, i.e. the predicted equals the actual network size, $\hat{N}/N = 1$.

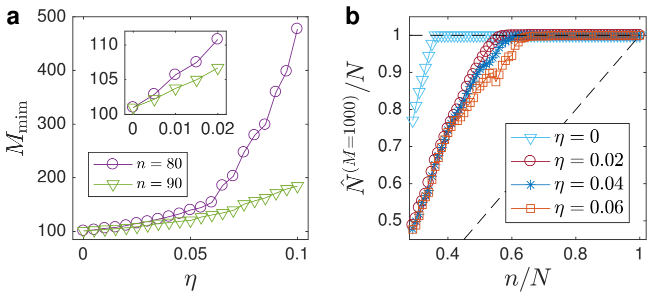

Figure 22: **Exact size prediction in noisy systems.** *(a)* Minimum number $M_{\min}$ of measurements to exactly determine network size for different noise strengths η and $N = 100$. The effects of noise may be compensated by increasing the number of time series. *(b)* Normalized predicted size $\tilde{N}/N$ versus fraction n/N of observed units for different system sizes for different noise levels η at fixed $M = 1000$. Every point represents an average over 20 random network realizations. The dashed line indicates the number of nodes predicted simply as the number of observed units, $\hat{N} = n$, i.e. prior knowledge provided by the observation itself without using any dynamical information.

6.6.3 *Generalization to systems without stable fixed point*

Our method is based on the idea to interpret measured data $\mathbf{y}(t) \in \mathbb{R}^n$ as linear combinations of the full set of N initial conditions $x_j(0)$, $j = 1, \ldots, N$, Eq. (130). In the main text, we have shown how this is achieved in the vicinity of stable fixed points. However, in a general network dynamical system $\dot{\mathbf{z}} = \mathbf{F}(\mathbf{z})$, we may obtain similar expressions– thus making our method applicable to a general class of network dynamical systems.

We relate the time evolution $\mathbf{z}(t) \in \mathbb{R}^N$ to the initial conditions $\mathbf{z}(0)$ through the nonlinear flow $\boldsymbol{\Phi}_t(\cdot)$:

$$\mathbf{z}(t) = \boldsymbol{\Phi}_t(\mathbf{z}(0)). \tag{147}$$

Besides the fact that only the first $1, \ldots, n$ components of $\mathbf{z}(t)$ are measurable, only little is known about $\boldsymbol{\Phi}_t$. In particular, we will generally find no explicit expression.

Let us, instead, consider two trajectories $\mathbf{z}^{(1)}(t)$ and $\mathbf{z}^{(2)}(t)$ which are close to some point $\mathbf{z}^*$ at time t^*

$$\mathbf{z}^{(\nu)}(t^*) = \mathbf{z}^* + \Delta\mathbf{z}^{(\nu)}(t^*) \tag{148}$$

for $\nu \in 1, 2$. We emphasize that z^* needs not to be a fixed point. If we now take into account the difference $\delta z(t) := z^{(1)}(t) - z^{(2)}(t)$ between two such trajectories at times $t > t^*$, we obtain

$$\begin{aligned}
\delta z(t) &= z^{(1)}(t) - z^{(2)}(t) && (149)\\
&= \Phi_{t-t^*}(z^{(1)}(t^*)) - \Phi_{t-t^*}(z^{(2)}(t^*)) && (150)\\
&= \Phi_{t-t^*}(z^* + \Delta z^{(1)}(t^*)) - \Phi_{t-t^*}(z^* + \Delta z^{(2)}(t^*)) && (151)\\
&\doteq \Phi_{t-t^*}(z^*) + D\Phi_{t-t^*}\Big|_{z^*} \Delta z^{(1)}(t^*) \\
&\quad - \Phi_{t-t^*}(z^*) - D\Phi_{t-t^*}\Big|_{z^*} \Delta z^{(2)}(t^*) && (152)\\
&= D\Phi_{t-t^*}\Big|_{z^*} (\Delta z^{(1)}(t^*) - \Delta z^{(2)}(t^*)) && (153)\\
&= D\Phi_{t-t^*}\Big|_{z^*} \delta z(t^*). && (154)
\end{aligned}$$

Here, $D\Phi_{t-t^*}\Big|_{z^*}$ denotes the Jacobian matrix of $\Phi_{t-t^*}(\cdot)$ evaluated at z^* and the symbol "$\doteq$" denotes first order approximation in $\Delta z^{(\nu)}(t^*)$.

6.6.4 *Example with* $k = 2$ *measured time points per trajectory*

If more than half of the units are perceptible, the singular values of the detection matrix $T_{(k,M)}$ reveal the network size N even if only two time instants per trajectory are used ($k = 2$). To derive this limit of low number of time steps, we consider that under ideal conditions, $M \geqslant N + 1$ measured trajectories are sufficient to reveal network size. Thus if the number n of perceptible units is larger than half the network size, $n \geqslant \frac{N+1}{2}$, according to step 2 in the algorithm explained in the main manuscript, $k = \lceil \frac{M}{n} \rceil = 2$. Intuitively, only two time instants may contain sufficient information about the state space dimensionality because repeated measurements of independently randomly initialized trajectories of the same system maximize linear independence among data vectors, therefore sampling high-dimensional volumes of the phase space. We illustrate an example of such minimal data usage in Fig. 23.

6.6.5 *Example of decreased performance due to clustering of measured nodes*

We illustrate a possible limitation of our method in cases where all or most perceptible units are much closer to each other (measured in terms of path length on the underlying graph) than they are to those units that are not perceptible. Fig. 24 illustrates a graph with loosely connected modules. Clustering of perceptible nodes in one of the modules (Figs. 24 a-d) can lead to a reduced size of the gap Δ_N in the singular value spectrum (Figs. 24 e-h) and hence a more difficult detection of the network size N. In the example shown, the most

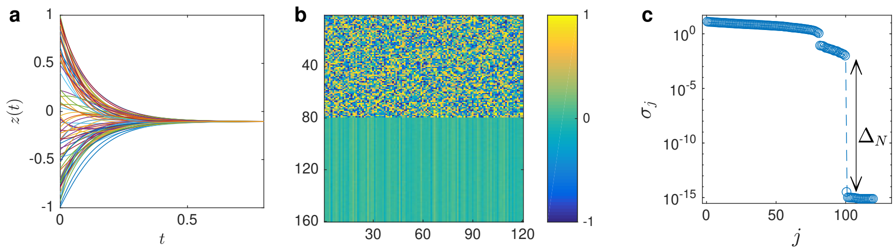

Figure 23: **Inference of number of network size is feasible with only two time instants per measurement (k=2).** *(a)* Trajectories $y(t)$ from which only $y(t_1 = 0)$ and $y(t_2) = 0.5$ are used. Here, we use a deterministic linear system (case *(i)*) with $N = 100$ and $n = 80$. *(b)* Detection matrix $T_{(k,M)}$ after $M = 130$ experiments. The upper half are the $\mathbf{y}^{(m)}(t_1)$ with large amplitudes and the lower half consists of the $\mathbf{y}^{(m)}(t_2)$ with smaller amplitudes. *(c)* Singular values of the detection matrix shown in (b): A clear and large gap correctly reveals $N = 100$.

extreme case of all perceptible units being part of one module and not being part of the second, the largest gap size between singular values does not reveal network size. An estimator resulting from the index j where the singular values reach the level of numerical resolution would here indicate $N^{num} = 28$, still close to the real $N = 30$.

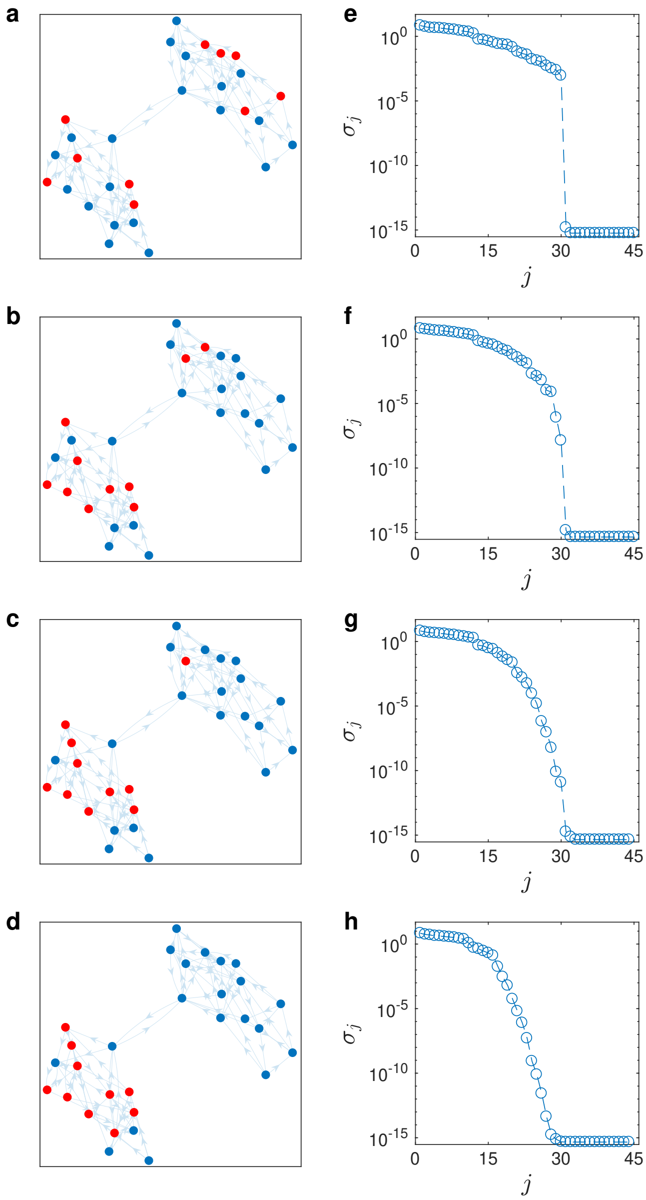

Figure 24: **Clustering of perceptible units can hinder network size detection in specific topologies.** *(a-d)* Directed Graph ($N = 30$) with linear dynamics (case *(i)*) with different choices of $n = 10$ measured units marked in red color. The graph has two modules which are only connected through one bidirectional link. *(e-h)* Singular values of $T_{(k,M)}$ with $M = 45$ measurements. The gap Δ_N after N singular values diminishes the more the perceptible units (red) cluster on one side of the link connecting the two modules. Even if no unit is present in the second module (d), the singular values σ_j reach numerical resolution at $N^{num} = 28$, still close to the real $N = 30$.

7 DISCUSSION & OUTLOOK

In this thesis, we discussed two specific problems in the field of network dynamical systems. First, we presented our analytical, numerical, and experimental results on how fluctuating wind power feed-in affects the short-term fluctuations of the power grid frequency. Second, we provided a novel theoretical approach for the detection and quantification of hidden units in network dynamical systems which is not restricted to networks of phase-coupled oscillators, such as power grids, but applies to a much broader class of systems.

With our experimental setup to measure the grid frequency, we showed that wind power injection directly influences frequency fluctuations in Oldenburg, but not in Göttingen. We further worked out an analytical theory for the propagation of fluctuations in power grids which indicates a strong localization of such fluctuations in the vicinity of the volatile injection. We deduced analytical expressions for the width of frequency increment statistics at nodes distant to the injection. For the specific case of chain-like grids, we discussed how the eigenvalues Λ_n of the generalized Laplacian determine type and steepness of the decay of fluctuations in the grid. Most importantly for future grids with fewer rotational inertia, emerging soft modes, induced by eigenvalues $\Lambda_n < 1$, may lead to wider ranging fluctuations and must therefore be carefully considered.

We generalized earlier applications of linear response theory to the swing equation [30, 34, 36, 104] to arbitrary signals and increment statistics. Therewith we can directly link the statistical analysis of grid frequency fluctuations to properties of turbulent flows without neglecting effects of intermittency and correlations in fluctuations of wind power production.

Our research gives rise to numerous questions for further research. Yet, the interaction of wind turbines, including their ac-dc-ac converters, with atmospheric turbulence is not fully understood. Where exactly do the fluctuations in the power output stem from? How can controllers contribute to a smoothening of the generated power on timescales as short as seconds? Second, we suggest to explore the exact technical mechanisms that lead to the broadening of frequency increment statistics in our measurements. Which grid component contributes to transporting such fluctuations, which other component could be better configured to absorb them? Further, the impact of our technique to estimate the frequency from voltage samplings could be compared to other methods.

The shape of increment distributions plays a key role in the theory of intermittency in turbulence and is – unfortunately – much more difficult to treat than the width. Our numerical results indicate that the shape, quantified in terms of kurtosis, of frequency increment distributions lasts on much wider spatial scales in the grid than their width. However, what makes the analytical treatment so challenging? Let us consider, once again, our generalized Fourier expansion of the phase angle

$$\alpha_i(t) = \int_{-\infty}^{t} \frac{dt'}{\tau} \delta\Pi_j(t') G_{ij}(t'-t), \tag{155}$$

that is Eq. (79) for a single source of perturbation $\delta\Pi_j(t')$. Differentiation of Eq. (155) with respect to t, multiplication with itself and subsequent application of statistical averaging $\langle\cdot\rangle$ allows us to express the variance $\langle\Delta_\tau\omega_i^2\rangle$ of frequency increments as a function of the correlator $\langle\Delta_\tau\delta\Pi_j(t')\Delta_\tau\delta\Pi_j(t'')\rangle$, that is the autocorrelation function of the increment time series. If we now try to do the same for the kurtosis, we find that this involves fourth order correlators

$$\langle\Delta_\tau\delta\Pi_j(t')\Delta_\tau\delta\Pi_j(t'')\Delta_\tau\delta\Pi_j(t''')\Delta_\tau\delta\Pi_j(t'''')\rangle.$$

Such terms are much more difficult to treat if we cannot make simplifying assumptions on the signal $\delta\Pi_j(t')$. The problem of higher order correlations which arises here is directly related to the closure problem of turbulence as discussed in Sec. 3.1. Recent results show the way towards a multi-point statistics of turbulence through Fokker-Planck modeling of cascade processes [133]. Principally, such a multi-point approach is promising to solve the problem of higher-order correlations also in power grids.

The novel approach for detecting hidden units in network dynamical systems gives rise to many new applications. While in previous approaches, if at all the existence of few hidden units could be detected [118–120], we now provide a framework to reveal the exact number of hidden units. We applied the new method to various types of systems including noisy and chaotic dynamics as well as heterogeneous couplings.

A very interesting generalization of our approach would be the application to discrete-time systems: Let us think of a network of interconnected neurons with membrane potential $V_i(t)$. If the potential exceeds a certain threshold, it fires a spike which affects the potentials of connected neurons. A typical dynamical model for such a network is the leaky integrate-and-fire model

$$\tau\dot{V}_i = -V_i + R_i I_i + \tau \sum_{j=1}^{N} \sum_{m\in\mathbb{Z}} A_{ij}\delta(t - t_{j,m} - \tau_{ij}) \tag{156}$$

[38], where τ, τ_{ij}, and R_i are constants and $I_i(t)$ is an external driving signal. $\delta(\cdot)$ denotes the delta function. Further, $t_{j,m}$ denotes the mth spiking instant of neuron j. Recent results show how systems of kind (156) can be linearized *continuously* in terms of inter-spike intervals $\Delta T_{i,m} := t_{i,m+1} - t_{i,m}$:

$$\Delta T_{i,m} - \Delta T_{i,r} = \left[\tilde{A}\mathbf{y}\right]_i , \tag{157}$$

where $\tilde{A}$ comprises the connectivity of neurons and $\mathbf{y}$ the cross-spike intervals, that is the time difference between spikes of different neurons [38, 50]. Even though Eq. (157) is not a identical to the systems we consider (such as Eq. (128)), it still gives an exciting starting point for possible future applications of our method– in this case to infer hidden neurons.

We hope that our contributions to the field of network dynamical systems will help to better understand the complex dynamics of networked system in terms of both, forward and inverse problems.

BIBLIOGRAPHY

[1] S. H. Strogatz, Nature **410**, 268 (2001).

[2] D. Brockmann and D. Helbing, Science **342**, 1337 (2013).

[3] G. Demirel, E. Barter, and T. Gross, Sci. Rep. **7**, 42352 (2017).

[4] A. Kumar, S. Rotter, and A. Aertsen, Nat. Rev. Neurosci. **11**, 615 (2010).

[5] G. Karlebach and R. Shamir, Nat. Rev. Mol. Cell Biol. **9**, 770 (2008).

[6] B. Huang, M. Lu, D. Jia, E. Ben-Jacob, H. Levine, and J. N. Onuchic, PLOS Comput. Biol. **13**, e1005456 (2017).

[7] G. Filatrella, A. H. Nielsen, and N. F. Pedersen, Eur. Phys. J. B **61**, 485 (2008).

[8] A. E. Motter and M. Timme, Ann. Rev. Cond. Mat. Phys. **9**, 463 (2018).

[9] L. M. Pecora and T. L. Carroll, Phys. Rev. Lett. **80**, 2109 (1998).

[10] M. Newman, *Networks: An Introduction* (Oxford University Press, New York, 2010).

[11] M. Timme and J. Casadiego, J. Phys. A **47**, 343001 (2014).

[12] A. Arenas, A. Díaz-Guilera, J. Kurths, Y. Moreno, and C. Zhou, Phys. Rep. **469**, 93 (2008).

[13] F. A. Rodrigues, T. K. D. Peron, P. Ji, and J. Kurths, Phys. Rep. **610**, 1 (2016).

[14] A. A. Prinz, D. Bucher, and E. Marder, Nat. Neurosci. **7**, 1345 (2004).

[15] M. Timme, Phys. Rev. Lett. **98**, 224101 (2007).

[16] M. Rabinovich, R. Huerta, and G. Laurent, Science **321**, 48 (2008).

[17] Y. Kuramoto, in International symposium on mathematical problems in theoretical physics, edited by H. Araki (Springer, 1975), pp. 420–422.

[18] M. Rohden, A. Sorge, M. Timme, and D. Witthaut, Phys. Rev. Lett. **109**, 064101 (2012).

[19] P. J. Menck, J. Heitzig, N. Marwan, and J. Kurths, Nat. Phys. **9**, 89 (2013).

[20] A. E. Motter, S. A. Myers, M. Anghel, and T. Nishikawa, Nat. Phys. **9**, 191 (2013).

[21] P. J. Menck, J. Heitzig, J. Kurths, and H. J. Schellnhuber, Nat. Commun. **5**, 3969 (2014).

[22] D. Witthaut, M. Rohden, X. Zhang, S. Hallerberg, and M. Timme, Phys. Rev. Lett. **116**, 138701 (2016).

[23] P. Milan, M. Wächter, and J. Peinke, "Wind turbine power performance and application to monitoring," in *Handbook of wind power systems*, edited by P. M. Pardalos, S. Rebennack, M. V. F. Pereira, N. A. Iliadis, and V. Pappu (Springer, Berlin, Heidelberg, 2013), pp. 673–708.

[24] C. Hens, U. Harush, S. Haber, R. Cohen, and B. Barzel, Nat. Phys. **15**, 403 (2019).

[25] P. Milan, M. Wächter, and J. Peinke, Phys. Rev. Lett. **110**, 138701 (2013).

[26] M. Anvari, G. Lohmann, M. Wächter, P. Milan, E. Lorenz, D. Heinemann, M. R. R. Tabar, and J. Peinke, New J. Phys. **18**, 063027 (2016).

[27] M. M. Bandi, Phys. Rev. Lett. **118**, 028301 (2017).

[28] U. Frisch, *Turbulence: The Legacy of A. N. Kolmogorov* (Cambridge University Press, Cambridge, 1995).

[29] J. Argyris, G. Faust, M. Haase, and R. Friedrich, *Die Erforschung des Chaos: eine Einführung in die Theorie nichtlinearer Systeme* (Springer, Berlin, Heidelberg, 2010).

[30] S. Kettemann, Phys. Rev. E **94**, 062311 (2016).

[31] B. Schäfer, M. Matthiae, X. Zhang, M. Rohden, M. Timme, and D. Witthaut, Phys. Rev. E **95**, 060203 (2017).

[32] K. Schmietendorf, J. Peinke, and O. Kamps, Eur. Phys. J. B **90**, 222 (2017).

[33] S. Auer, F. Hellmann, M. Krause, and J. Kurths, Chaos **27**, 127003 (2017).

[34] S. Tamrakar, M. Conrath, and S. Kettemann, Sci. Rep. **8**, 6459 (2018).

[35] M. F. Wolff, P. G. Lind, and P. Maass, Chaos **28**, 103120 (2018).

[36] M. Tyloo, T. Coletta, and P. Jacquod, Phys. Rev. Lett. **120**, 084101 (2018).

[37] L. Pagnier and P. Jacquod, PLOS ONE **14**, e0213550 (2019).

[38] J. Casadiego, "Network Dynamics as an Inverse Problem," dissertation (Georg-August-Universität Göttingen, 2016).

[39] M. K. S. Yeung, J. Tegnér, and J. J. Collins, Proc. Natl. Acad. Sci. U. S. A. **99**, 6163 (2002).

[40] T. S. Gardner, D. di Bernardo, D. Lorenz, and J. J. Collins, Science **301**, 102 (2003).

[41] D. Yu, M. Righero, and L. Kocarev, Phys. Rev. Lett. **97**, 188701 (2006).

[42] D. Napoletani and T. D. Sauer, Phys. Rev. E **77**, 026103 (2008).

[43] D. Yu and U. Parlitz, PLOS ONE **6**, e24333 (2011).

[44] S. G. Shandilya and M. Timme, New J. Phys. **13**, 013004 (2011).

[45] B. Barzel and A.-L. Barabási, Nat. Biotechnol. **31**, 720 (2013).

[46] X. Han, Z. Shen, W.-X. Wang, and Z. Di, Phys. Rev. Lett. **114**, 028701 (2015).

[47] N. M. Mangan, S. L. Brunton, J. L. Proctor, and J. N. Kutz, IEEE Trans. Mol. Biol. Multi-Scale Commun. **2**, 52 (2016).

[48] J. Casadiego, M. Nitzan, S. Hallerberg, and M. Timme, Nat. Commun. **8**, 2192 (2017).

[49] M. Nitzan, J. Casadiego, and M. Timme, Sci. Adv. **3**, e1600396 (2017).

[50] J. Casadiego, D. Maoutsa, and M. Timme, Phys. Rev. Lett. **121**, 054101 (2018).

[51] M. Newman, SIAM Rev. **45**, 167 (2003).

[52] L. Euler, Comm. acad. sci. Petropol. **8**, 128 (1741).

[53] E. Estrada and P. A. Knight, *A first course in network theory* (Oxford University Press, New York, 2015).

[54] G. Kirchhoff, Ann. Phys. **140**, 497 (1845).

[55] E. Estrada, *The structure of complex networks: theory and applications* (Oxford University Press, New York, 2012).

[56] R. J. Brown, *A modern introduction to dynamical systems* (Oxford University Press, New York, 2018).

[57] J. K. Hale and H. Koçak, *Dynamics and bifurcations* (Springer, New York, 2012).

[58] C. Gardiner, *Stochastic methods*, Vol. 4 (Springer, Berlin, 2009).

[59] S. Strogatz, *Nonlinear dynamics and chaos: with applications to physics, biology, chemistry, and engineering* (Westview Press, Boulder, 2015).

[60] F. Dörfler, M. Chertkov, and F. Bullo, Proc. Natl. Acad. Sci. U.S.A. **110**, 2005 (2013).

[61] L. Huang, Q. Chen, Y.-C. Lai, and L. M. Pecora, Phys. Rev. E **80**, 036204 (2009).

[62] F. Dörfler and F. Bullo, Automatica **50**, 1539 (2014).

[63] L. F. Richardson, *Weather prediction by numerical process* (Cambridge University Press, Cambridge, 1922).

[64] A. N. Kolmogorov, Dokl. Akad. Nauk SSSR **30**, 301 (1941).

[65] A. M. Obukhov, Dokl. Akad. Nauk SSSR **32**, 22 (1941).

[66] A. N. Kolmogorov, Dokl. Akad. Nauk SSSR **32**, 16 (1941).

[67] W. Heisenberg, Z. Phys. **124**, 628 (1948).

[68] C. F. v. Weizäcker, Z. Phys. **124**, 614 (1948).

[69] C. Renner, J. Peinke, and R. Friedrich, J. Fluid Mech. **433**, 383 (2001).

[70] A. N. Kolmogorov, J. Fluid Mech. **13**, 82 (1962).

[71] Z.-S. She and E. Leveque, Phys. Rev. Lett. **72**, 336 (1994).

[72] F. Milano, *Power system modelling and scripting* (Springer, London, 2010).

[73] B. Schäfer, "Self-Organized Dynamics of Power Grids: Smart Grids, Fluctuations and Cascades," dissertation (Georg-August-Universität Göttingen, 2017).

[74] K. Schmietendorf, J. Peinke, R. Friedrich, and O. Kamps, Eur. Phys. J. S. T. **223**, 2577 (2014).

[75] P. Kundur, N. J. Balu, and M. G. Lauby, *Power system stability and control*, Vol. 7 (McGraw-Hill, New York, 1994).

[76] J. Machowski, J. Bialek, J. R. Bumby, and J. Bumby, *Power system dynamics and stability* (John Wiley & Sons, New York, 1997).

[77] T. Nishikawa and A. E. Motter, New J. Phys. **17**, 015012 (2015).

[78] WindEurope, *Wind in power - 2016 european statistics*, (2017) `https://windeurope.org/wp-content/uploads/files/about-wind/statistics/WindEurope-Annual-Statistics-2016.pdf`.

[79] WindEurope, *Daily wind power numbers*, `https://windeurope.org/about-wind/daily-wind/`, (2018)

[80] ENTSO-E, *ENTSO-E Operation Handbook Policy 1*, `https://www.entsoe.eu/fileadmin/user_upload/_library/publications/entsoe/Operation_Handbook/Policy_1_final.pdf/`.

[81] M. Albadi and E. El-Saadany, Electric Power Systems Research **80**, 627 (2010).

[82] F. Boettcher, C. Renner, H. Waldl, and J. Peinke, Bound.-Layer Meteorol. **108**, 163 (2003).

[83] R. Baile and J.-F. Muzy, Phys. Rev. Lett. **105**, 254501 (2010).

[84] R. Calif, F. G. Schmitt, and Y. Huang, Physica A **392**, 4106 (2013).

[85] X. Liang, IEEE Trans. Industry Appl. **53**, 855 (2017).

[86] B. Schäfer, C. Beck, K. Aihara, D. Witthaut, and M. Timme, Nat. Energy **3**, 119 (2018).

[87] J.-F. Muzy, R. Baïle, and P. Poggi, Phys. Rev. E **81**, 056308 (2010).

[88] O. Kamps, in Wind energy - impact of turbulence, edited by M. Hölling, J. Peinke, and S. Ivanell (2014), pp. 67–72.

[89] Data available online at http://www.uni-oldenburg.de/fileadmin/user_upload/physik/ag/twist/Forschung/Daten/AnvariEtAl2016_ExampleData_WindPowerAndIrradianceData.zip.

[90] M. Lauby, J. Bian, S. Ekisheva, and M. Varghese, in North American Power Symposium (NAPS) (IEEE, 2014), pp. 1–5.

[91] B. Boashash, Proc. IEEE **80**, 520 (1992).

[92] ENTSO-E, *Transp. Platform*, https://transparency.entsoe.eu/.

[93] B. Podobnik, P. C. Ivanov, Y. Lee, A. Chessa, and H. E. Stanley, Europhys. Lett. **50**, 711 (2000).

[94] A Morales, M Wächter, and J Peinke, Wind Energy **15**, 391 (2012).

[95] B. Castaing, Y. Gagne, and E. Hopfinger, Physica D **46**, 177 (1990).

[96] F. Chilla, J. Peinke, and B. Castaing, J. Phys. II France **6**, 455 (1996).

[97] X.-P. Zhang, C. Rehtanz, and B. Pal, *Flexible AC transmission systems: modelling and control* (Springer, Berlin, Heidelberg, 2012).

[98] A. Ulbig, T. S. Borsche, and G. Andersson, IFAC Proc. Vol. **47**, 7290 (2014).

[99] B. Podobnik, P. C. Ivanov, Y. Lee, and H. E. Stanley, Europhys. Lett. **52**, 491 (2000).

[100] P. C. Ivanov, M. G. Rosenblum, C.-K. Peng, J. Mietus, S. Havlin, H. E. Stanley, and A. L. Goldberger, Nature **383**, 323 (1996).

[101] WindEurope, *Wind in power 2017 - Annual combined onshore and offshore wind energy statistics*, (2018) https://windeurope.org/wp-content/uploads/files/about-wind/statistics/WindEurope-Annual-Statistics-2017.pdf.

[102] H. Haehne, J. Schottler, M. Waechter, J. Peinke, and O. Kamps, Europhys. Lett. **121**, 30001 (2018).

[103] R. Friedrich, J. Peinke, M. Sahimi, and M. R. R. Tabar, Phys. Rep. **506**, 87 (2011).

[104] X. Zhang, S. Hallerberg, M. Matthiae, D. Witthaut, and M. Timme, arXiv preprint (2018).

[105] *Windenergie: Leistung installierter Anlagen in Niedersachsen und Bremen*, Fraunhofer Institut für Umwelt-, Sicherheits- und Energietechnik, (2015) https://www.maps4use.de/wp-content/uploads/2015/10/150903_EEG_Windenergie_Leistung_HB_NI_Gemeindeebene_absolut_A3.jpg.

[106] A. Plietzsch, S. Auer, J. Kurths, and F. Hellmann, arXiv preprint (2019).

[107] C. Matke, W. Medjroubi, and D. Kleinhans, *SciGRID-An Open Source Reference Model for the European Transmission Network (v 0.2)*, 2016.

[108] J. Wolter, B. Lünsmann, X. Zhang, M. Schröder, and M. Timme, Chaos **28**, 063122 (2018).

[109] H. Ronellenfitsch, J. Dunkel, and M. Wilczek, Phys. Rev. Lett. **121**, 208301 (2018).

[110] M. Wilczek and R. Friedrich, Phys. Rev. E **80**, 016316 (2009).

[111] T. Coletta and P. Jacquod, Phys. Rev. E **93**, 032222 (2016).

[112] L. A. Torres-Sánchez, G. T. Freitas de Abreu, and S. Kettemann, arXiv preprint (2017).

[113] Y. Sun, C. Liu, C. X. Zhang, and Z. K. Zhang, Phys. Lett. A **378**, 635 (2014).

[114] D. X. Horváth and J. Kertész, New J. Phys. **16**, 073037 (2014).

[115] J. Casadiego and M. Timme, in Mathematical technology of networks, edited by D. Mugnolo (2015), pp. 39–48.

[116] D. Soudry, S. Keshri, P. Stinson, M. H. Oh, G. Iyengar, and L. Paninski, PLoS Comput. Biol. **11**, e1004464 (2015).

[117] B. J. Lünsmann, C. Kirst, and M. Timme, PLOS ONE **12**, e0186624 (2017).

[118] R. Q. Su, W. X. Wang, and Y. C. Lai, Phys. Rev. E **85**, 065201 (2012).

[119] Z. Shen, W. X. Wang, Y. Fan, Z. Di, and Y. C. Lai, Nat. Commun. **5**, 4323 (2014).

[120] R.-Q. Su, W.-X. Wang, X. Wang, and Y.-C. Lai, R. Soc. Open Sci. **3**, 150577 (2016).

[121] J. Gonçalves, R. Howes, and S. Warnick, in Decision and Control, 2007 46th IEEE Conference on (IEEE, 2007), pp. 1516–1522.

[122] J. Gonçalves and S. Warnick, IEEE Transac. Autom. Contr. **53**, 1670 (2008).

[123] Y. Yuan, G.-B. Stan, S. Warnick, and J. Goncalves, Automatica **47**, 1230 (2011).

[124] J. Stoer and R. Bulirsch, *Introduction to numerical analysis*, Vol. 12 (Springer, Berlin, Heidelberg, 2013).

[125] A. Roberts, arXiv preprint (2012).

[126] H. Kantz and T. Schreiber, *Nonlinear time series analysis*, 2nd ed. (Cambridge University Press, Cambridge, 2004).

[127] L. M. Pecora, L. Moniz, J. Nichols, and T. L. Carroll, Chaos **17**, 013110 (2007).

[128] Y.-Y. Liu, J.-J. Slotine, and A.-L. Barabási, Proc. Natl. Acad. Sci. U.S.A. **110**, 2460 (2013).

[129] Y. Tang, F. Qian, H. Gao, and J. Kurths, Ann. Rev. Contr. **38**, 184 (2014).

[130] A. J. Whalen, S. N. Brennan, T. D. Sauer, and S. J. Schiff, Phys. Rev. X **5**, 011005 (2015).

[131] U. Parlitz, in *Chaos detection and predictability* (Springer, 2016), pp. 1–34.

[132] F. Hamilton, B. Setzer, S. Chavez, H. Tran, and A. L. Lloyd, Chaos **27**, 073106 (2017).

[133] J. Peinke, M. R. Tabar, and M. Wächter, Annu. Rev. Condens. Matter Phys. **10**, 107 (2019).

ACKNOWLEDGEMENTS

Diese Arbeit wäre ohne die anhaltende Unterstützung vieler Kolleg*innen, Freund*innen und meiner Familie nicht möglich gewesen.

Joachim Peinke hat mir hier in Oldenburg ermöglicht, mit viel Gestaltungsfreiheit meine Forschungen durchzuführen. Er stand mir stets mit professionellem Rat zur Verfügung und hat durch seinen motivierenden Optimismus diese Arbeit entschieden vorangebracht. Stefan Kettemann hat mich mit seinem Wissen über Linear Response Theory grundlegend weitergebracht; ohne ihn wäre der Artikel in *Phys. Rev. E* so nicht zustande gekommen. Marc Timme hat durch sein umfangreiches Wissen über Netzwerke und dynamische Systeme meine Arbeit über Hidden Units zum Erfolg geführt. Oliver Kamps hat mir in meinem ersten Artikel geholfen, die Ergebnisse klar und verständlich zu präsentieren. Vielen Dank euch allen.

In unserer Arbeitsgruppe „Turbulenz, Windenergie und Stochastik“ am Institut für Physik der Universität Oldenburg habe ich viele spannende und fruchtbare Diskussionen zu verschiedenen Themen geführt, die mich in meiner wissenschaftlichen Arbeit oft weiter gebracht haben. Besonders hervorheben möchte ich Christian Behnken, David Bastine und Katrin Schmietendorf. Mit euch habe ich eine sehr spannende, interessante und sympathische Zeit in Oldenburg verbracht. Matthias Wächter stand mir ebenfalls von Anfang an mit Rat und Tat zur Seite und hat mir bei vielen Problemen geholfen.

Jose Casadiego hat mich mit vielen Ratschlägen und Diskussionen unterstützt, wodurch ich enrom viel gelernt habe. Es tat sehr gut und war unwahrscheinlich wichtig, mit Jose immer einen geduldigen Zuhörer und kompetenten Wissenschaftler an meiner Seite zu haben.

Ronja, ohne dich wäre das sowieso alles nicht möglich gewesen.

***

Die Dokumentvorlage dieser Arbeit stammt von André Miede[1], bei dem ich mich dafür herzlich bedanken möchte.

1 www.miede.de

DECLARATION / ERKLÄRUNG

Hiermit erkläre ich, dass

- ich die vorliegende Arbeit selbst verfasst und nur die angegebenen Hilfsmittel verwendet habe,
- die vorliegende Arbeit weder in Teilen noch in ihrer Gesamtheit einer anderen wissenschaftlichen Hochschule zur Begutachtung in einem Promotionsverfahren vorliegt oder vorgelegen hat und dass
- die vorliegende Arbeit bereits in Teilen veröffentlicht wurde.

Oldenburg, den 15. Juli 2019

Hauke Hähne